



저작자표시-비영리-변경금지 2.0 대한민국

이용자는 아래의 조건을 따르는 경우에 한하여 자유롭게

- 이 저작물을 복제, 배포, 전송, 전시, 공연 및 방송할 수 있습니다.

다음과 같은 조건을 따라야 합니다:



저작자표시. 귀하는 원저작자를 표시하여야 합니다.



비영리. 귀하는 이 저작물을 영리 목적으로 이용할 수 없습니다.



변경금지. 귀하는 이 저작물을 개작, 변형 또는 가공할 수 없습니다.

- 귀하는, 이 저작물의 재이용이나 배포의 경우, 이 저작물에 적용된 이용허락조건을 명확하게 나타내어야 합니다.
- 저작권자로부터 별도의 허가를 받으면 이러한 조건들은 적용되지 않습니다.

저작권법에 따른 이용자의 권리는 위의 내용에 의하여 영향을 받지 않습니다.

이것은 [이용허락규약\(Legal Code\)](#)을 이해하기 쉽게 요약한 것입니다.

[Disclaimer](#)

Ph.D. DISSERTATION

Investigation on the fabrication of
biomimetic Micro-Lens Array and its
application

생체모방형 마이크로렌즈 어레이의 제작과 활용에 관한
연구

BY

JUNGHO YI

DEPARTMENT OF ELECTRICAL AND
COMPUTER ENGINEERING
COLLEGE OF ENGINEERING
SEOUL NATIONAL UNIVERSITY

Ph.D. DISSERTATION

Investigation on the fabrication of
biomimetic Micro-Lens Array and its
application

생체모방형 마이크로렌즈 어레이의 제작과 활용에 관한
연구

BY

JUNGHO YI

DEPARTMENT OF ELECTRICAL AND
COMPUTER ENGINEERING
COLLEGE OF ENGINEERING
SEOUL NATIONAL UNIVERSITY

Investigation on the fabrication of biomimetic Micro-Lens Array and its application

생체모방형 마이크로렌즈 어레이의 제작과 활용에 관한
연구

지도교수 서 종 모

이 논문을 공학박사 학위논문으로 제출함

2023년 8월

서울대학교 대학원

전기 정보 공학부

이 정 호

이정호의 공학박사 학위 논문을 인준함

2023년 8월

위 원 장:	전 누 리
부위원장:	서 종 모
위 원:	박 재 형
위 원:	이 재 상
위 원:	Ivan Kristof

Abstract

With the advancement of technology, robots are becoming increasingly miniaturized. Depending on their purpose, robots are equipped with various sensors, and they typically have visual sensors such as cameras as a basic feature since they are primarily used for human assistance. However, the spatial information obtained from a single camera is limited. Large robots can be equipped with multiple sensors such as LiDAR sensors and Time-of-Flight (ToF) sensors to acquire accurate and diverse information. However, small robots clearly have spatial and energy limitations. In this paper, attempts are made to solve this problem by utilizing bio-inspired micro-lens arrays. By using a micro-lens array, it is possible to view an object from more than two perspectives with a single camera sensor, similar to the binocular vision of human eyes. This enables accurate distance measurement and extraction of various information such as velocity calculation, making it much more useful. Therefore, a few micro-lens arrays were fabricated, verified the information that can be obtained through the micro-lens arrays, and investigated how to arrange the lenses through design analysis for optimal performance.

keywords: Biomimetics, Micro-Lens Array, MEMS, Computer Vision

student number: 2018-25309

Contents

Abstract	i
Contents	ii
List of Tables	v
List of Figures	vi
1 Introduction	1
1.1 Biomimetics	1
1.1.1 Biomimetic Research	1
1.1.2 Vision system	4
1.1.3 Small robot applications	8
1.2 Micro-Lens Array	11
1.2.1 Micro-lens array research	11
1.2.2 Materials and methods for Micro-lens array fabrication	16
1.2.3 Basic Optics	19
1.3 Conclusion and Goal	22
2 Fabrication of artificial compound eyes	24
2.1 PDMS-PVC Micro-lens Array	24
2.1.1 Introduction	24
2.1.2 Materials and Method	25

2.1.3	Result	28
2.1.4	Discussion and Conclusion	31
2.2	COC-CB Micro-lens Array	32
2.2.1	Introduction	32
2.2.2	Materials and Method	34
2.2.3	Results and Discussion	40
2.2.4	Conclusion	46
2.3	PDMS-PTFE Micro-lens Array	48
2.3.1	Introduction	48
2.3.2	Materials and Method	48
2.3.3	Results and Discussion	52
2.3.4	Conclusion	63
3	Micro-Lens Array design in depth	64
3.1	Effect of the aperture	64
3.1.1	Depth-of-Field	64
3.1.2	Field-of-View	69
3.2	Micro-Lens Array Arrangements	70
3.2.1	Arrangements on a flat surface	70
3.2.2	Arrangements on a curved surface	73
3.3	Conclusion	95
4	Application	96
4.1	Use of multiple aspect	96
4.1.1	Small robot application	96
4.1.2	Micro-lens array for Artificial Retina	99
4.1.3	Other possible applications	104
5	Summary	106

List of Tables

2.1	Fabrication method and performance comparisons of various micro-lens arrays.	62
3.1	f-number of the fabricated micro-lens arrays	67
3.2	Numerical comparison of the the number orbits for the arrangements.	73
3.3	Zenith angles in radian where the micro-lenses can be located at its maximum for given parameters.	83

List of Figures

1.1	Biomimetic researches ^[1,3,6,7]	2
1.2	Comparison of human eye and a camera	3
1.3	Binocular Field-of-View of human eye. The overlapping region provides depth information.	5
1.4	Human retinal circuitry ^[14]	6
1.5	Two major types of the compound eye	8
1.6	Lobula Plate of insects ^[20]	9
1.7	Artificial compound eye system that imitated bee's eye for wide field-of-view ^[27]	12
1.8	Artificial compound eye system with pigment cell ^[30]	12
1.9	Foveated vision eagle eye micro-lenses ^[34]	13
1.10	Structure of the three-layer 3D compound eye ^[26]	14
1.11	Micro-lens Array not providing enough overlapping field-of-view ^[26]	15
1.12	Chemical etching method to produce lens shape ^[35]	17
1.13	Thermal-reflow method to produce lens shape ^[36]	17
1.14	Ray refracting at a flat surface	20
1.15	Ray refracting at a concave spherical surface	20
2.1	Picture of the PDMS-PVC MLA	24
2.2	Fabrication Process of the PDMS-PVC MLA.	25

2.3	The fabricated micro-lens array (a) Top-view of the micro-lens array. (b) An individual micro-lens captured using SEM.	27
2.4	The schematic of the imaging system setup using 3D printed jig. . . .	28
2.5	Raw image taken using fabricated the micro-lens array. (a) Image of USAF 1951 for pattern group '-1'. (b) Leftmost 3x3 sub-image of (a) (c) Middle 3x3 sub-image of (a) (d) Resulting image of USAF 1951 for pattern group '0' (e) Leftmost 3x3 sub-image of (d) (f) Middle 3x3 sub-image of (d)	29
2.6	Schematics for distance measurement.	29
2.7	Field-of-View measuring setup and resulting images (a) 3D printed goniometer (b) Raw image taken using the micro-lens array (c) Middle 3x3 sub-image of (b)	30
2.8	The schematics for the hemispherical PVC film micro-lens array. (a) Before the process. The Micro-lens Array is still in flat (b) Formation of the the hemispherical curvature using negative pressure (c) Result- ing hemispherical PVC film micro-lens array	32
2.9	Picture of the COC-CB MLA.	32
2.10	Thermal-reflow of a single micro-lens. (a) Before thermal-reflow (b) After thermal-reflow showing smoother surface	34
2.11	Angle of view and the pitch based on offset of the lens.	36
2.12	Schematic of the COC-CB MLA.	37
2.13	Fabrication Process of the COC-CB MLA.	38
2.14	Experimental setup for the Point Spread Function of the monochro- matic light.	39
2.15	Comparisons of the resulting images with and without the light-screen.	42
2.16	CMOS Image Sensor Results of the monochromatic source.	43
2.17	Fabrication of the curved COC-CB micro-lens array	45

2.18	PDMS contact angle changes over natural curing time on (a) glass and (b) PTFE.	50
2.19	Fabrication steps of the PDMS-PTFE micro-lens array. (a) A glass slide as a substrate. (b) Spin-coat a layer of regular PDMS for adhesion. (c) Applying PFA film on top of the PDMS adhesive layer (d) Spin-coat a layer of the viscosity-modified PDMS. (e) Applying the laser-patterned PTFE film. (f) Protrusion of the modified PDMS through the patterned holes. (g) After curing on a hot plate, remove the substrate and cut out the sample. (h) Resulting PDMS-PTFE micro-lens array.	51
2.20	Fabricated PDMS-PTFE micro-lens array	53
2.21	PDMS-PTFE micro-lens arrays depending on the condition of the PDMS. (Left column) When PDMS was used right after making. (Right column) The micro-lens arrays are formed when PDMS cured at room temperature for 5 hours was used.	53
2.22	Aperture adjustment of the Micro-lens Array. (a) Lens size adjusted by the size of the inner hole with fixed PDMS thickness. (b) Lens size adjusted by the thickness of the PDMS with fixed inner hole diameter.	54
2.23	Images taken using the fabricated micro-lens array and the image sensor. (a) Original image of USAF 1951 resolution test chart. (b) Disparity calculation schematics. (c) 3D printed goniometer and camera setup. (d) Resulting image taken by the micro-lens array showing the printed test target. (e) Appearance of a pawn behind the rook (right red arrow) and disappearance of the pawn (left red arrow). (f) Field-of-View test images of the micro-lens array. Red mark indicates the center of the goniometer.	55
3.1	Changes of Depth-of-Field and brightness due to aperture size	65
3.2	Change of focal length due to aperture	66

3.3	Change of focal length due to aperture	66
3.4	Total power changes by aperture ratio and location	67
3.5	Modulation Transfer Functions of the fabricated Micro-lens arrays. . .	68
3.6	Field-of-View of a flat Micro-lens Array	69
3.7	(a) Single plano-convex micro-lens to be arranged (b) Rectangular (left) and hexagonal (right) arrangements. p_x and p_y representing the pitch (center-to-center). ^[61]	71
3.8	Gray value comparison between the rectangular arrangement and the hexagonal arrangement with a USAF-1951 test target located at one meter away. (a) Rectangular arrangement with red line segment indi- cating the region of analysis. (b) Gray value analysis result of the red line in Fig. 3.8(a). (c) Hexagonal arrangement with red line segment indicating the region of analysis. (d) Gray value analysis result of the red line in Fig. 3.8(c).	72
3.9	Comparison of the rectangular and the hexagonal arrangement on a curved surface. The colored area in the upper row indicates the level of layers from the reference micro-lens (blue area). The red vertical line and the white orbital circle indicate the reference micro-lens, and groups of outer micro-lenses that share the same polar angle from the red line, respectively.	74
3.10	Schematic of Micro-lens Array on a curved surface: focal length . . .	75
3.11	Schematic of a Micro-lens on a curved surface that has elliptical airy disk.	76
3.12	Zemax simulation result for a micro-lens array on a curved surface whose lenses have the same radius regardless of the zenith angle. . . .	78
3.13	Zemax simulation result for a micro-lens array on a curved surface whose lenses have different radii depending on the zenith angle. . . .	79

3.14	Zemax simulation result for a micro-lens array on a curved surface whose lenses have elliptical shape depending on the zenith angle, while maintaining the same initial radius regardless of the zenith angle. . . .	80
3.15	Zemax simulation result for a micro-lens array on a curved surface whose lenses have elliptical shapes depending on the zenith angle while varying the radii depending on the zenith angle.	80
3.16	Schematic of Micro-lens Array on a curved surface: for maximum number of lenses.	81
3.17	Resulting maximum number of lenses simulated on Zemax.	83
3.18	Reason for the flat type Micro-lens array providing wider field-of-view compared to the single lens.	84
3.19	Schematic of the Field-of-View of the micro-lens array on a curved surface.	86
3.20	Schematic of the minimum number of layers required to achieve 180 ° Field-of-View for a micro-lens array on a curved surface.	86
3.21	Change of the maximum field-of-view by curvature R while d_{sensor} , f_0 , and α are constant.	87
3.22	Deformation of micro-lens on a curved surface with $R=1$	88
3.23	Deformation comparison design schemes. (a) Deformation of micro-lens array made of PDMS. (b) Deformation of micro-lens array with PTFE light-screen layer	89
3.24	Deformation comparisons. (a) Rate of changes in height for PDMS. (b) Rate of changes in height for PDMS-PTFE MLA. (c) Rate of changes in width for PDMS. (d) Rate of changes in width for PDMS-PTFE MLA. (e) Rate of changes in pitch length for PDMS. (f) Rate of changes in pitch length for PDMS-PTFE MLA. (g) Rate of changes in pitch length for PDMS depends on the layer order. (h) Rate of changes in pitch length for PDMS-PTFE MLA depending on the order of layer.	90

3.25	Focal length and zenith angle changes after deformation.	93
3.26	f-number changes after deformation. The green and yellow lines indicate the f-numbers of PDMS version and PTFE version, respectively. .	94
4.1	Deep Ego-motion Classification	97
4.2	Octagonal compound eye camera	98
4.3	Result of the combination of the software and hardware	98
4.4	Artificial Retina system overview	99
4.5	Artificial Retina system when the patient gazes sideways	100
4.6	Comparison of the binocular and monocular system in terms of the depth information	100
4.7	Artificial Retina system solution. (A) Example image when seen by the mounted camera, (B) Suggested image when considering the gaze. .	101
4.8	Expected result when the micro-lens array is applied to the artificial retina system	103
4.9	Overview of the 3D trajectory system using Micro-Lens Array ^[28] . .	104
4.10	Disparity map created by a micro-lens array ^[76]	105

Chapter 1

Introduction

1.1 Biomimetics

Humanity has been learning and utilizing many things from nature, thereby enhancing our abilities. We learned to ride and control horses to increase our speed of travel, observed birds in flight to discover the secret of soaring through the sky, acquired the knowledge of swimming and diving from observing fish and whales, by observing slowly descending feathers and dandelion seeds, parachutes were invented, and applied designs of kingfisher that reduce aerodynamic resistance in trains. The examples of applying what we have learned from nature are endless. This process of learning from nature and applying it in an engineering context is called biomimetics.

1.1.1 Biomimetic Research

More specifically, Biomimetics, or Biomimicry is a field of research that studies and imitates the natural world to solve problems and create innovative technologies. It involves observing how living organisms have adapted to their environment and using those insights to develop new materials, structures, and systems. One of the most famous examples of Biomimetics would be the simple and easy fastener system Velcro that was motivated by the hook of the cockle-burs, and other derivative research

[1, 2]. Other biomimetic researches include adhesion researches that mimic feet of frogs, micro-sucker of octopus, and superior wet adhesion ability of mussels [3, 4, 5]. Moreover, to reduce underwater fluid drag, surface structure of the shark-skin had been investigated, and structure of various types of wings had also been studied, to improve performance and efficiency of aerial robots [6, 7].

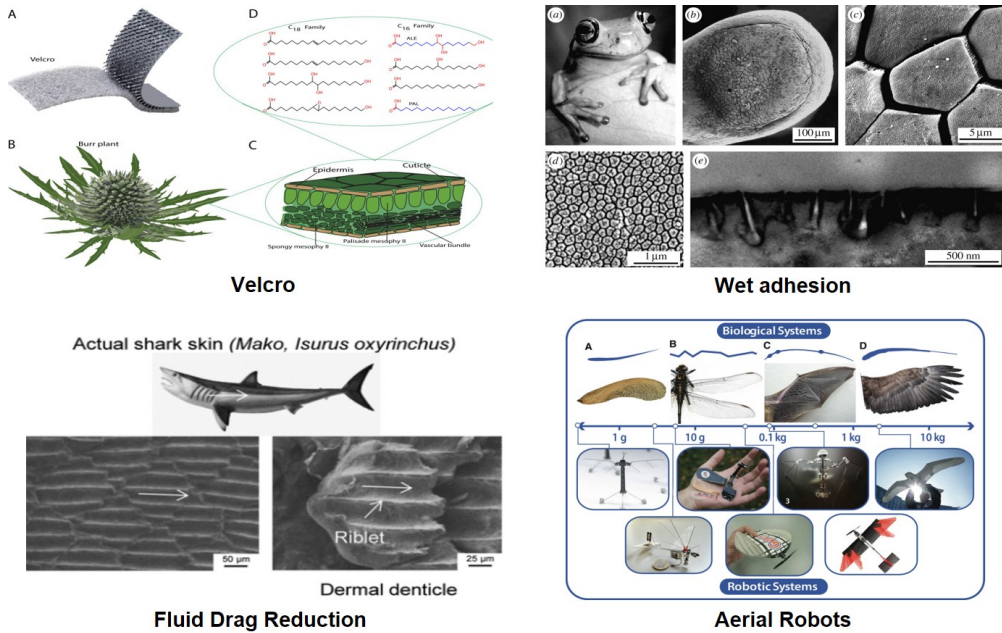


Figure 1.1: Biomimetic researches [1,3,6,7]

In a broad sense, cameras can be described as a device that imitates human vision. It is widely used in everyday life, closely integrated into various devices such as smart-phones, cars, and CCTV systems, and is designed to resemble human vision, making it highly intuitive. It is composed of a single lens and a single sensor. The human eye and a camera are remarkably similar. Light enters the human eye through the cornea, which is the first part that receives light. After passing through the cornea, light is filtered through the iris and reaches the retina, located inside the eye, surrounded by the sclera and choroid, forming an image. Similarly, in case of a camera, light passes

through the lens and then the aperture that is controlled by a diaphragm, and reaches the image sensor inside the dark camera body. This process allows the camera to capture the shape of objects and acquire an image.

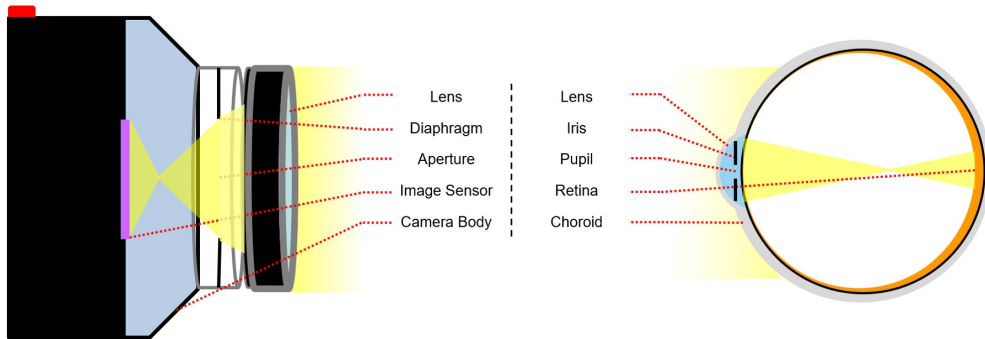


Figure 1.2: Comparison of human eye and a camera

Although human beings are one of the most successful living organisms in utilizing visual ability for survival, there is still a lot to learn from nature. For example, eagles are well-known for its superior ability to capture a small prey from a distance, chameleons can see surroundings with minimal blind spot, and cuttlefish with its w-shaped pupil that enables high visual acuity in horizontally illuminated light [8, 9, 10, 11]. If these characteristics could be incorporated into cameras, it would enable the acquisition of a wider range of information from the camera. In the quest for survival, there is another species that has developed vision, and that is insects. Although the visual range of insects is generally shorter than that of vertebrates, they have evolved specific characteristics due to their species' needs. One notable feature is their wide field of view, allowing them to perceive a broad range of their surroundings. Additionally, insects possess rapid reaction times, enabling them to respond quickly to stimuli in their environment.

1.1.2 Vision system

Human eye

Vision is the most important sensory system in survival for many living organisms. In most cases, any living organisms have more than one eye for stereopsis to obtain spatial and depth information from its surroundings. Binocular vision system is one of the most important characteristics of the human eye vision system. It is an ability to perceive a single, three-dimensional image of the world using both eyes simultaneously. This is made possible by the horizontal placement of the eyes allowing them to overlap their visual fields providing two different aspects of a single object. The slight difference between the images seen by each eye is called binocular disparity that provides information about depth and distance perception, as in Figure 1.3. Another benefit of having a binocular vision is that it offers a broader field of view. For an example, the maximum horizontal field of view is approximately 190° when seen by both eyes whereas single eye can observe around 120° . Within this range, around 120° form the binocular field of view, which is visible to both eyes [12]. The brain uses this information to determine depth and distance, as objects that are closer to us will have a larger disparity than objects that are further away.

When light enters the eye, it is focused onto the retina by the lens. The cones in the fovea are responsible for high-acuity vision and are most sensitive to light. The rods in the periphery of the retina are more sensitive to low levels of light and are responsible for peripheral vision. The information gathered by the retina is then transmitted to the brain via the optic nerve. The information from the left eye is sent to the right hemisphere of the brain, while the information from the right eye is sent to the left hemisphere of the brain. The two hemispheres then work together to create an unified image. The retina contains specialized cells called photoreceptors that convert incoming light into electrical signals that can be processed by other cells in the retina and eventually transmitted to the brain. The basic structure of the retinal cir-

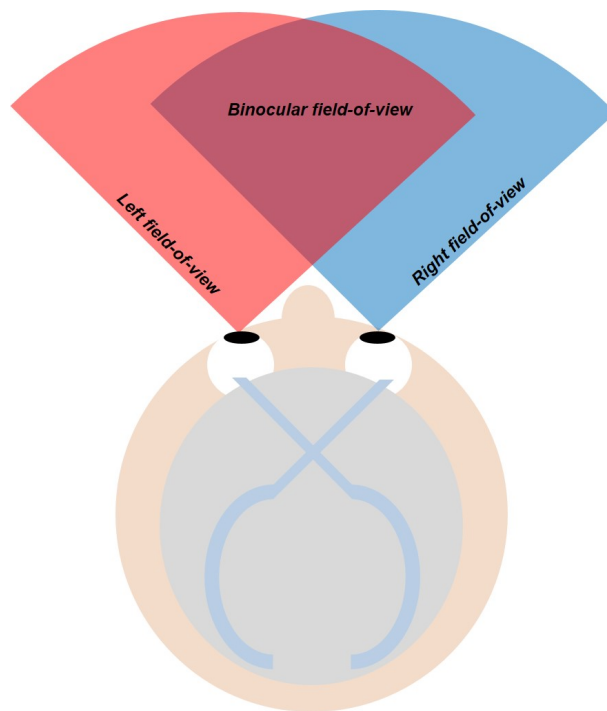


Figure 1.3: Binocular Field-of-View of human eye. The overlapping region provides depth information.

cultry system consists of a series of layers, each containing different types of cells that perform specific functions. The outermost layer of the retina contains the photoreceptor cells, which come in two types: rods and cones. Rods are more sensitive to light and are responsible for detecting dim light and motion, while cones are responsible for color vision and high visual acuity. The signals generated by the photoreceptors are transmitted to a layer of cells called bipolar cells, which help to refine the signals and transmit them to another layer of cells called ganglion cells. Ganglion cells are the output neurons of the retina, and their axons form the optic nerve, which carries visual information to the brain. In addition to these three main cell types, the retina also

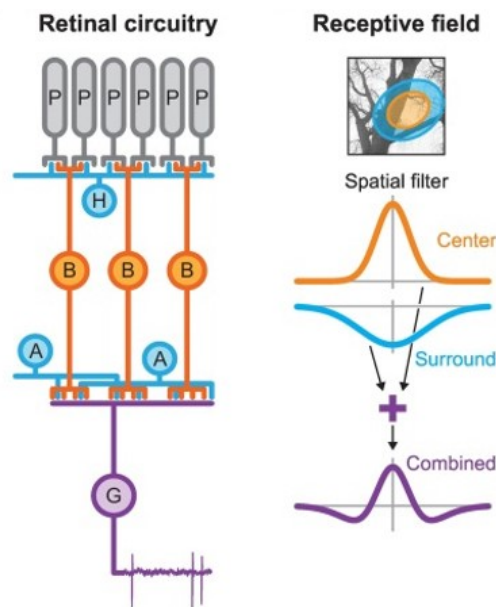


Figure 1.4: Human retinal circuitry ^[14]

contains a variety of other cells that modulate and shape the signals generated by the photoreceptors, bipolar cells, and ganglion cells. These include horizontal cells that integrate signals across neighboring photoreceptors, and amacrine cells which modulate the activity of bipolar and ganglion cells. These two types of cells create signals called center and surround, based on the global motion, local motion, and differential

motion signals which increase the contrast so that the brain can obtain motion vector information from the sequential stimulation [13, 14].

Insects eye

While human beings and other vertebrates rely on visual distance and spatial resolution to focus on a specific object, insects developed their vision system to observe wider and faster. An interesting and well-known feature of the eyes of the insects is that they have the compound eye system in place of the single-aperture eyes of vertebrates. Compound eye consists of more than hundreds ommatidia, each of which consists of a cornea, lens, and photoreceptor cell. Compared to the single-aperture eyes of human being, it provides wide viewing angle and the ability to detect fast moving objects, although it has poor image resolution.

There are two types of compound eyes; superposition and apposition. In superposition eyes, the lenses of the ommatidia are not in direct contact with the photoreceptor cells, although they share a layer of pigment cell for light-screen. The light passing through the lens is split into two or more images, which are then focused onto different parts of the photoreceptor cell. This allows for a wider field of view and a higher sensitivity to motion. Apposition eyes also consist of multiple ommatidia, but the lenses of the ommatidia are in direct contact with the photoreceptor cells, meaning that each ommatidium is surrounded by a pigment cell layer, producing a single, relatively sharp image. Apposition eyes are better suited for visual acuity and color vision than superposition eyes, but they have a more limited field of view.

Nonetheless, eyes of insects have an extremely wide field-of-view compared to that of human [15, 16]. For an example, honeybees have around 280° of field-of-view, which is large enough to cover almost everything around them [17]. Therefore, it would be very beneficial to incorporate these advantages into existing systems such as robotic vision.

In their vision system, the complicated retinal circuitry for motion vector does

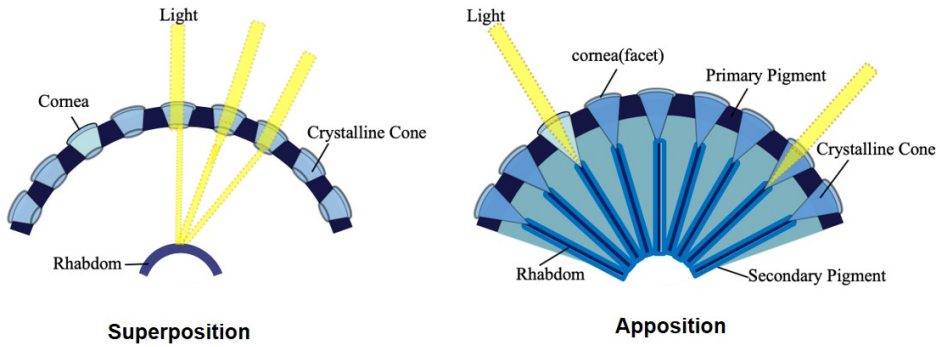


Figure 1.5: Two major types of the compound eye

not exist. Instead, they rely on minimal visual information to create optic flow. Once the light enters the insect's eye, rapid motion sensitive neuron called Lobula Plate receives the motion signal and integrated to be sent to the thoracic interneurons along with signals from other sensory parts [18, 19, 20, 21]. This alternative retinal circuitry enables them to observe moving objects and reflect against it faster [20].

1.1.3 Small robot applications

Recent advances in the field of computer vision have enriched our lives with autonomous cars, drones, humanoids, and surveillance cameras, etc. Combined with other distance sensors such as ultrasonic sensors, infrared distance sensors, LiDAR, or Time of Flight(ToF) sensors, applications and potential of the vision system are limitless. However, the combination of different sensors is restricted to large robots or vehicles due to its requirements such as space for the equipment, extra power for those sensors, and computational resources. Therefore, equipping both the image sensor and distance sensor in small machines or endoscopy applications for narrow spaces is greatly limited. When the compound eyes of the insects are adopted as computer vision system, however, the problem could be resolved since it could offer multiple visions for an image sensor. This artificial compound eye system enables multi-ocular

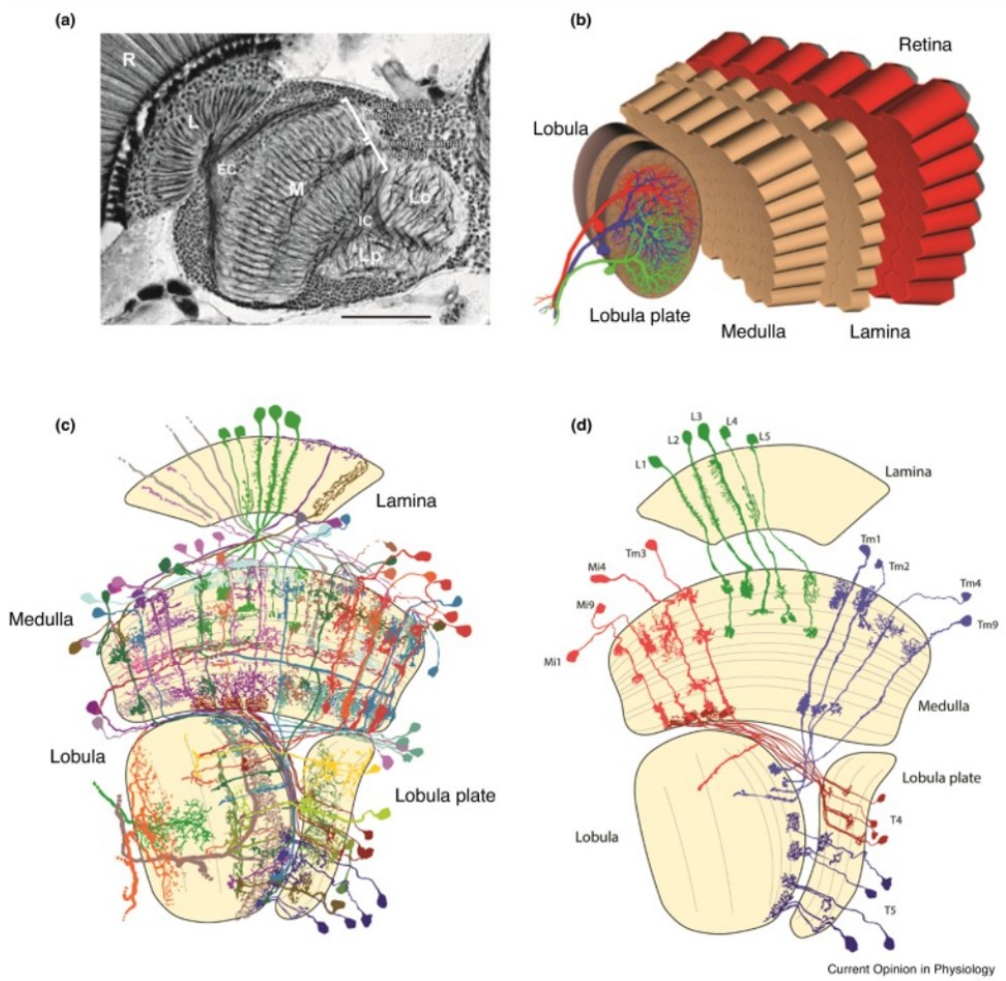


Figure 1.6: Lobula Plate of insects [20]

vision that offers even more aspects of a single object that goes beyond binocular system. With these multiple images taken at different aspects, it would be able to obtain spatial information simply by comparing two small sub-images.

Moreover, the advancement of the computer vision system brought changes to the shape of the image sensors. The complementary metal–oxide–semiconductor(CMOS) image sensor has been researched and fabricated with the curved surface instead of the conventional flat surface. The curved image sensors are expected to improve the resolution, aberration, and illumination of the flat sensor, along with the reduced size and complexity of the whole vision system [22, 23, 24]. Therefore, the application of the curved image sensor to the vision system with the compact size and high performance can further strengthen its potential as a future image sensor system, leading to a development of a curved artificial compound eye system as well.

1.2 Micro-Lens Array

Micro-Lens Array, or MLA is a device that consists of many small lenses arranged on a plane. It is used in imaging systems to enhance the performance of image sensors as supplementary optical components or as a primary camera lens for imaging. By focusing light onto an image sensor, a micro-lens array can increase the amount of light that is captured and improve the overall image quality. Micro-lens arrays can also be used to reduce crosstalk between adjacent pixels in an image sensor, which can lead to better color accuracy and contrast. Other applications include 3D imaging, holography, and photovoltaics. Combined with biomimetics, MLAs are often considered as bio-inspired lens system, or artificial compound eye, as it exhibits similar aforementioned advantages and disadvantages when it was utilized as a primary lens for an imaging system, especially for robotic vision.

Micro-lens arrays, therefore, are great apparatus for the compact computer vision system and the curved CMOS sensor technology application due to the additional spatial information it offers. The spatial information can be obtained since the multi-perspective imaging system provides multiple images of a target in one image plane along with a wide field of view[25, 26]. To recreate the spatial information acquisition and wide field-of-view, many studies have presented various fabrication methods of the micro-lens arrays by mimicking the structure of the superposition compound eye of the insects [27, 28]. However, conventional micro-lens arrays do not resolve the optical interference from the neighboring micro-lenses which saturates the light intensity received on the image sensor, and only provides a very short visual range of a few tens of millimeters.

1.2.1 Micro-lens array research

To reduce the optical interference from adjacent lenses and external light sources, a few studies have actualized the light screening layer which corresponds to the pigment cell

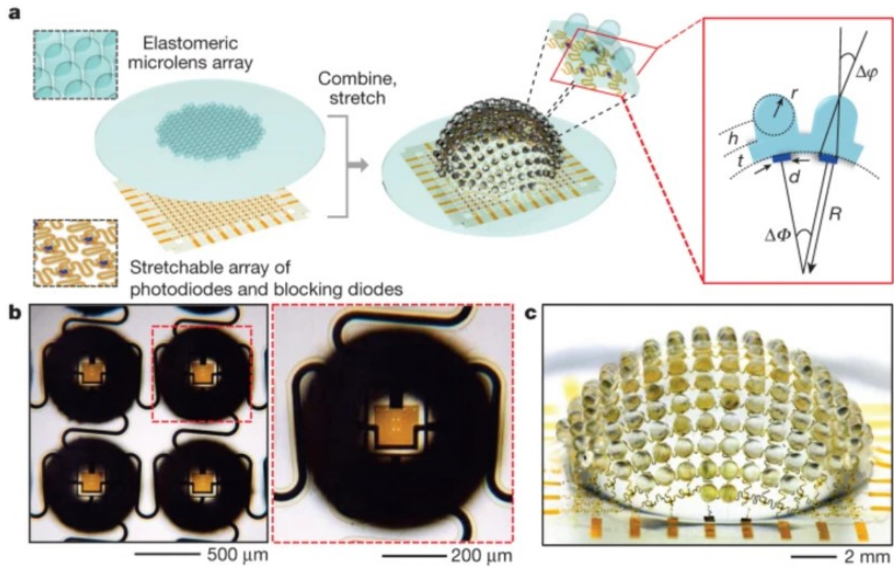


Figure 1.7: Artificial compound eye system that imitated bee's eye for wide field-of-view [27]

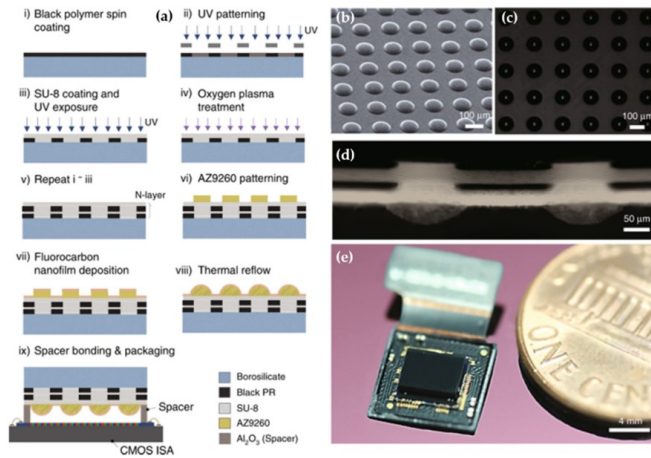


Figure 1.8: Artificial compound eye system with pigment cell^[30]

of the compound eye [29, 30, 31, 32, 33]. They adopted the light screen layer or barrier around each micro-lens to rectify the optical interference. Since the light screen around each lens functions as a wide aperture, the light screen increased the visual range of them. However, they lack a real aperture, which provides a further depth of field, and structural improvements, resulted in a short visual range of a few tens of centimeters. However, due to its short-sighted vision and optical interference from adjoining micro-

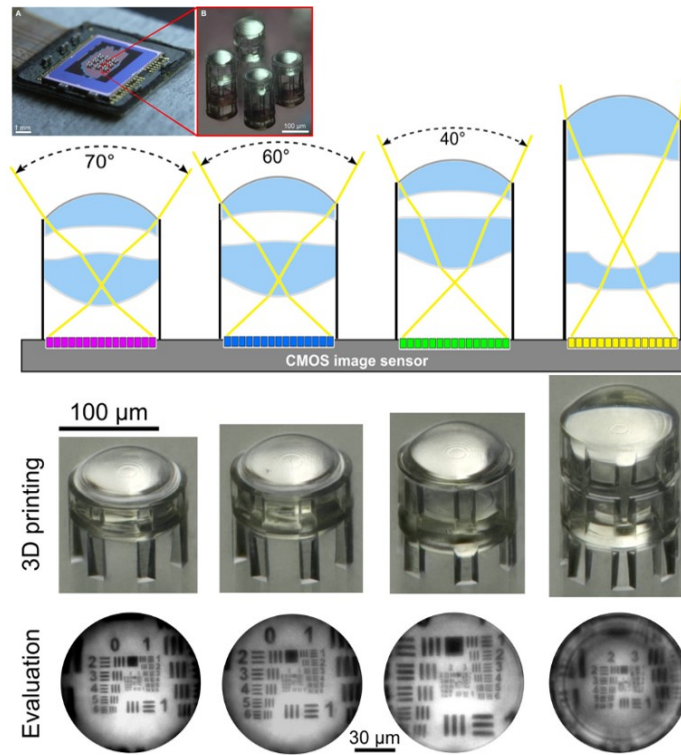


Figure 1.9: Foveated vision eagle eye micro-lenses^[34].

lenses, it has not been actively adopted to the current computer vision system. To increase the visual range of the micro-lenses, a research combined "foveated vision" from eagles' eye and insects' compound eye multi-aperture system[34]. This research greatly improved the visual range by 1 meter through a unique lens design that imitates the eagles' eye. It demonstrated the versatility of the micro-lens multi-aperture system

for small robots by improving the visual range through structural design. However, this study did not resolve the optical interference problem from adjoining lenses and external light sources since the materials used for the foveated vision are transparent. Therefore, there is ongoing effort to establish a pragmatic micro-lens array optical system. The optimal micro-lens array system will provide a better visual range and wider field-of-view while it can be located in smaller spaces or small machines and can fit on any curved CMOS image sensors for a superior optical performance.

Another notable research is 3-dimensionally designed artificial compound eye. The micro-lens array from the research contains complicated optical components including field lens array, freeform lens array, aperture array, and micro-lens array with its 'channels' around them [26]. This micro-lens array offers about 32 cm of long visual range with 87 °of overall field-of-view, along with aperture stop at the right after the first layer for reduced aberration and light scattering as shown in 1.10.

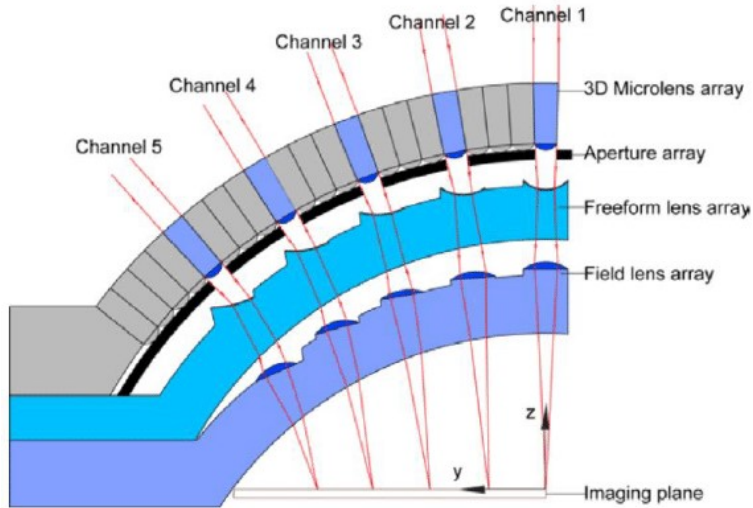


Figure 1.10: Structure of the three-layer 3D compound eye [26]

The only downside of this system is that it requires extra image stitching process for recognition of the target object, since it does not provide overlapping images as

shown in 1.11. The images from individual lenses can show only a small portion of the whole, which means it is not suitable for obtaining further spatial information from the resulting image.

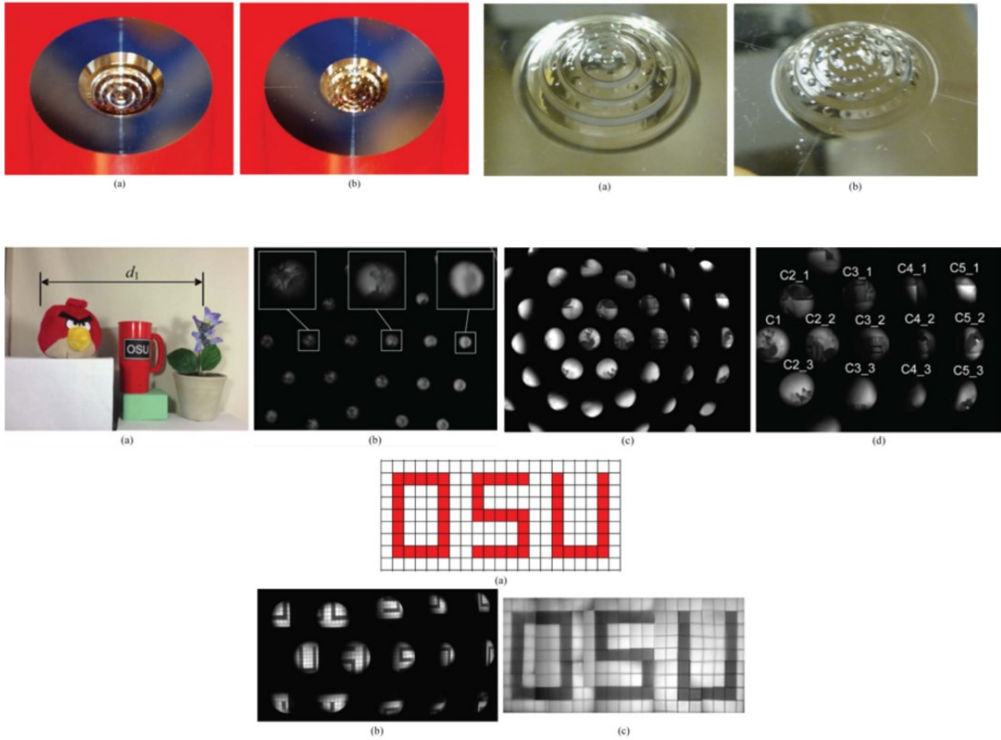


Figure 1.11: Micro-lens Array not providing enough overlapping field-of-view ^[26]

In summary, for a biomimetic micro-lens array: 1) It should have enough overlapping areas between images in a superposition form rather than apposition, 2) It should enable observing the front view with a wider field of view compared to conventional micro-lens array cameras, 3) It should have an aperture to reduce noise from nearby lenses, and 4) It should be able to be designed with a curved shape to achieve a wider field of view. These characteristics would allow a more advanced and versatile camera, capable of acquiring a broader range of information.

1.2.2 Materials and methods for Micro-lens array fabrication

Materials and fabrication method of micro-lens arrays vary, although there are some of the typical materials and methods that are widely used. Typical micro-lens array materials include transparent polymeric materials such as PDMS, PMMA, SU-8, etc., combined with Micro Electro Mechanical Systems (MEMS) or nanotechnology fabrication process for precise design and manufacturing of the lenses.

Methods

Among various methods of manufacturing a micro-lens array, the most representative method involves use of a mold. A mold can be made by physically grinding a material using high-precision machine milling, it can also be made by chemical etching [35], or by melting circular cylinder-shaped photoresist through thermal-reflow to produce a hemispherical mold [36]. After creating a mold, liquid-state lens material is poured into the mold and then it could be hardened, or if it is in solid-state material it could be handled by applying high pressure and heat to the mold. While this method offers the advantage of achieving intricate designs and customization, it is important to note that it is not a new technique. In fact, it is currently the most commonly employed method for fabricating micro-lens arrays. Its widespread usage is a testament to its effectiveness and suitability for producing micro-lens arrays with intricate features and desired designs.

Alternatively, as in the foveated vision micro-lens array's case, one can also use 3D printing or super inkjet printing for formation of micro-lens arrays. As it involves the fabrication of stacked small and intricate micro-lens arrays, there is room for various approaches. However, the substrate used must be compatible with 3D printing, and as discussed in the paper, it is crucial to directly print onto the CMOS sensor without causing any damage to the camera. Therefore, careful consideration is required to ensure the material and printing process are compatible with the specific requirements of protecting the camera and achieving successful fabrication.

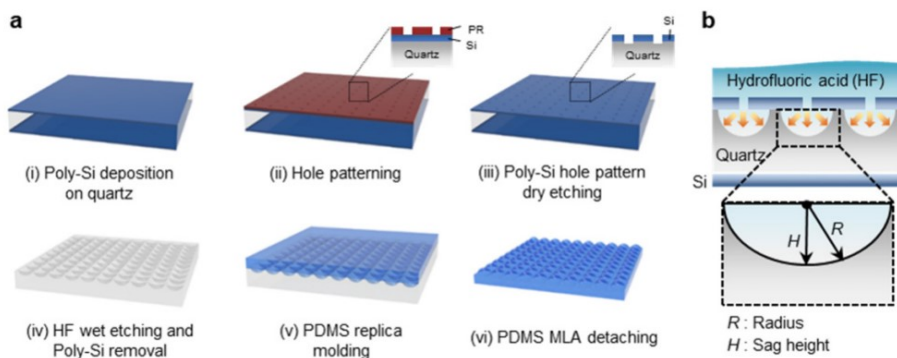


Figure 1.12: Chemical etching method to produce lens shape ^[35]

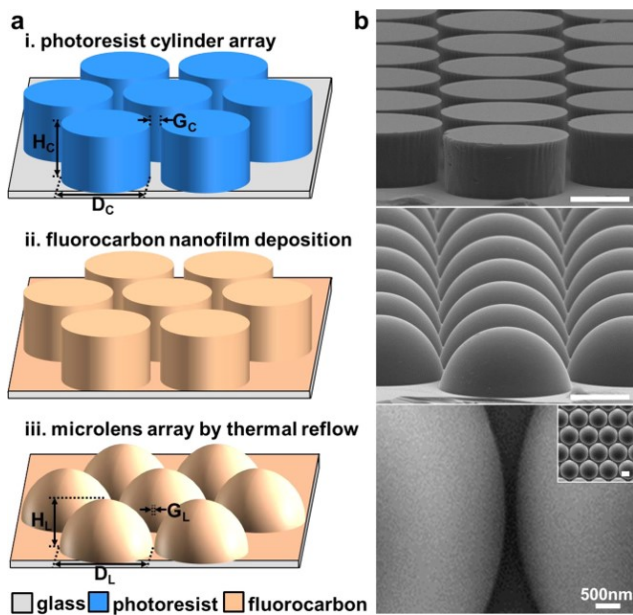


Figure 1.13: Thermal-reflow method to produce lens shape ^[36]

Material

Vision system for small robots not only require small size but also demand light weight for prolonged remote exploration under limited power supply. Polymeric materials, therefore, are great candidates since they have relatively low specific density since they have 0.9 - 1.41 g/cm^3 , while glasses have 2.2 - 2.64 g/cm^3 of density [37, 38]. Typical Micro-lens Array materials include Polydimethylsiloxane (PDMS), negative photoresist such as SU-8, Poly(methyl methacrylate (PMMA), UV resins, etc. Among these materials, PDMS and Cyclic Olefin Copolymer (COC) were investigated due to their ease of process and high transparency.

PDMS is a silicone-based polymer. PDMS has a wide range of applications due to its unique properties, including its high chemical resistance, thermal stability, and low surface energy, etc. It is commonly used in the medical, pharmaceutical, and electronics industries, as well as in soft lithography. Another great application of the material is in optics. Since it is cost-effective, easy to process, highly transparent with more than 90%, and refractive index of 1.43, which is good enough to be used as a lens material [39, 40, 41]. Another important characteristic of the PDMS is that it is a flexible material. Therefore, it is expected to fit on any curved surface regardless of the curvature of the image sensor, making it a versatile micro-lens array.

COC is one of the thermoplastic polymers that consist of repeating units of cyclic olefin monomers. These monomers are typically derived from cyclo-olefins such as norbornene and ethylene. COC is known for its excellent transparency, high thermal stability, and low water absorption properties, which make it suitable for a wide range of applications. Its high optical clarity and low birefringence make it an ideal material for applications in the optics, including lenses, prisms, and light guides. COC can easily be molded into complex shapes, making it a popular material for injection molding applications. Although its transparency (85%) is lower than that of PDMS [42], its high thermal stability and chemical resistance are taken into account as well, since PDMS-based lenses are prone to be damaged from external stress, making the system

vulnerable.

Studies that investigated the COC-based MLA fabricated the lenses through the injection molding method [43, 44, 45]. However, injection molding requires huge facilities that require spacious room for particular purpose of creating a COC-based product, which is not possible in a laboratory environment. Therefore, compression molding method using a heat-press was considered based on the fact that the COC is a thermoplastic.

1.2.3 Basic Optics

Snell's Law

As Micro-lens Arrays are optical components that collimate light to the image sensor, some of the basic formulas and basic knowledge are needed to describe and understand its behavior. The behavior of rays traveling from a medium to another can be explained by Snell's law, also known as Law of refraction, as shown in Figure 1.15 and described in Equation 1.1, where θ_1 and θ_2 are the incident angle and refracted angles, respectively, n_1 and n_2 are the refractive indices of each medium. The law states that the ratio of the sines of the angles of incidence and refraction is equal to the ratio of the refractive indices of the two materials. The law applies to any materials as long as they are transparent. When the ray passes from a material with a lower refractive index to a material with a higher refractive index, the angle of refraction is smaller than the angle of incidence. Conversely, when light passes from a material with a higher refractive index to a material with a lower refractive index, the angle of refraction is larger than the angle of incidence.

$$\sin\theta_1 \cdot n_1 = \sin\theta_2 \cdot n_2 \quad (1.1)$$

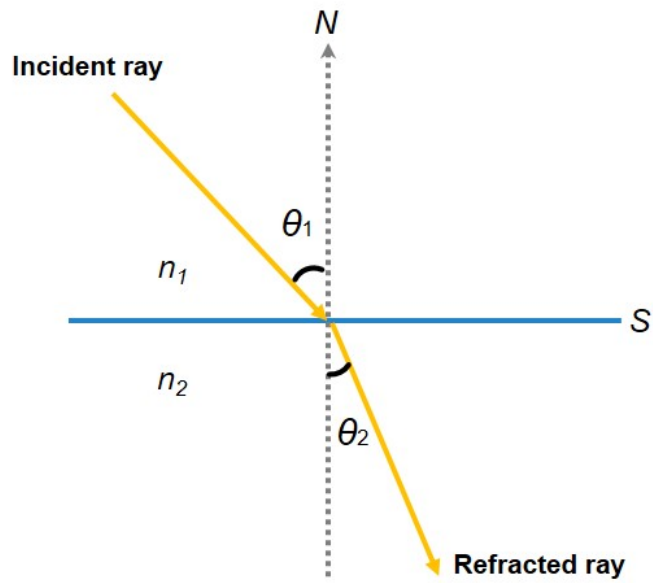


Figure 1.14: Ray refracting at a flat surface

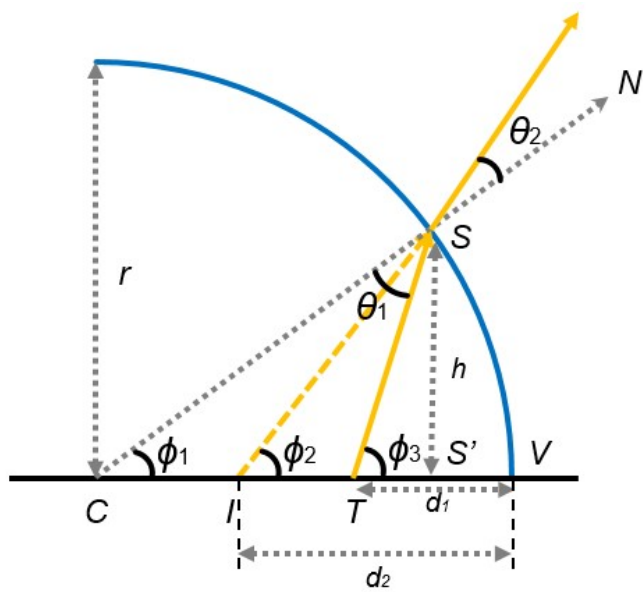


Figure 1.15: Ray refracting at a concave spherical surface

Lens maker's equation

Snell's law can also be applied to any curved surfaces such as lenses. Consider a refracting curved surface centered around a point C with a curvature of radius r as in Figure 1.15. The ray from a target source point T heads toward an arbitrary point S on the surface at an incident angle θ_1 , according to the Snell's law (Equation 1.1). The refracted ray and the axial ray intersects at an image point I . $\triangle CIS$ produces an exterior angle $\phi_2 = \phi_1 + \theta_2$, since θ_2 makes a vertical angle on the θ_1 side, and $\triangle CTS$ makes another exterior angle $\phi_3 = \phi_1 + \theta_1$ in the same manner. Substituting both $\sin\theta_1$ and $\sin\theta_2$ for the corresponding angles, now we have:

$$(\phi_3 - \phi_1) \cdot n_1 = (\phi_2 - \phi_1) \cdot n_2 \quad (1.2)$$

ϕ_1 through ϕ_3 can be geometrically expressed as tangents, namely $\tan \phi_1 = \frac{h}{r}$, $\tan \phi_2 = \frac{h}{d_2}$, and $\tan \phi_3 = \frac{h}{d_1}$. Using small angle approximation, the line segment from the perpendicular foot of the point S onto the paraxial axis (point S') to the vertex of the curve (point V), namely \overline{CV} can be neglected, making $r \approx \overline{CS'}$. Using the small angle approximation again, $\tan \phi_n \approx \phi_n$. Therefore, we can simply rewrite Equation 1.2 as following:

$$\left(\frac{h}{d_1} - \frac{h}{r}\right) \cdot n_1 = \left(\frac{h}{d_2} - \frac{h}{r}\right) \cdot n_2 \quad (1.3)$$

By applying the *sign convention for lenses*, we may also obtain the following relationship depending on the positive/negative distances for real objects/images, virtual objects/images, and the radius of curvature for concave/convex settings:

$$\left(\frac{n_1}{d_1} - \frac{n_2}{d_2}\right) = \frac{n_1 - n_2}{r}, \text{ or } \left(\frac{n_2}{d_1} + \frac{n_1}{d_2}\right) = \frac{n_2 - n_1}{r} \quad (1.4)$$

For thin lenses that have two refractive surfaces, the *sign convention for lenses* for the first surface with curvature r_1 that the ray enters initially becomes:

$$\left(\frac{n_1}{d_{11}} + \frac{n_2}{d_{12}}\right) = \frac{n_2 - n_1}{r_1} \quad (1.5)$$

and Equation 1.6 for the second surface,

$$\left(\frac{n_2}{d_{21}} + \frac{n_1}{d_{22}}\right) = \frac{n_1 - n_2}{r_2} \quad (1.6)$$

Assuming that the lens is surrounded by the same medium with its refractive index n_1 , the second object distance d_{21} becomes $d_{21} = d_{lens} - d_{12}$, where d_{lens} represents the thickness of the lens. Since we're assuming a very thin lens, thin-lens approximation applies which neglects the thickness of the lens, $d_{21} = -d_{12}$ holds true. By substituting d_{21} in Equation 1.6 and adding the modified Equation 1.6 to Equation 1.5, the term $\frac{n_2}{d_{12}}$ cancels out on both equation, resulting:

$$n_1 \cdot \left(\frac{1}{d_{11}} + \frac{1}{d_{22}}\right) = (n_2 - n_1) \cdot \left(\frac{1}{r_1} - \frac{1}{r_2}\right) \quad (1.7)$$

Dividing both sides by n_1 and by the definition of the focal length which is the *image distance for an object at infinity*, finally we have the *lensmaker's equation* as shown in Equation 1.8, where focal length of the lens is denoted by f .

$$\frac{1}{f} = \left(\frac{n_2 - n_1}{n_1}\right) \cdot \left(\frac{1}{r_1} - \frac{1}{r_2}\right) \quad (1.8)$$

The *lensmaker's equation* provides the focal length of the thin-lens given the refractive indices of the lens and the environment, depending on the curvature of the both surfaces of the lens. In this research, however, since the lenses are all in the shape of the plano-convex lens which has an infinity value ($r \rightarrow \infty$) of curvature on one side, the terms can be reduced even further, which will be discussed later.

1.3 Conclusion and Goal

This dissertation emphasizes the use of micro-lens arrays as visual sensors for small robot applications. Various micro-lens arrays suitable for curved CMOS have been fabricated. In line with the concept of biomimicry, not only the lens itself but also pigment cells were incorporated through the inclusion of a light-screen in the fabrication

process. Various aspects to consider when fabricating the micro-lens array in a future 3D curved form were addressed, utilizing the simple optical formulas mentioned earlier. Furthermore, the advantages arising from the utilization of micro-lens arrays, such as acquiring spatial information through multi-aspect imaging, were discussed. Several applications utilizing the fabricated micro-lens array were also presented, emphasizing its use as a visual sensor for small robots.

Chapter 2

Fabrication of artificial compound eyes

2.1 PDMS-PVC Micro-lens Array

2.1.1 Introduction

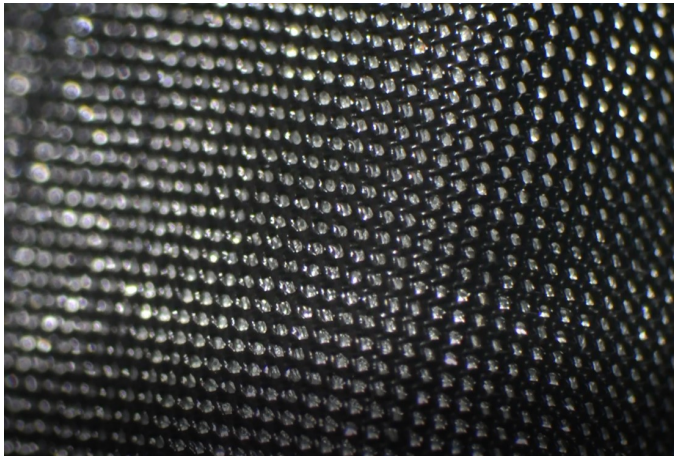


Figure 2.1: Picture of the PDMS-PVC MLA

When producing a curved micro-lens array, a decision must be made whether to fabricate it in a curved state or to manufacture it in a flat form and then shape it into a curved shape. However, if it is fabricated in a curved state, it comes with significant

constraints when using existing useful equipment such as spin-coaters or laser cutters. Therefore, it is advantageous to initially manufacture it in a flat form and then shape it into a curved shape in terms of the manufacturing process. This implies that the main material should be flexible and easily bent, rather than rigid materials. Consequently, PDMS was chosen as the primary material for the lens, and PVC was selected as the material for the light-screen layer.

In this section, the fabrication method of a micro-lens array using PDMS and PVC is introduced, along with the outcomes achieved through its utilization.

2.1.2 Materials and Method

Materials for the PDMS-PVC micro-lens array includes polydimethylsiloxane (PDMS, Sylgard 184, Sigma-Aldrich, United States) with 10:1 of ratio is used for the micro-lenses, PVC with 40 μm thickness, microscope glass slide (M08-660-147, LK Lab Korea, South Korea) for fabrication substrate, and a custom-made vacuum box.

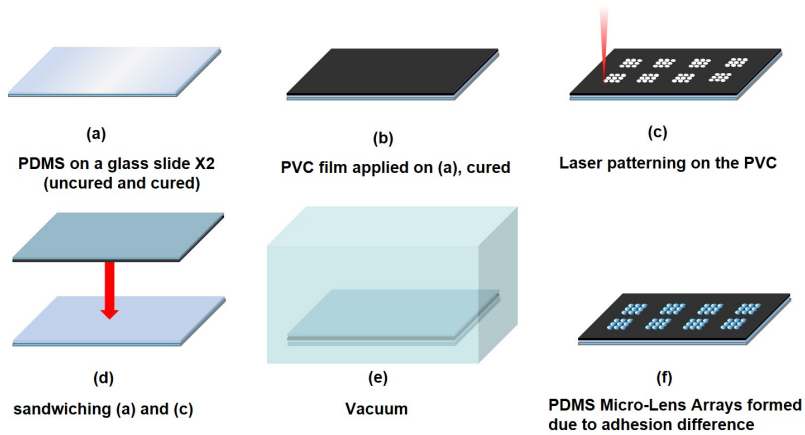


Figure 2.2: Fabrication Process of the PDMS-PVC MLA.

The fabrication process for the PVC-MLA involves several steps as illustrated in Figure 2.2. 1) Spin-coating PDMS on top and bottom substrates: Both the top and bottom substrates are coated with a 10:1 ratio of polydimethylsiloxane (PDMS) us-

ing a spin-coating technique. The PDMS is evenly spread on the substrates, forming a thin layer. 2) Curing the PDMS layer: After spin-coating, the substrates with the PDMS layer are cured at 100 °C for 30 minutes. This curing process helps solidify and stabilize the PDMS layer. 3) wrapping PVC layer to the top substrate: A PVC layer is carefully added to the top substrate, ensuring there is no air trapped between the PDMS layer and the PVC layer. 4) Drawing patterns for the micro-lens array: Using a UV laser, a set of patterns for the micro-lens array is drawn on the top substrate. The patterns define the shape and arrangement of the individual lenses in the array. 5) Applying an additional uncured PDMS layer on the bottom substrate: On top of the previously cured PDMS layer on the bottom substrate, another layer of thin PDMS is applied. This additional layer remains uncured at this stage. 6) Laying the top substrate upon the bottom substrate: The top substrate with the PVC layer and the drawn micro-lens array is carefully placed on top of the bottom substrate with the uncured PDMS layer. 7) Placing in a vacuum chamber: The assembled substrates are placed in a vacuum chamber for a duration of 4 hours. The vacuum environment helps remove any trapped air bubbles and enhance adhesion between the top and bottom substrates. The steps involve the filling of the indented pattern on the top substrate with an uncured PDMS layer from the bottom substrate. Subsequently, the carefully adjusted micro-lens patterns on the top layer (40 μ m thin) induce a capillary phenomenon within the uncured PDMS, resulting in the transformation of the uncured PDMS into a lens-like shape over a few hours. Once the PDMS attains its lens-like shape, the uncured PDMS layer undergoes curing while maintaining the shape within each indentation. Finally, the substrates with PDMS are removed, leaving behind the PVC layer and the cured PDMS (which initially was called "uncured PDMS") layer in their lens-like formed state together. This process is made possible due to the superior adhesive strength between the substrate and the cured PDMS, which is significantly stronger than the adhesive strengths between the cured PDMS and PVC layer, or between the uncured PDMS and the cured PDMS layer. Figure 2.3 shows the produced micro-lens array,

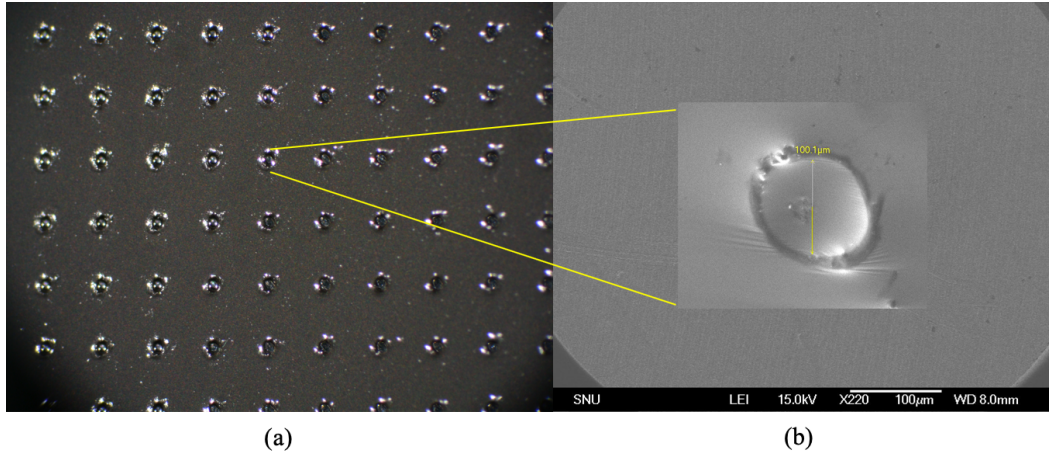


Figure 2.3: The fabricated micro-lens array **(a)** Top-view of the micro-lens array. **(b)** An individual micro-lens captured using SEM.

which includes a PVC screening layer. Each lens within the array measures $100\ \mu\text{m}$ in diameter and $60\ \mu\text{m}$ in height, with a spacing of $300\ \mu\text{m}$ between them. Due to the elasticity of the processed PVC film, the micro-lens array can be easily manipulated and shaped according to requirements. However, in order to apply it onto a flat surface, a planarization process becomes necessary.

As depicted in figure 2.4, the fabricated micro-lens array is flattened and affixed to a 3D jig for further adjustments. After the fabrication of the PVC micro-lens array, it becomes compatible with various commercially available CMOS sensors. Figure 2.4 showcases a specially designed jig employed for loading the PVC micro-lens array film onto the CMOS image sensor module. The micro-lens array is affixed at the center of a 3D printed cover, which is then assembled using screws and spiral springs positioned at each corner. These spiral springs serve the purpose of preventing any movement of the cover part towards the sensor section, while the screws secure the cover part in place to prevent detachment. This setup allows for precise adjustment of the distance between the micro-lens array and the sensor by tightening or loosening the screws.

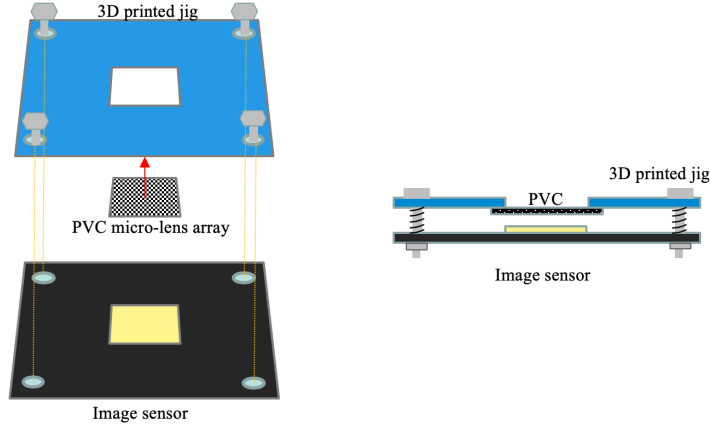


Figure 2.4: The schematic of the imaging system setup using 3D printed jig.

2.1.3 Result

The comparison images of the printed USAF 1951 pattern captured from different subset locations within the micro-lens array are depicted in Figure 2.5. Specifically, the images obtained from the left-most subset exhibit a slight rightward shift in the numbers (-1 (top) and 0 (bottom)) that indicate the center of each lens, in comparison to the image obtained from the center subset lens. By leveraging this disparity observed between the image subsets, we were able to calculate the distance of an object from the compound eye camera system. This spatial information provides data that can be utilized for achieving a more precise object localization during post-image processing.

To calculate the distance of an object from the image sensor, certain assumptions were made. Firstly, it was assumed that the distance ‘d’ between each micro-lens ($500\ \mu\text{m}$) is negligible compared to the distance between the image sensor and the target object ‘D’ (2 cm). Additionally, it was considered that the difference between θ_1 and θ_2 is also negligible. θ_1 can be determined using Equation 2.6 and calibration process, which will appear in the PDMS-PTFE section again.

Under these conditions, the distance of an object from the image sensor can be calculated using the distance between each micro-lens, the focal length, and the dis-

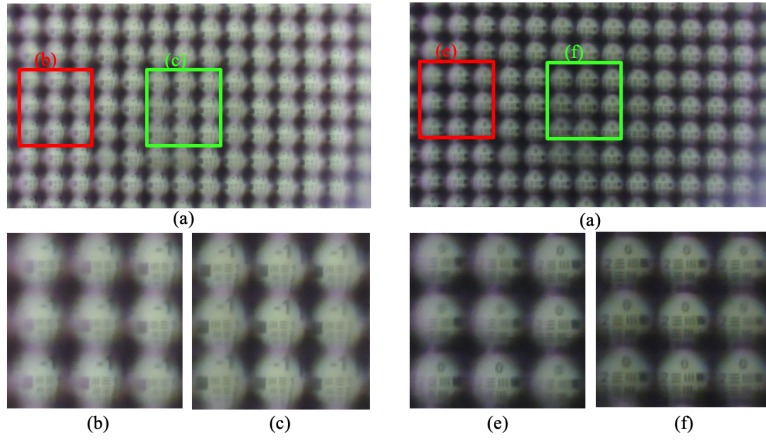


Figure 2.5: Raw image taken using fabricated the micro-lens array. **(a)** Image of USAF 1951 for pattern group '-1'. **(b)** Leftmost 3x3 sub-image of (a) **(c)** Middle 3x3 sub-image of (a) **(d)** Resulting image of USAF 1951 for pattern group '0' **(e)** Leftmost 3x3 sub-image of (d) **(f)** Middle 3x3 sub-image of (d)

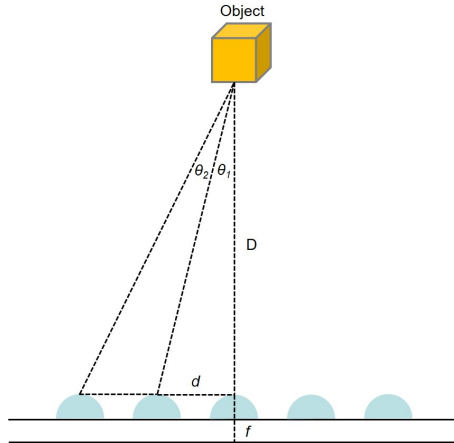


Figure 2.6: Schematics for distance measurement.

tance of image mismatch. For instance, in Figure 2.5-(a), the left-most image exhibits a 1cm x 1cm black reference box that is approximately 0.01 mm away from its original position, as seen in the center image of the middle subset. Given a focal length of 80 μm and a comparing micro-lens distance of 2.5 mm (since each lens is 500um apart), the distance from the object can be calculated as 2cm, which aligns with the original setup.

$$\begin{aligned} \text{Disparity}_{ref} &= f \cdot \tan(\theta) = f \cdot d/D, \\ \text{Distance} &= f \cdot d / \text{Disparity}_{calibrated} \end{aligned} \quad (2.1)$$

The field-of-view (FOV) of the image system was determined by measuring it using a 3D printed half-circle goniometer, as depicted in Figure 2.7. The goniometer consists of black bars, with each gap between them representing a 10-degree angle increment, starting from the center bar. Observing a single micro-lens positioned at the center, it displayed an FOV of 80 $^\circ$, encompassing four bars on each side of the center bar. On the other hand, the left-most micro-lens exhibited five black bars starting from the center bar, while the rightmost micro-lens displayed another five bars on its side. This suggests that while a single micro-lens may have an FOV of 80 $^\circ$, in a micro-lens array configuration where multiple lenses are aligned, the FOV can be expanded up to 100 $^\circ$, thereby widening the overall field of view.

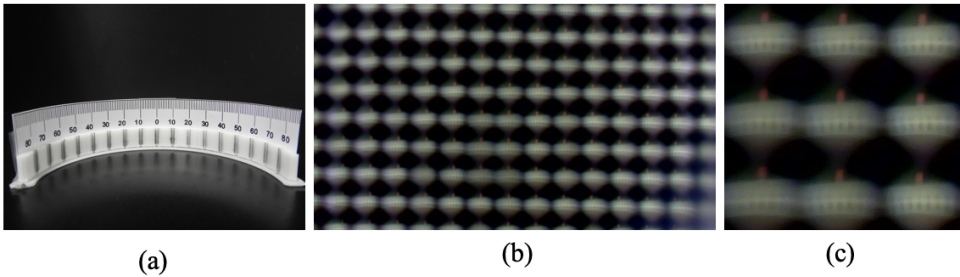


Figure 2.7: Field-of-View measuring setup and resulting images (a) 3D printed goniometer (b) Raw image taken using the micro-lens array (c) Middle 3x3 sub-image of (b)

2.1.4 Discussion and Conclusion

The fabricated PDMS-PVC micro-lens array was successfully produced and effectively captured subjects in imaging experiments. Since the PDMS-PVC micro-lens array was initially fabricated in a flat form, it is flexible and can be processed as needed through a curvature forming process using negative pressure, as shown in Figure 2.8. Alternatively, it can be directly placed on a curved CMOS sensor to serve as a lens. However, there is a challenge encountered during the fabrication process. PVC is vulnerable to heat while PDMS requires heating for solidification. When PVC and PDMS are combined, heating to around 100 °C for PDMS solidification causes the PVC to shrink and create random patterns of wrinkles, thereby affecting the fabrication yield. When PDMS was left on PVC film at room temperature for natural curing, it did not cure at all, even after 7 days. This issue can be addressed by considering alternative processes or selecting different materials.

Once it is fabricated in the hemispherical form without the issue of heating, it will result in a wider field of view, covering nearly 180 °, along with improved heat durability, opening up new possibilities for research and applications with its unique shape and functionality. In conclusion, this research offers a straightforward yet efficient approach to produce PVC micro-lenses.

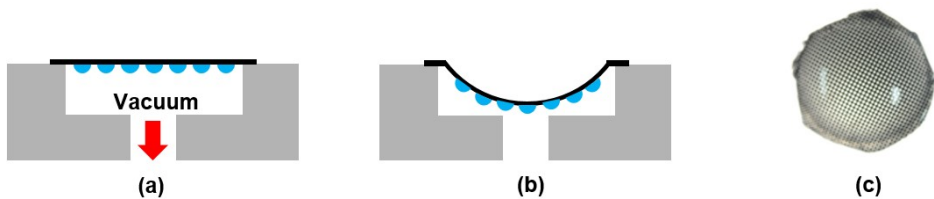


Figure 2.8: The schematics for the hemispherical PVC film micro-lens array. (a) Before the process. The Micro-lens Array is still in flat (b) Formation of the the hemispherical curvature using negative pressure (c) Resulting hemispherical PVC film micro-lens array

2.2 COC-CB Micro-lens Array

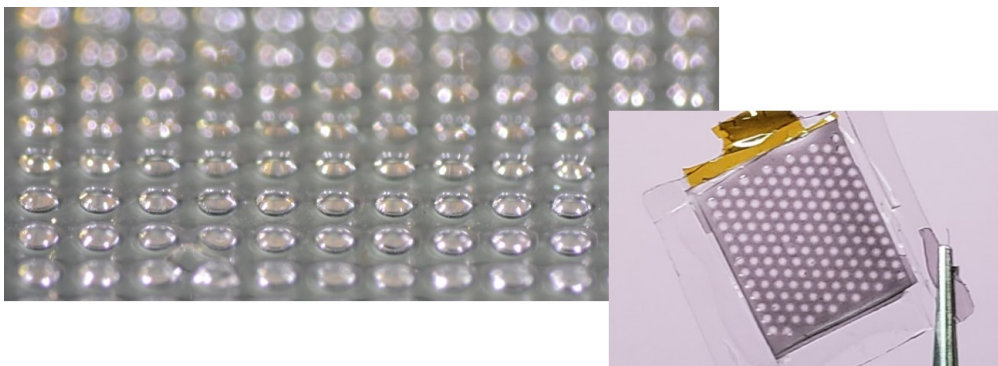


Figure 2.9: Picture of the COC-CB MLA.

2.2.1 Introduction

Cyclic olefin copolymer (COC) is a versatile thermoplastic polymer commonly employed in various fields such as medical packaging, food packaging, microfluidics, and optics. Recently, there have been discussions about the potential use of COC in implantable neural prosthetic devices [46]. COC stands out as a favorable material

for numerous applications due to its biocompatibility, thermoplasticity, high chemical resistance, exceptional optical transparency, and low water absorption rate. The thermoplasticity and excellent optical transparency of COC are particularly advantageous for optical applications. Previous studies have introduced COC-based micro lens arrays (MLAs) [43, 44, 45], predominantly utilizing the injection molding method recommended by manufacturers. However, in this research, we employed compression molding, which offers the advantage of requiring significantly less laboratory space for replication.

An important aspect of this study involves the incorporation of a light screen between the lenses. Previous research efforts have focused on minimizing the gap between lenses to maximize coverage ratio, which is suitable for laser or optical communication applications [47, 48]. However, in our case, we directly placed the micro lens array (MLA) on an image sensor to capture an array of images. Therefore, it was crucial to minimize interference to obtain clearer images. To achieve this, we ensured appropriate distances between the lenses and filled the gaps with the light screen, effectively reducing interference.

This research introduces a cost-effective method for fabricating a micro lens array (MLA) using Cyclic Olefin Copolymer (COC), Polydimethylsiloxane (PDMS), and Carbon Black (CB). CB, obtained by charring various hydrocarbons, finds wide industrial usage, including as a color pigment in inks. It has demonstrated favorable optical limiting properties when combined with epoxy resin [49], which we utilized in this study for the light screen component.

The primary objective of the proposed MLA is to acquire image arrays, prioritizing image clarity over the quantity of images or coverage ratio. We placed the fabricated MLA on an image sensor and conducted an analysis of the point spread function (PSF) to validate the effectiveness of the proposed fabrication technique.

2.2.2 Materials and Method

The manufacturer's recommendation for processing COC involves injection molding. However, in our laboratory setting where accessibility and space efficiency are important factors, compression molding was employed instead. This decision was supported by our previous COC study [46], which had successfully validated the use of compression molding. While it is feasible to create an MLA mold using photoresist through photolithography, the compression molding of COC pellets (5013s-04, TOPAS Advanced Polymers, Germany) necessitates high pressure and temperature. To withstand the compression molding process's pressure, the mold needed to be constructed using a material stronger than silicon wafer and photoresist. For this particular study, we designed the mold using polytetrafluoroethylene (PTFE)-coated aluminum. A prelim-

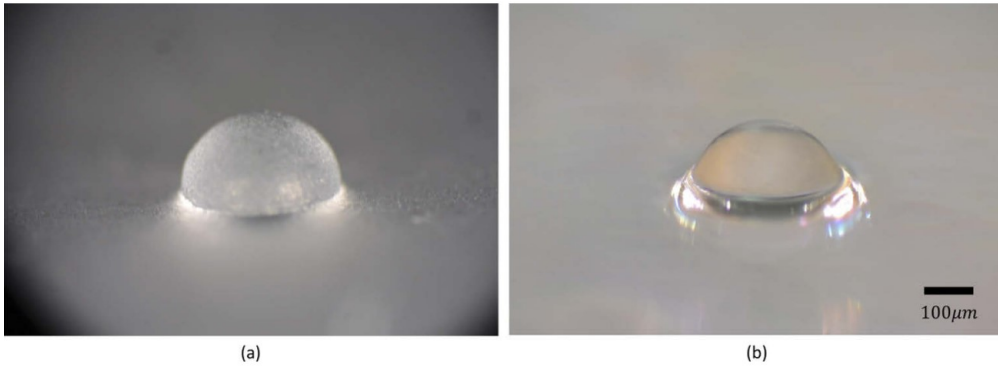


Figure 2.10: Thermal-reflow of a single micro-lens. (a) Before thermal-reflow (b) After thermal-reflow showing smoother surface

inary examination was carried out on a single lens, as depicted in Figure 2.10. The initial outcome after the compression molding process closely resembled the rough surface profile of the mold, as shown in Figure 2.10(a). Subsequently, an investigation was conducted to determine the optimal parameters for a thermal reflow process aimed at enhancing the surface profile. Before creating microlens arrays (MLAs), individual lenses of different sizes were tested to validate the proposed fabrication procedure.

Two test molds were prepared: one in a hemispherical shape and the other in a cylindrical shape, catering to single lenses ranging in diameter from 300 μm to 2 mm. The parameters for reflow process search started at 140 $^{\circ}\text{C}$, which is slightly above the glass transition temperature (T_g) of 134 $^{\circ}\text{C}$, and was incremented by 10 $^{\circ}\text{C}$ until the optimal reflow temperature was identified, as illustrated in Figure 2.10(b).

To mitigate the spherical aberration observed in the single lens with a radius of 150 μm , the radius (R) for each lens in the microlens array (MLA) was adjusted to 250 μm . The effective focal length was then calculated using the lens maker's formula.

$$\frac{1}{f} = (n - 1) \cdot \left(\frac{1}{R_1} - \frac{1}{R_2} \right) \quad (2.2)$$

In the case of a plano-convex lens design, the lens has one flat surface with an infinite curvature radius. Therefore, the lens maker's formula can be simplified as follows, where f represents the focal length, n denotes the refractive index, and R is the radius of curvature of the convex surface:

$$\frac{1}{f} = (n - 1) \cdot \left(\frac{1}{R_1} \right) \quad (2.3)$$

For the remaining curved surface of the lens, let's denote the radius of curvature as R . By inputting the refractive index of 1.533 for 5013s-04 [50] and the R value of 250 μm , the calculated effective focal length (f_L) was approximately 469 μm . To facilitate the detachment of the microlens array from the mold after compression molding, an offset (O_L) was introduced to the lens array. This offset has an impact on the angle of view (α) and the number of lenses per unit area without overlapping images. Assuming the presence of a 50 μm thick light screen, the theoretical angle of view (α) for a single lens can be calculated using the following equation.

$$\alpha = 2\theta = 2\arccos\left(\frac{O_L + T_S}{R}\right) \quad (2.4)$$

, where the thickness of the light screen is denoted as T_S . Additionally, the center-to-center distance between the lenses, known as the pitch (P), necessary to prevent

overlapping images, is dependent on the offset (O_L). The calculation for the pitch is as follows.

$$P = 2(T_F - O_L) \cdot \tan\theta, \quad T_F = (f_L - R/2) + O_L \quad (2.5)$$

The equation for the pitch (P) is influenced by the thickness of the flange-back (T_F).

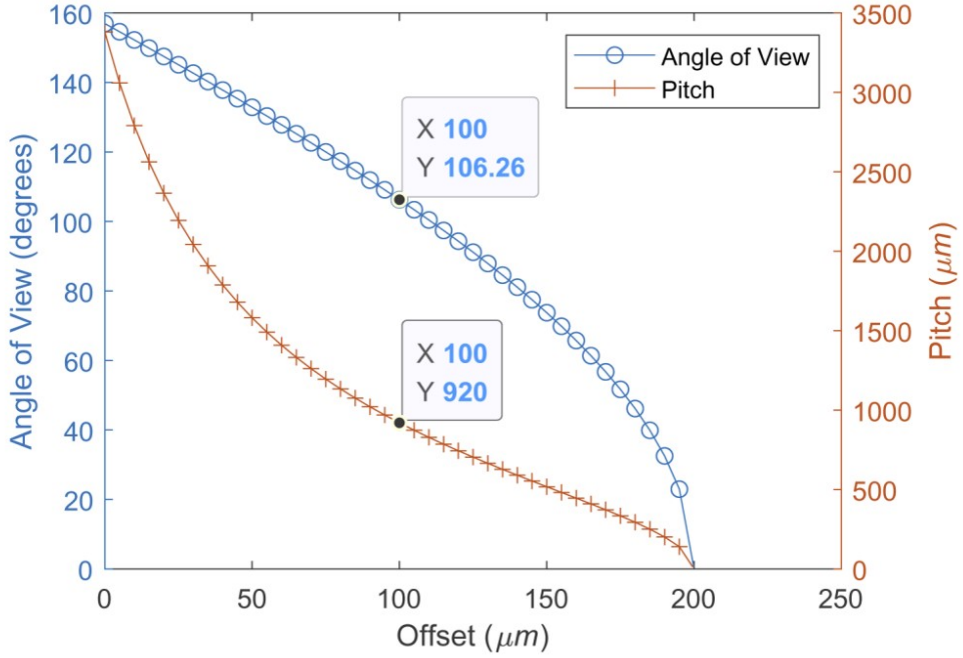


Figure 2.11: Angle of view and the pitch based on offset of the lens.

Equation 2.5 is graphically represented in Figure 2.11. To maintain a balance between the rapidly increasing pitch (P) on the far-left side of the plot and the rapidly decreasing angle of view (α) on the far-right side of the plot, a favorable compromise was identified at $O_L = 100 \mu\text{m}$. With this configuration, the theoretical angle of view was determined to be 106.26° , and the pitch was measured at $920 \mu\text{m}$. The exposed lens above the light screen had a theoretical aperture diameter of $400 \mu\text{m}$. An overview of the design scheme is provided in Figure 2.12.

The light screen functions as an aperture, serving to minimize interference be-

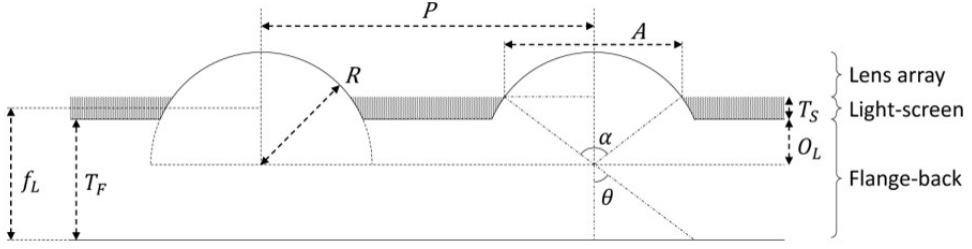


Figure 2.12: Schematic of the COC-CB MLA.

tween images produced by individual lenses and prevent undesired light from entering the image sensor through the flat valleys of the microlens array (MLA). Once the COC-MLA fabrication was accomplished successfully, a technique for installing the light screen became necessary. Previous study had demonstrated the effectiveness of a gold screening layer incorporated into an epoxy-resin-based MLA, validating the positive impact of the light screen on image clarity [33]. However, it should be noted that epoxy resin is a thermoset polymer, whereas COC is a thermoplastic polymer. To accommodate the contrasting fabrication processes of epoxy resin-based MLAs and COC-based MLAs, a novel technique for installing the light screen was developed. In this particular study, a blend of PDMS (Sylgard184, Corning, USA) and CB (CARB-BLK, Graphene Supermarket, NY, USA) was utilized. The weight ratio of PDMS base A, PDMS base B, and CB was set at 10:1:0.2. To ensure a uniform distribution of the PDMS-CB mixture over the MLA area while avoiding its application onto the lenses, the MLA was secured onto a glass substrate using a 50 μm thick Kapton tape. The Kapton tape acted as a spacer to regulate the thickness of the light screen (T_S). To prevent the light screen from detaching after installation, a perfluoroalkoxy alkane (PFA) film (PFA0050, Alphaflon, South Korea) was placed on the surface of the PDMS-CB mixture. Additionally, a separate PDMS block with a 10:1 ratio was created. This block was utilized to apply pressure on the PDMS-CB mixture, ensuring its uniform distribution across the MLA area while conforming to the contour of the lenses. The

PDMS block also served to restrict the height of the light screen to the thickness of the spacer. Both the PDMS block and the PFA film were highly transparent, enabling the MLA to be observed through the PDMS-CB mixture when pressure was applied from the top. While maintaining the applied pressure, the PDMS-CB mixture was subjected to curing at 95 °C for a duration of one hour, resulting in the formation of the light screen. Once the curing process was complete, the PDMS block and the PFA film were cautiously removed. Prior to removing the spacer, the light screen was carefully cut along the inner edges of the spacer to separate it from any adjacent residue of PDMS-CB mixture. After confirming the successful isolation of the light screen, the spacer was lifted off with care. The entire fabrication process is illustrated in Figure 2.13. The Point Spread Function (PSF) analysis of the COC-MLA was conducted

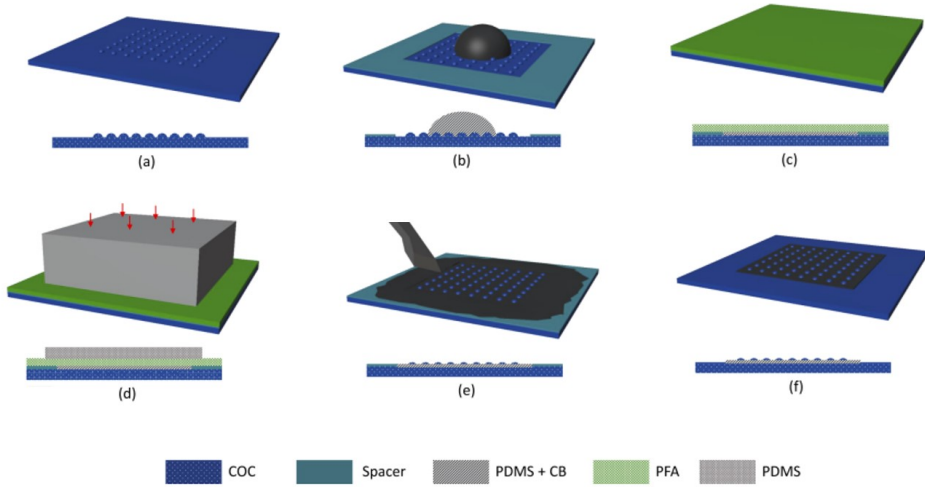


Figure 2.13: Fabrication Process of the COC-CB MLA.

using a customized test setup, as depicted in Figure 2.14. For the experiment, a laser diode (#54-032, Edmund Optics, NJ, USA) with a beam diameter of 3.0 mm was employed. The rationale behind using a wider-beam laser was to capture the response of both the single lens and the lens array. To reduce the beam diameter specifically for the single lens response, a convex lens with a focal length of +200 mm (#33-360,

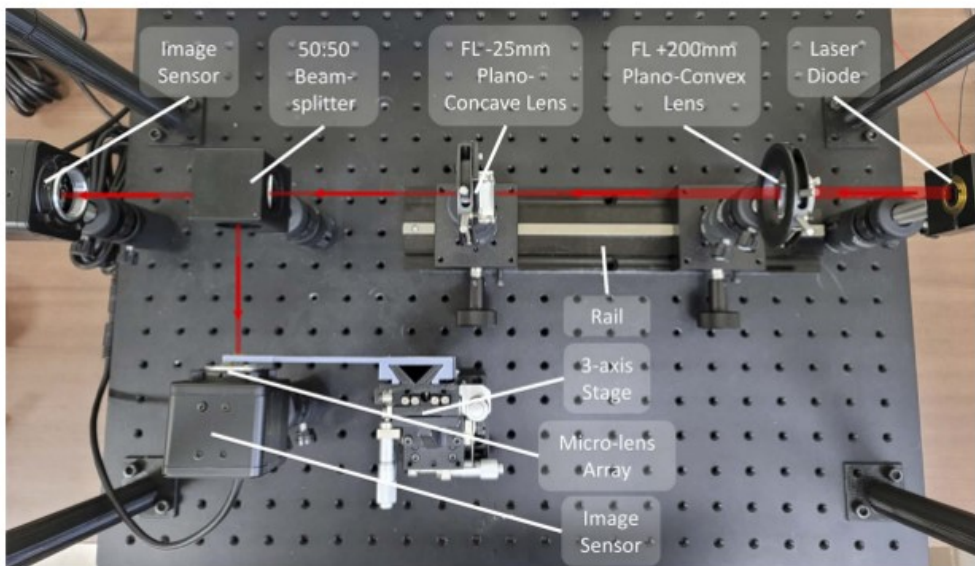


Figure 2.14: Experimental setup for the Point Spread Function of the monochromatic light.

Edmund Optics) and a concave lens with a focal length of -25 mm (#47-911, Edmund Optics) were positioned on a rail track (#56-798, #56-793, Edmund Optics) with a distance of 175 mm between them. The laser beam was evenly split using a beam-splitter (#49-682, Edmund Optics). One portion of the beam was directed straight towards the image sensor (IMX317CQC, Sony, Japan), while the other passed through the microlens array (MLA). The laser power was supplied by a voltage source, and the brightness was adjusted to a level that allowed for optimal observation of intensity using the image sensor, ensuring the greatest dynamic range. To obtain a comprehensive profile of the MLA, the two lenses placed on the rail were removed. This adjustment enabled a wider beam to enter and interact with multiple lenses within the microlens array.

2.2.3 Results and Discussion

The optimal thermal reflow parameter for a single COC micro-lens was determined to be 180 °C for a duration of 10 minutes. This parameter was equally effective for the entire MLA. The microlens array was observed using an optical microscope, and its dimensions were measured using ImageJ software, as depicted in Figure 2.15(a). Assuming that the pitch (P) was unaffected by the thermal reflow process, it was found that the radius (R) increased by approximately 7 μm , while the height of the lens above the flange-back decreased by around 15 μm . Regarding the light screen, it was observed that its thickness exceeded the targeted value. However, it was installed properly, as evidenced by Figure 2.15(b). The measured diameter of the exposed lens, using a G-Scope G6 microscope (GenieTech, South Korea), was approximately 340 μm , which was slightly smaller than the theoretical value.

The COC-MLA was directly placed on an image sensor to observe the USAF1951 pattern at distances of 15 cm and 20 cm, as depicted in Figure 2.15(i) (15 cm) and Figure 2.15(j) (20 cm). Images captured using the COC-MLA without the light screen are shown in Figure 2.15(f) and Figure 2.15(g). Comparing these images, it can be ob-

served that both the hexagonal-arranged MLA and rectangular-arranged MLA produce clearer images when the light screen is installed. Additionally, a noticeable phase-shift is evident in the images, particularly in Figure 2.15(i), which was captured at a closer distance to the object. The angle of view was also assessed using a similar test setup. A 3D printed goniometer was positioned in front of the COC-MLA, as shown in Figure 2.15(e), and the result for a single lens is displayed in Figure 2.15(h). In this figure, nine lines were observed, indicating an angle of view of approximately 80° . By substituting the values of R ($257.60 \mu\text{m}$) and TS ($90.37 \mu\text{m}$) from Figure 2.15(a) into the equation, the calculated α value was found to be 84.7° , which matches with the result presented in Figure 2.15(h). Figure 2.15(k) displays an image captured using a COC-MLA with a light screen installed, featuring a pitch of $500 \mu\text{m}$. Despite the presence of the light screen, the images appear significantly overlapped, as anticipated based on the information provided in Figure 3 and Equation (5).

The PSF acquisition are presented in Figure 2.16. When directly observing the laser beam (Figure 2.16(a), (b), (c), and (d)), a high level of ambient light was detected. However, in the same setup, the presence of the light-screen installed on the COC-MLAs effectively suppressed this ambient light, as shown in Figure 2.16(g) and (h). This demonstrates that the light screen is capable of significantly reducing interference. On the other hand, as in Figures 2.16(e) and (f), where the light screen was not used, the raw laser beam can be observed as a shadow behind the focused light. This would have a negative effect on the clarity of the resulting images, as shown in Figure 2.15(f) and (g). The intensity across the center region (depicted in blue in Figure 2.16(a), (b), (c), and (d), and represented by red lines in Figure 2.16(e), (f), (g), and (h)) is displayed in their respective plots in Figure 2.16(i), (j), (k), and (l). Notably, the lens successfully focused the light, resulting in an amplified intensity, which can be attributed to the thickness of the flange-back (TF). Furthermore, due to the aperture-like effect of the light screen, the presence of spherical aberration was unnoticeable in the images captured with the light screen (Figure 2.16(g) and (h)).

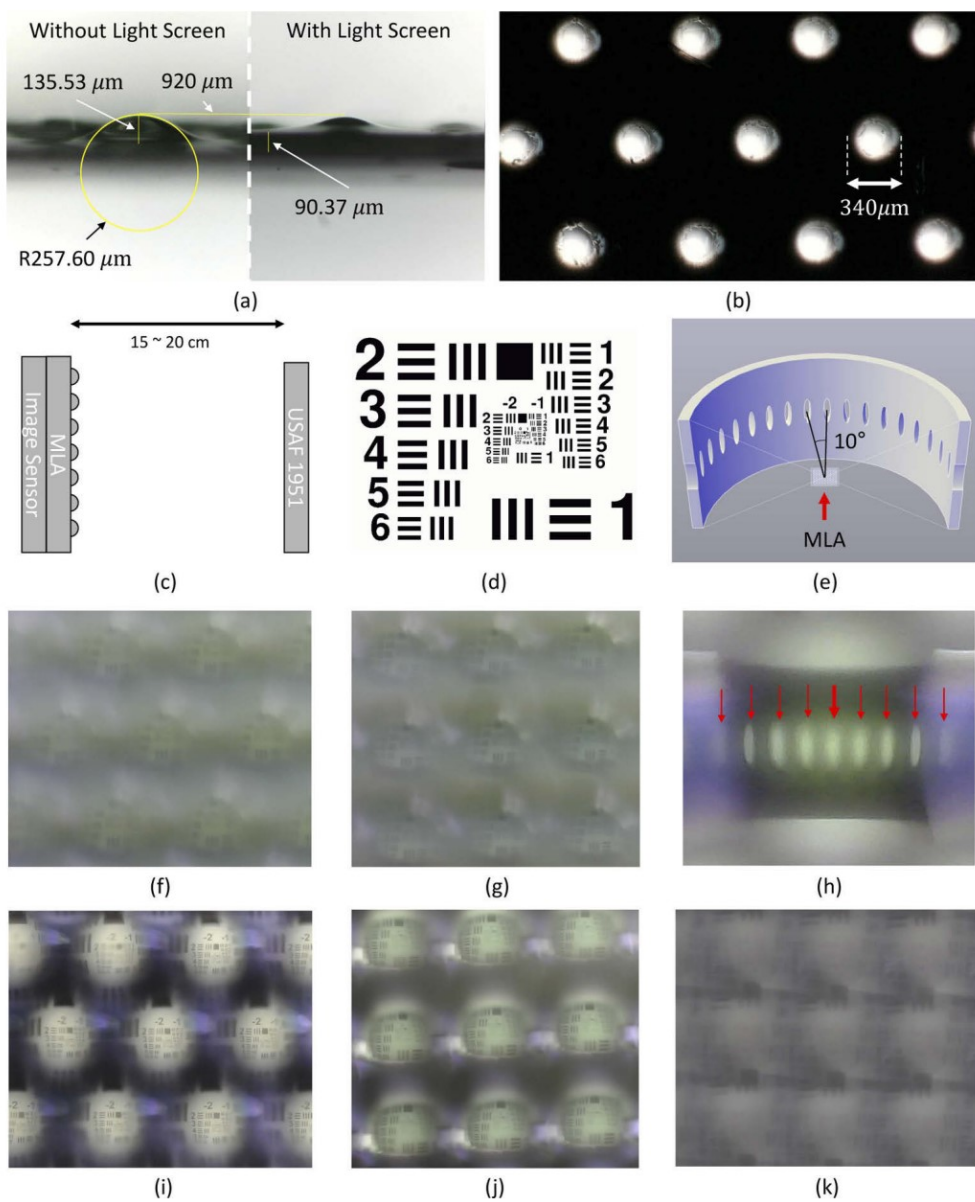


Figure 2.15: Comparisons of the resulting images with and without the light-screen.

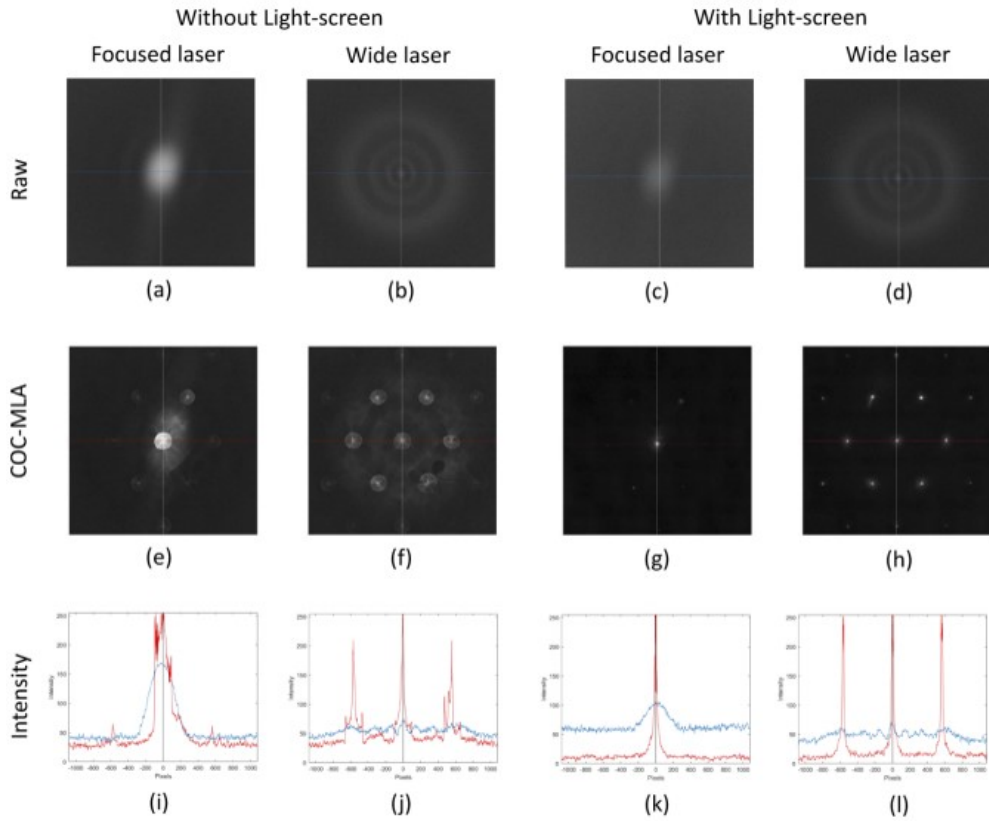


Figure 2.16: CMOS Image Sensor Results of the monochromatic source.

The experimental results depicted in Figure 2.15(i) show distinct separation between individual images, deviating from the expected behavior stated in the theoretical specifications provided in Table 1. Additionally, the observed angle of view in Figure 2.15(h) appears slightly narrower than the anticipated value. These outcomes suggest that the thickness of the flange-back (T_F) may have been larger than initially assumed, causing a shift in the offset (O_L). It is important to note that the T_F can be influenced by various factors, including the applied pressure during the installation process shown in Figure 2.13(d), the mixing ratio of the PDMS (which affects the softness of the PDMS block used), the overall area of the MLA, and the distance between the lenses.

In Figures 2.15(i) and (j), it is evident that some images appear blurry due to multiple reasons. Firstly, the lenses were designed with a theoretical aperture of $400\ \mu\text{m}$, which corresponds to approximately $920\ \mu\text{m}$ of the image sensor per lens, as described in Equation (5). However, in the actual experiment, the aperture size was smaller than the theoretical value. Consequently, each image had a lower resolution compared to commonly used displays, as the image sensor unit cell size was $1.62\ \mu\text{m}$ by $1.62\ \mu\text{m}$, resulting in an approximate resolution of 568×568 pixels per image. Secondly, despite COC having high viscosity at high temperatures [51] and requiring significant pressure for thermoforming, the thermal reflow process introduced certain deviations from the specified lens parameters, particularly affecting the effective focal length. These alterations might have contributed to the observed blurriness in the images.

The deviation in the effective focal length from the target value of $469\ \mu\text{m}$ to the actual value of $483\ \mu\text{m}$ resulted in reasonably acceptable images, as demonstrated in Fig. 2.15(i) and (j). However, to enhance the clarity of the images further, certain corrections could be implemented. It is important to note that polishing of plastics is likely to bring surface distortions due to the heat generated by friction. Additionally, the addition of thin layers may lead to uneven adhesion or heat fatigue, potentially causing distortions. Therefore, further investigation is required to establish a precise

relationship between the shape of the COC-MLA, the thermal reflow parameters, and the compensation required for the change in focal length during the initial compression molding process, taking into account the adjusted thickness.

When it comes to encapsulating electronic devices or creating small systems like bio-mimetic robots, the rigid nature and low water absorption rate of COC can offer advantages. However, the fabrication of micro-precision lenses using COC can be challenging, especially in terms of mold fabrication. CNC machines with micrometer-level precision are still relatively uncommon. Although techniques such as thermal reflow and electroforming have been explored for micro-precision fabrication, limitations arise when applying excessive heat and pressure during COC compression molding, as electroformed molds may not withstand such conditions [52].

An alternative approach involves using soft curable materials like PDMS as high-fidelity stamps [53]. This method has been utilized by researchers to fabricate sub-100 μm diameter COC-MLAs successfully. The use of thermoset polymers like PDMS or photoresist still remains a viable option for fabricating micro-lenses with reduced diameters, considering the increased complexity associated with reducing the diameter of thermoplastic MLAs. Ultimately, the choice of polymer material depends on the specific application requirements and the feasibility of the fabrication process.

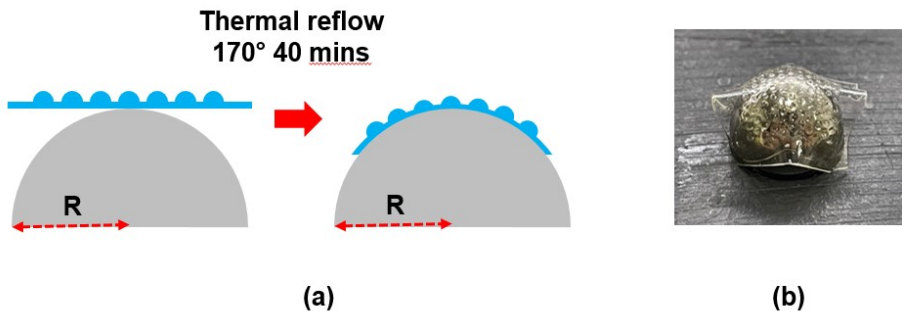


Figure 2.17: Fabrication of the curved COC-CB micro-lens array

To fabricate a curved COC micro-lens array, the most straightforward and conve-

nient approach would be employing a pre-formed mold with the desired curvature. An alternative technique for imparting curvature to the COC-based micro-lens array is to utilize thermal reflow again. Figure 2.10 demonstrates the utilization of the thermal reflow technique to slightly liquefy the uneven surface of COC following the molding process. If this procedure is implemented on a curved surface, such as a small metal ball depicted in Figure 2.17(a), the entire micro-lens array will be smoothed out and acquire the same curvature as the metal ball, as shown in Figure 2.17(b). While the outer portion of the micro-lens array may not exhibit a complete curvature, as long as the central part conforms to the curvature, the lenses will remain in focus. The underlying reason why they would be in focus will be discussed later.

The overall assessment of CB-COC microlens arrays includes the excellent durability of COC and the effective utilization of precision molds for fabrication. However, the inability to adjust the aperture size is a disadvantage. In the fabrication process, CB occupies the space between COC layers, making the thickness of CB the only adjustable variable. This limitation may pose difficulties when utilizing curvature processes, as it may not be possible to apply CB uniformly. To achieve the optimal production of microlens arrays, it would be necessary to introduce a new manufacturing process.

2.2.4 Conclusion

The successful fabrication of the COC-MLA using compression molding and thermal reflow is a significant achievement. By incorporating a light screen made of PDMS and CB between the lenses, interference between neighboring lenses was effectively reduced, resulting in improved image quality. The impact of the light screen was evaluated using an image sensor, highlighting its effectiveness in suppressing unwanted light and enhancing clarity. COC-MLA offers several advantages over other polymer-based MLAs. Its lower water absorption rate and higher rigidity make it suitable for encapsulating electronic devices and being a part of small systems like bio-mimetic

robots. The excellent optical transparency of COC allows it to serve dual functions as both packaging and optics in these systems. This integration of packaging and optics simplifies the overall design and enhances the performance of the system. Overall, the successful fabrication of COC-MLA and its unique properties make it a promising choice for various applications that require precise optical components and reliable encapsulation of electronic devices.

2.3 PDMS-PTFE Micro-lens Array

2.3.1 Introduction

To achieve the ultimate goal of producing a curved microlens array, considering the thermal shrinkage of PVC and the inability to adjust aperture of the CB light screen used in the previous fabrication methods, a new approach was needed. Therefore, in this new method, PDMS was chosen as the lens material, and heat-resistant PTFE was used as the light-blocking material for the microlens array. PDMS was chosen again due to its suitability for processing in liquid form although it has a low resistance to scratches compared to COC. PTFE was prepared with pre-created holes corresponding to the apertures, allowing the liquid PDMS to permeate through the holes. The viscosity of PDMS was then utilized to create the lenses on the opposite side, which is a novel fabrication process.

2.3.2 Materials and Method

Materials include polydimethylsiloxane (PDMS, Sylgard 184, Sigma-Aldrich, United States) with 10:1 of silicone elastomer base to curing agent ratio for the micro-lenses, polytetrafluoroethylene (PTFE, AF008AS, Alphaflon, South Korea) with 80 μm of thickness for the light-screen layer, microscope glass slide (M08-660-147, LK Lab Korea, South Korea) with a 1.1 mm substrate thickness for flatness, and perfluoroalkoxy polymer (PFA, PFA0050, Alphaflon, South Korea) with 50 μm of thickness as a supportive substrate for flexible micro-lens arrays.

The PDMS with a 10:1 ratio of base to curing agent solidifies when it is left at room temperature for 48 hours or 35 minutes when it is heated at 100 °C [54]. However, the behavior of PDMS during the transitional phase between the liquid and solid states remains unclear. Limited studies have focused on this phase, particularly the moment just before the PDMS mixture solidifies when its viscosity is at its highest level. A recent study has demonstrated that PDMS droplets on a heated substrate exhibit an

increased contact angle over curing time due to the viscosity increase of PDMS during its gel time, which follows Equation (1).[55]

$$\mu = 10^{-7}t^2 + 0.0003t + 2.4733, \quad (2.6)$$

The solidification process of the 15ml PDMS in a capped 50ml falcon tube was observed to be completed after 7 hours of natural curing at room temperature in our experiment. Partial gelation of the PDMS was noticed after 6 hours, and at that stage, it was no longer suitable for spin-coating since it behaved more like several chunks of jelly rather than a flowing liquid. Hence, we determined that the last moment for the PDMS mixture to remain in a liquid state with the highest viscosity was around 5 hours of natural curing. According to Equation (1), this corresponds to an approximate 16 times of increase in the viscosity of the PDMS mixture. The elevated viscosity of the PDMS mixture contributes to a delayed flattening of the hemispherical shape, allowing the initially formed lens-like shape to be maintained for a longer duration, primarily due to the surface tension effect. Figure 2.18 illustrates the changes in viscosity of PDMS droplets on two different substrates over time. As the PDMS undergoes natural curing at room temperature, its viscosity gradually increases. The lens-like shape of the PDMS droplets tends to maintain its form for the longest duration when cured for approximately 5 hours. In contrast, freshly mixed PDMS exhibits a state close to complete wetting ('0hr' in Figure 2.18) on both substrates. Before the 5-hour curing mark, the PDMS displays fluidic behavior with no discernible differences between the two substrates. However, on the PTFE film, the PDMS tends to form a dome shape earlier compared to when it is on glass. Nonetheless, when tilted, the PDMS on the PTFE substrate flows easily, indicating relatively low adhesion between the PDMS and PTFE. This behavior is advantageous for lens formation on PTFE film as it prevents the PDMS from flowing over to neighboring PDMS lenses before curing. Beyond the 5-hour curing mark, the PDMS transitions into a highly viscous liquid state that retains its shape effectively. By employing slow curing at room temperature, a higher viscosity is achieved, facilitating the mold-less formation of the micro-lens array. After 6 hours

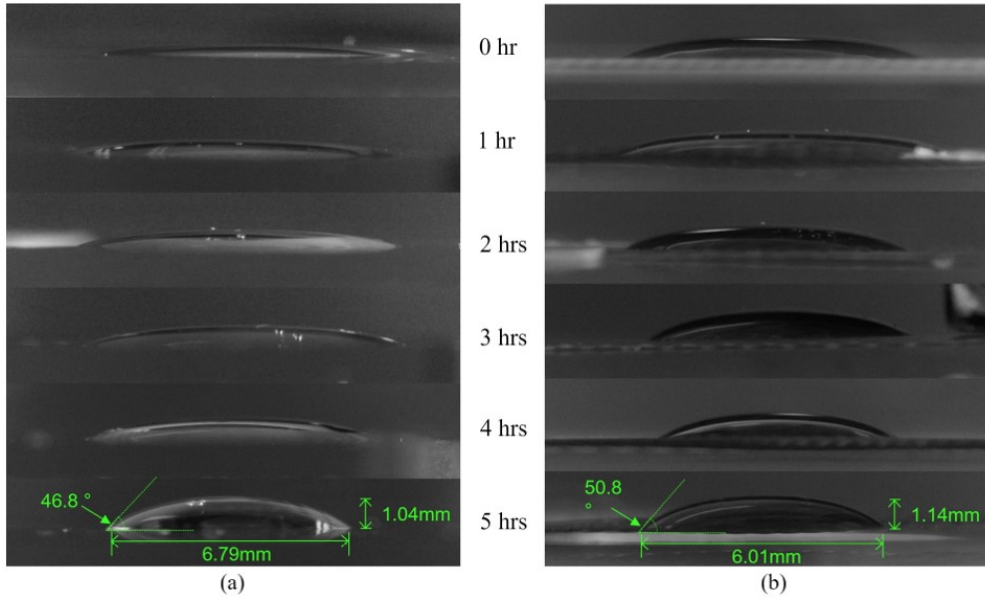


Figure 2.18: PDMS contact angle changes over natural curing time on (a) glass and (b) PTFE.

of curing, the sample transforms into a gel-like solid, losing its fluidic characteristics.

The fabrication steps are as follows: first, the 10:1 ratio of PDMS was spin-coated for 60 seconds at 3000 RPM on a glass substrate, followed by 40 minutes of curing at 100 °C (Fig. 2.19(a) and Fig. 2.19(b)). After curing, PFA film was applied on top of the cured PDMS (Fig. 2.19(c)). Another layer of PDMS, that was cured for 5 hours at room temperature in a capped 50 ml falcon tube, was spin-coated onto a PFA film (Fig. 2.19(d)). Then, a PTFE film with laser-cut patterns was applied on the top of the PFA film (Fig. 2.19(e)). After a few seconds, the PDMS liquid soared upwards through the patterned holes on the PTFE film due to the subtle pressure applied by the weight of the PTFE film (Fig. 2.19(f)). Initially the surface tension of PDMS formed the lens shape, and the shape was maintained due to its viscosity. Lastly, the entire sample was cured on a hot plate for 30 minutes at 100 °C, the substrate was removed and the sample was cut out (Fig. 2.19(g)).

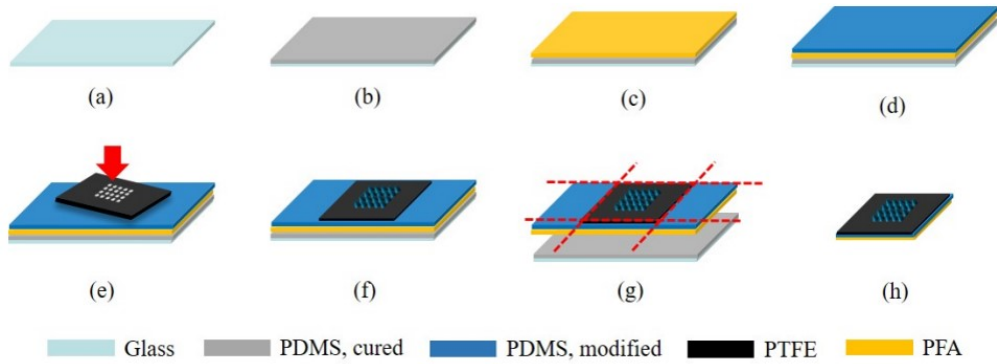


Figure 2.19: Fabrication steps of the PDMS-PTFE micro-lens array. (a) A glass slide as a substrate. (b) Spin-coat a layer of regular PDMS for adhesion. (c) Applying PFA film on top of the PDMS adhesive layer (d) Spin-coat a layer of the viscosity-modified PDMS. (e) Applying the laser-patterned PTFE film. (f) Protrusion of the modified PDMS through the patterned holes. (g) After curing on a hot plate, remove the substrate and cut out the sample. (h) Resulting PDMS-PTFE micro-lens array.

The micro-lens array with PTFE screening layer, as depicted in the right-hand side columns of Figure 2.21, showcases individual lenses with a diameter of $500\ \mu\text{m}$ and a height of $100\ \mu\text{m}$. The lenses are spaced $1.4\ \text{mm}$ apart from each other. The distance between the lenses was optimized through empirical experimentation to avoid overlapping of resulting images. Starting from the inner hole diameter R , the distance between lenses was incrementally increased by R until it reached $20R$. The distance that yielded the best results in terms of achieving the highest packing density was found to be approximately $12R$. The laser-cut inner hole within each lens has a diameter of $120\ \mu\text{m}$. The diameter of the inner hole and the dimensions of the PDMS lens can be customized as small as the fiber laser used allows. With the FM20CS machine from The Lasers (South Korea), the smallest achievable pattern size is $10\ \mu\text{m}$. However, due to laser ablation limitations, the smallest hole diameter possible is around $100\ \mu\text{m}$. For reliable and consistent results in terms of uniformity, the most suitable diameter range on PTFE film is between $100\text{--}200\ \mu\text{m}$, with a PDMS coating thickness of $40\ \mu\text{m}$ on

the substrate. In comparison to lenses made with freshly mixed PDMS (left-hand side column of Figure 2.21), the lenses created from PDMS cured for 5 hours demonstrate better maintenance of their hemispherical shape. Both PTFE film and PFA film possess elasticity and flexibility, as depicted in Figure 2.20(a), allowing the micro-lens array with PTFE light-screen to be easily applied to any curved image sensor.

After the fabrication of the PTFE micro-lens array, it can be applied to various commercially available image sensors. Figure 2.20(b) showcases a specially designed jig used to load the PTFE micro-lens array film onto the image sensor module with adjustable height to achieve the optimal focal length. The micro-lens array is attached to a 3D-printed cover using an ethyl cyanoacrylate adhesive (Scotch Super Glue Liquid AD110, 3M, United States). The cover part and the image sensor part are assembled using screws and spiral springs at each corner. The spiral coil spring surrounding each screw acts as a repelling force to prevent contact between the micro-lens array and the image sensor, while the screws ensure that the cover part remains securely attached to the camera module. This setup enables precise adjustment of the distance between the micro-lens array and the sensor by tightening or loosening the screws. The screws have a body diameter of 2 mm and a total height of 10 mm. Each turn of the screws elevates the cover by 0.2 mm. Once an optimal focus is achieved, test images are captured using a modified USB camera (USB camera module megapixel USB camera, ELP). The original lens in front of the image sensor is removed and replaced with the fabricated PTFE micro-lens array.

2.3.3 Results and Discussion

Demonstration and Spatial information acquisition

The fabricated micro-lens array consisted of plano-convex lenses, each with a measured radius of curvature of $800\text{ }\mu\text{m}$. The lensmaker's equation, as shown in Equation 1.8, was utilized to determine the focal length f of the thin PDMS micro-lens. In the equation, n_1 represents the refractive index of air ($n_1 = 1$), n_2 is the refractive index



Figure 2.20: Fabricated PDMS-PTFE micro-lens array

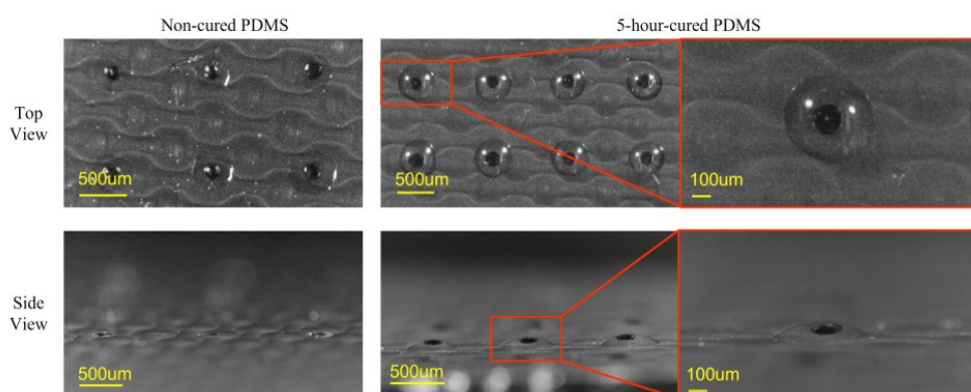


Figure 2.21: PDMS-PTFE micro-lens arrays depending on the condition of the PDMS. (Left column) When PDMS was used right after making. (Right column) The micro-lens arrays are formed when PDMS cured at room temperature for 5 hours was used.

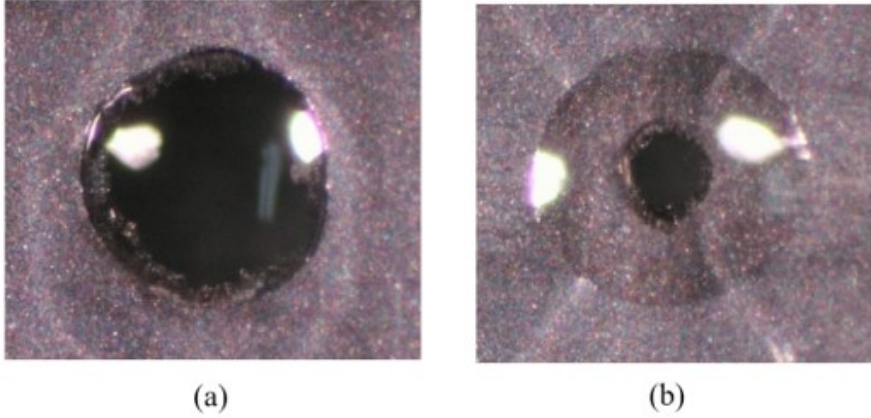


Figure 2.22: Aperture adjustment of the Micro-lens Array. (a) Lens size adjusted by the size of the inner hole with fixed PDMS thickness. (b) Lens size adjusted by the thickness of the PDMS with fixed inner hole diameter.

of PDMS ($n_2 = 1.43$), R_1 denotes the radius of curvature of the micro-lens ($800 \mu\text{m}$), and R_2 is the infinite radius of curvature. By applying these values, the resulting focal length was calculated to be approximately $1860 \mu\text{m}$. This focal length value is valuable not only for determining the optimal distance between the lens system and the sensor plane but also for obtaining straightforward spatial information.

$$\frac{1}{f} = \left(\frac{n_2 - n_1}{n_1} \right) \cdot \left(\frac{1}{R_1} - \frac{1}{R_2} \right). \quad (2.7)$$

In Figure 2.23(d), (e), and (f), actual snapshots taken using the PTFE micro-lens array combined with the image sensor are presented. Clear disparities between the images can be observed in each image. In Figure 2.23(d), a printed version of the USAF-1951 resolution test chart (Figure 2.23(a)) is displayed on each lens. Each individual lens in the micro-array presents a slightly different view of the target image. The left-most lens shows the target image shifted towards the right, while the right-most lens shows a slight bias towards the left from the center. Similar to a binocular

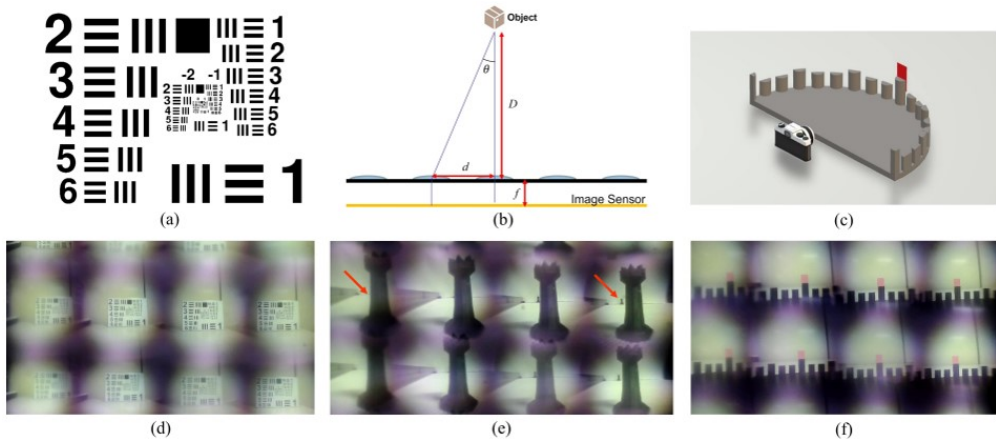


Figure 2.23: Images taken using the fabricated micro-lens array and the image sensor. (a) Original image of USAF 1951 resolution test chart. (b) Disparity calculation schematics. (c) 3D printed goniometer and camera setup. (d) Resulting image taken by the micro-lens array showing the printed test target. (e) Appearance of a pawn behind the rook (right red arrow) and disappearance of the pawn (left red arrow). (f) Field-of-View test images of the micro-lens array. Red mark indicates the center of the goniometer.

vision system, the disparity obtained from the two lenses in the micro-lens array provides spatial information. By analyzing the pixel-wise differences between the two images displayed on the screen, the depth information can be obtained. By utilizing the focal length (f) determined through the Lens Maker's Equation and the distance between two selected lenses in the micro-lens array, the distance between the target object and the micro-lens array can be computed. This calculation can be performed using trigonometry, as shown in Equation 2.8 and Equation 2.9. For instance, the images obtained from each lens in Figure 2.23(e) provide distance information about a pawn positioned far behind a rook. In the figure, the pawn is placed 30 cm behind the rook, which itself is 10 cm away from the micro-lens array sensor. The actual distance between the pawn and the image sensor is measured as 39.8 cm. The calculation involves applying a simple trigonometric relationship based on Equation 2.8 and Equation 2.9, which are also illustrated in Figure 2.23(b).

$$Disparity_{ref} = f \cdot \tan(\theta) = f \cdot d/D_0, \quad (2.8)$$

$$D_1 = f \cdot d/Disparity_{calibrated} \quad (2.9)$$

In Equation 2.8, f represents the focal length of the lens obtained from the lens maker's equation, d is the distance between each micro-lens (center to center), and D_0 is the reference distance between the target object and the sensor, which is used for calibration purposes. Equation 2.9 calculates the distance value D_1 of the target object using the values obtained from Equation 2.8. In this equation, $Disparity_{calibrated}$ refers to the calibrated value of $Disparity_{ref}$, which is the pixel-wise difference measured on the computer screen. With the exception of the disparity value that needs to be obtained from the image, the other information required for the calculations is readily available: the focal length f (1.86 mm) and the distance between each lens d (1.4 mm). The disparity value is first obtained through image processing, based on the number of pixels that appear on the screen, and then calibrated using Equation 2.9 with a reference object at a predefined distance. The measurement in this case was performed using the

two lenses on the right-hand side of the upper row. Using the known distance value of the rook ($d_{rook} = 10$ cm), the reference disparity value ($Disparity_{reference} = 0.79$ mm), and the calibration coefficient of 0.329, the disparity value of the target object, in this case, the pawn, was obtained through image processing ($Disparity_{pawn} = 0.2$). By applying the calibration coefficient in Equation 2.9, the distance value of the pawn ($D_1 = 39.57$ cm) was calculated, which closely matches the measured distance of 39.8 cm. This demonstrates the effectiveness of the method in accurately estimating the distance to objects using the micro-lens array and image sensor setup.

$$D_1 = (1.86mm)(1.4mm)/(0.2mm)(0.329) = 39.57cm. \quad (2.10)$$

Apart from distance measurement, images captured using micro-lens arrays can be used for various applications such as image reconstruction. By merging a subset of images taken from different micro-lenses, it is possible to create a single image with enhanced features like different focus levels, improved resolution, and even motion detection of surrounding objects [33, 56, 57].

The field-of-view (FOV) of the imaging system was assessed using a 3D printed half-circle goniometer (Fig. 2.23(c) and 2.23(f)). The black bars on the goniometer represent a 10 °angle, starting from the bar with a red mark at the center. The micro-lenses in the third column, indicated by the red mark at the center, exhibited an 80 °FOV, with four spaces on each side of the center bar. The lens in the second column displayed five gaps on the left side of the red mark, while the lens in the fourth column had four gaps on the right side. This suggests that a single lens provides an approximate 80 °FOV, but in a micro-lens array system where multiple lenses are horizontally aligned, the FOV can be expanded to 100 °. Considering the flexibility of the fabricated micro-lens array, the FOV can exceed 180 °when paired with a perfectly hemispherical image sensor.

Micro-lens formation and Aperture

The micro-lens array was designed with flexible materials for future application on a curved CMOS image sensor. Two options were considered for the light screen-aperture integrated layer: black PTFE film and black polyvinyl chloride (PVC) film, both known for their flexibility. However, the PVC film proved unsuitable as it couldn't withstand the heating process required for PDMS at 100 °C, resulting in heat distortion and reduced yield rate. Consequently, the black PTFE film, with its higher melting point of 329.1 °C, was chosen for its temperature resistance [58].

Regarding the micro-lens array, laser-assisted fused silica is commonly used. However, the protrusion method, which requires the lens material to extend through the light screen layer, cannot be applied to rigid materials. Therefore, PDMS and photopolymers were considered for the fabrication process. The photopolymer, unfortunately, could not be fully cured when positioned beneath the PTFE film due to the UV-stable nature of PTFE [59]. As a result, PDMS was adopted due to its flexibility, transparency, ease of use, and low cost [60].

Traditionally, PDMS micro-lens arrays are fabricated using the stamping method or mold injection method, where PDMS is cured within a mold to maintain its shape easily. This is possible because PDMS has low viscosity, allowing it to quickly spread and flatten. However, for the novel fabrication method that doesn't involve mold manipulation for lens shape formation, a more viscous PDMS is required to sustain its hemispherical shape for an extended period, facilitating the formation of micro-lenses.

The size of each micro-lens was determined by the weight of the PTFE film and the thickness of the PDMS layer underneath. The pressure exerted on the PDMS layer resulted from the subtle weight of the PTFE film, which caused the liquid PDMS to flow out through the laser-cut holes. The thickness of the 5-hour cured PDMS layer beneath the PTFE film played a role in regulating the amount of PDMS that could seep out.

For instance, a 1 cm by 1 cm PTFE film weighed approximately 12.5 ± 1 g, which

applied a pressure of around 1.23 ± 1 Pa on the PDMS layer. The pressure exerted by the PTFE film, combined with the high viscosity of the PDMS, caused the liquid PDMS to bulge through the laser-cut holes. The PDMS molecules surrounding the holes remained relatively stationary, while the PTFE film on top pushed the liquid PDMS downward, creating a small bulge through the holes. The surface tension and viscosity of the PDMS contributed to the formation of a lens shape with longer-lasting stability.

Once a certain size of the lens was formed, the PDMS no longer oozed out through the holes. This was because the weight of the PDMS lens that had already passed through the holes exerted pressure that counteracted the further protrusion of PDMS. This equilibrium prevented additional PDMS from flowing out. The ratio between the diameter of the inner hole and the diameter of the lens was approximately 1:4. With a 1.2 cm by 1.2 cm PTFE film and an inner hole diameter of 120 ± 10 μm , a lens diameter of 480 ± 10 μm was achieved. The slight fluctuation in size was attributed to the inner woven mesh layer of the PTFE film.

The thickness of the PDMS also played a role in determining the size of the lens. In this study, the optimal thickness for the fabricated lens was found to be 40 μm . To achieve the desired thickness, the spin-coater (ACE-200, Dong Ah Trade Corp, South Korea) was used to precisely control the PDMS thickness. After curing the PDMS at room temperature for 5 hours, spin-coating was performed for 10 seconds at 1000 RPM, followed by 50 seconds at 3000 RPM. The high viscosity of the PDMS resulted in a thicker coating compared to regular PDMS spinning, with a thickness of 40 ± 2 μm . In contrast, untreated PDMS measured a thickness of 20 μm when measured with a digital caliper (Mitutoyo Vernier Calipers, Mitutoyo Corp., Japan).

The 40 μm thickness was sufficient to fill the inner space of the array of 5x5 patterned holes on an 80 μm thick PTFE film. The excess PDMS that gently protruded through the holes due to the weight of the film formed the lenses. When the PDMS thickness precisely filled the cylindrical shape inside the inner hole (as shown in Fig.

2.22(a)), the size of the lens matched the diameter of the inner hole. In this case, the thickness of the PDMS was also 40 μm , as the widened inner diameter required a larger amount of PDMS to fill the space.

The micro-lenses were formed by protruding the PDMS through the small inner hole (Fig. 2.22(b)), rather than adjusting the size of the inner hole to match the desired lens size (Fig. 2.22(a)). This design took advantage of the PTFE light screening layer, which also served as an aperture. By protruding the PDMS through the small hole, the lenses were formed in a spherical shape, as opposed to an aspherical shape. Spherical lenses inherently do not exhibit spherical aberration at the lens edge. Therefore, incorporating the PTFE light screening layer not only reduced excessive incoming light intensity but also minimized aberrations at the lens edge, effectively acting as a small aperture (Fig. 2.22(d)).

Table 2.1 provides a comparison of fabrication methods and performance indices for micro-lens arrays mimicking insects' compound eyes. The protrusion method, used in this study, offers several advantages over other commonly employed techniques. It features a simpler fabrication process specifically optimized for the light screen-aperture integrated design, resulting in lower costs. While photolithography, compression molding, injection molding, and 3D printing offer high precision, they are not suitable for fabricating the desired design with the chosen materials due to technical constraints.

Furthermore, the proposed method eliminates the need for complex machinery or dedicated molds for lens formation, contributing to its cost-effectiveness. However, there are limitations associated with the protrusion method. One limitation is the material restriction for lens fabrication, as rigid materials like fused silica cannot be used in this process due to their inability to flow through the holes in the light screen layer. Additionally, the stability of the protrusion method is relatively lower compared to other fabrication techniques, as it relies on the viscosity of the material. In terms of performance, the micro-lens array developed in this study exhibited the longest visual

range, comparable to the Thiele's foveated micro-lens array. Additionally, with the same visual range, our micro-lens array achieved a wider field of view (FOV) of 100° , primarily due to the presence of a small aperture.

The flexibility of our fabricated micro-lens array enables its application on a curved CMOS sensor. Previous work by Song demonstrated a wide FOV of 160° using a hemispherical micro-lens array-photodetector-integrated structure, mimicking insects' compound eyes. However, the FOV achievable with a micro-lens array can vary based on its design. Keum and Zhang also applied micro-lens arrays on a hemispherical surface, but their FOV was limited to 68° and 86° , respectively, due to the recessed positions of their micro-lens arrays. In contrast, our micro-lens array design does not have a recessed design and can be curved into various shapes, including a hemispherical configuration, allowing us to achieve a wider field of view when coupled with a curved CMOS image sensor.

Fabrication		Performance				
	Method	FOV (°)	Tested distance ^a (mm)	Light Screen	Curved ^b	Focal length (mm)
This work	Protrusion	100	1000	O	O	1.8
Baek ^[12]	Compression molding	85	200	O	X	0.48
Seo ^[11]	Photolithography	100	100	O	O	1.4
Keum ^[8]	Photolithography	68	N/A ^c	O	O	1.4
Thiele ^[13]	3D printing	20-70 ^d	1000	X	X	65-252 ^d
Zhang ^[5]	Injection molding	87	320	O	O	5.8
Song ^[6]	Photolithography	160	32	X	O	N/A ^c

^a The distance between the target object and the micro-lens array as demonstrated in the paper.

^b Availability of the curved design mentioned in the paper.

^c Not specified by the author

^d Different sizes of micro-lens arrays were tested.

Table 2.1: Fabrication method and performance comparisons of various micro-lens arrays.

2.3.4 Conclusion

The protrusion fabrication method created the light screen-aperture integrated, flexible micro-lens array. Compared to traditional micro-lens arrays, the screen-aperture integrated design offers a superior visual range of one meter and maintains a wide field-of-view of 100 °. This design and the artificial compound eye's longer visual range and multi-perspective capability allowed for obtaining distance data from the resulting images. The flexible micro-lens array was also suggested for curved CMOS image sensors to achieve a wider field of view.

These improvements highlight the micro-lens array's potential to overcome existing arrays' limitations, making them suitable for future computer vision systems. Due to its longer visible range and the ability to acquire spatial data, our micro-lens array can be applied to computer vision systems for small robots and endoscopy applications that require accurate distance measurement in a compact size.

Chapter 3

Micro-Lens Array design in depth

3.1 Effect of the aperture

3.1.1 Depth-of-Field

The aperture has several effects on the resulting image, such as controlling the depth of field (DOF) and influencing the amount of light that reaches the image sensor. A wide aperture creates a shallow depth of field, which offers limited sharpness for objects located at a certain distance, while a narrow aperture creates a deep depth of field, providing more of the scene in focus. As mentioned, a light-screen aperture is crucial since it can block rays of light scattered from neighboring lenses. The effect of aperture size is depicted in Figure 3.1. As the aperture size decreases, the system can capture clear images of objects at greater distances. However, this comes at the cost of reduced brightness due to the decrease in incoming light. The micro-lens arrays previously introduced have a light-screen aperture that fills the gaps between all the lenses, which provides an aperture stop around them. Having an aperture on a micro-lens array is the reason for the long visual distance, which is related to the depth of field. Depth of field refers to the range of distance where the subject appears sharp and in focus and is determined by the lens's aperture and focal length. A wide aperture will produce a shallow depth of field, while a narrow aperture will produce a deeper depth of field. As

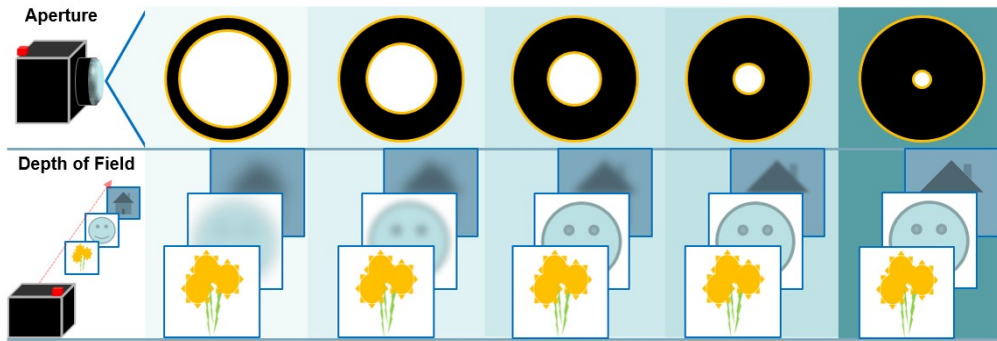


Figure 3.1: Changes of Depth-of-Field and brightness due to aperture size

the aperture gets smaller and smaller, the depth of field increases, allowing the vision system to capture an object located further and further by widening the depth of field. The increase in depth of field indicates an extended range of visibility for the lens. This occurs because a smaller aperture restricts the passage of marginal rays, leading to a longer focal length, as illustrated in Figure 3.2. Among the depicted cases, the one on the far left, with an aperture radius equal to 0.2 times the lens size, exhibits the greatest focal length when compared to instances where the aperture has ratios of 0.5 and 1.0 relative to the lens size. Figure 3.3 shows the Modulation Transfer Function (MTF) for each aperture size ratio. The result demonstrates that having a smaller aperture provides better optical performance.

Another influence on the resulting image of the aperture is the brightness. Figure 3.4 shows the total power change depending on the aperture size and location while other parameters are fixed. Using a simulation tool Zemax (Zemax OpticsStudio, Ansys, USA), single plano-convex micro-lens with a similar diameter ($500\text{ }\mu\text{m}$) and that of the micro-lens arrays were created and tested. Concerning the "ratio" of the aperture, a ratio of 1 indicates that the aperture has the same radius as a single micro-lens. On the other hand, a location ratio of 1 implies that the aperture is positioned at the back of the lens, while a ratio of 0 indicates that it is located at the frontmost part. As the aperture ratio decreases, the total power decreases, and the impact of the aper-

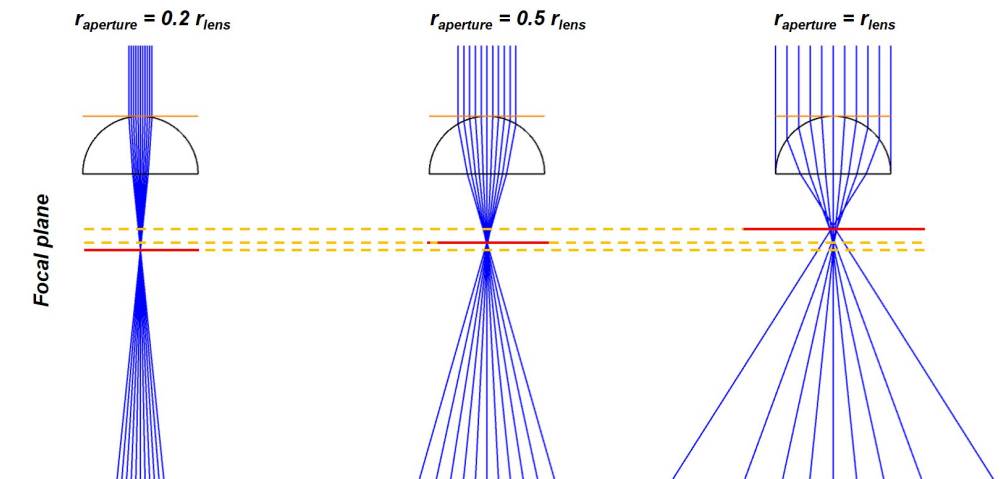


Figure 3.2: Change of focal length due to aperture

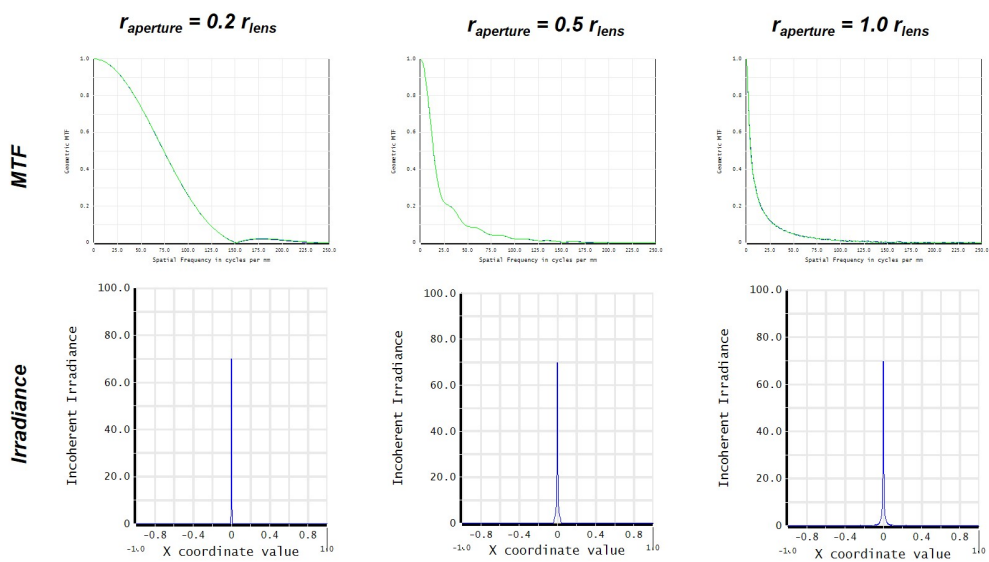


Figure 3.3: Change of focal length due to aperture

ture's location is negligible. The decrease in total power signifies a reduction in the brightness of the resulting image. Therefore, reducing the size of the aperture leads to a dimming effect on the image.

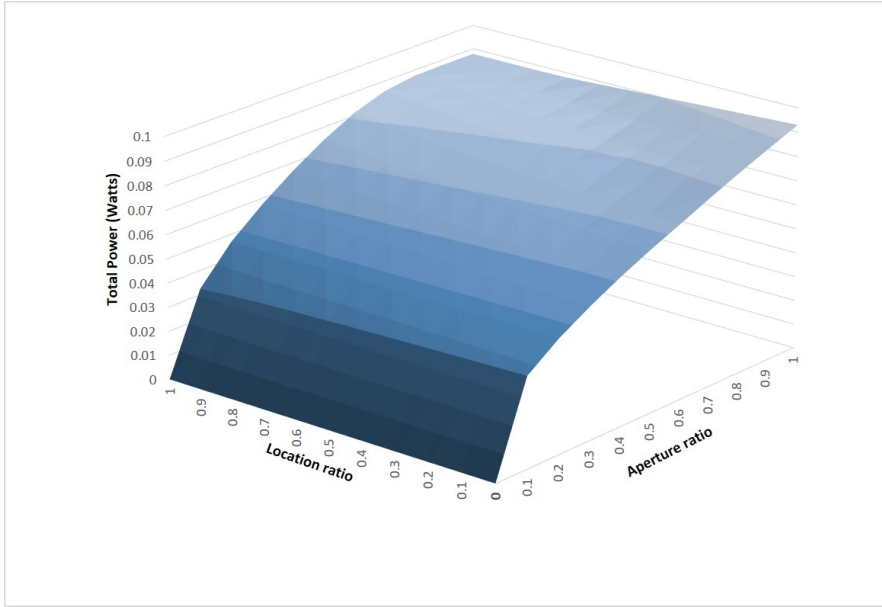


Figure 3.4: Total power changes by aperture ratio and location

Using the size of the aperture, f-number 'N' can be obtained as in equation 3.1.

$$N = \frac{f}{D} \quad (3.1)$$

, where f is the lens's focal length, and D is the diameter of the aperture. Table 3.1 shows the f-numbers of three different micro-lens arrays previously fabricated.

	PDMS-PVC	COC-CB	PDMS-PTFE
focal length (mm)	0.08	0.48	1.8
Aperture size (mm)	0.1	0.4	0.12
f-number	0.8	1.2	15

Table 3.1: f-number of the fabricated micro-lens arrays

With the f-number and the specifications of the micro-lens arrays, a modulation transfer function (MTF) can be obtained, which explains how the PDMS-PTFE micro-lens array can observe better than the previously manufactured ones.

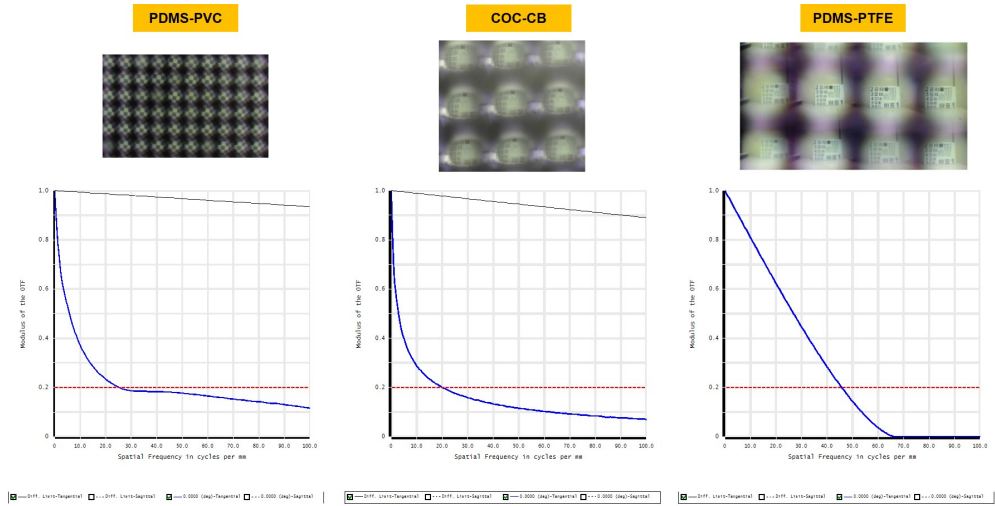


Figure 3.5: Modulation Transfer Functions of the fabricated Micro-lens arrays.

3.1.2 Field-of-View

The field-of-view is the angle of the scene that is captured by the vision system, and it is determined by the focal length of the lens, as described in Equation 3.2

$$\alpha = 2 \cdot \arctan\left(\frac{D}{2f}\right) \quad (3.2)$$

, where α is the field-of-view in degrees, D is the sensor size (or the image size that laid on the sensor), and f being focal length. A shorter focal length will result in a wider field-of-view, while a longer focal length will narrow the field-of-view.

Is was discussed that having a smaller aperture increases focal length of the system, and according to the Equation 3.2, it decreases the field-of-view of the system. However, unlike conventional single lens cameras that only have α °of field-of-view at its best, micro-lens arrays innately have slightly larger total field-of-view owing to the neighboring lenses that are located around the central lens, as in Figure 3.6. This multi-ocular system also provides wider FOV as in human eye's binocular vision.

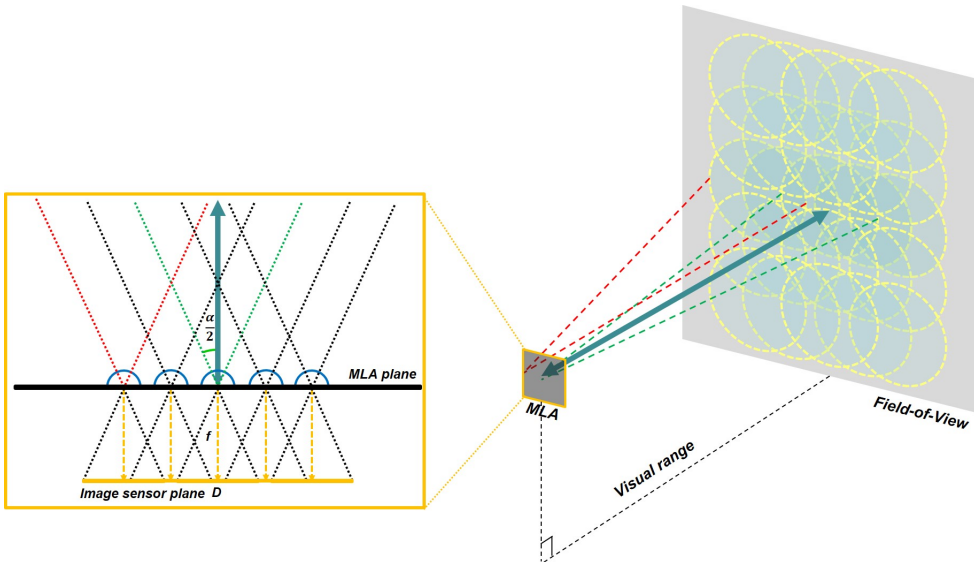


Figure 3.6: Field-of-View of a flat Micro-lens Array

If the micro-lens arrays are expected to observe objects located infinitely far away,

the total field-of-view would be just α regardless of the number of lenses for the system. However, according to Table 2.1, micro-lens arrays observe objects a meter ahead at its most, meaning the distance is finite. In this case, as shown in Figure 3.6, although a single lens at the center provides only FOV of α , the total FOV owing to the additional layers of lenses would provide even wider FOV. As discussed earlier, having a binocular vision provides depth information due to overlapping field-of-view from each eye. In case of the micro-lens array system, these overlap occurs on almost every view, since each lens shares similar scenery with the neighboring micro-lenses. Therefore, if we make it a curved version, we can have even wider FOV, not to mention that it is a part of biomimetics in terms of its structure.

In order to mimic pigment cells, certain studies have developed lenses that incorporate an adjustable aperture, allowing for versatile focusing capabilities, instead of using a fixed aperture value. However, the variability of the focal length implies that the distance between the lens and the image sensor must be flexible. If the distance between the lens and the image sensor is fixed, any changes in aperture would be meaningless. Furthermore, the majority of such studies utilize electroactive polymers (EAP), which require voltages ranging from a few hundred to several thousand. This makes them unsuitable for use in small robots.

3.2 Micro-Lens Array Arrangements

3.2.1 Arrangements on a flat surface

Conventional micro-lens arrays with either rectangular or hexagonal arrangements show the difference in their packing density which refers to the number of lenses per area. The packing density, or a “fill factor” is determined by the gap between the lenses, lens diameter, and pitch of the lenses[61].

The author defined the fill factor $\eta = \frac{\pi(\phi/2)^2}{p_x p_y}$, where ϕ is the diameter of a single microlens, p_x and p_y are the distance or the pitch between the neighboring lenses.

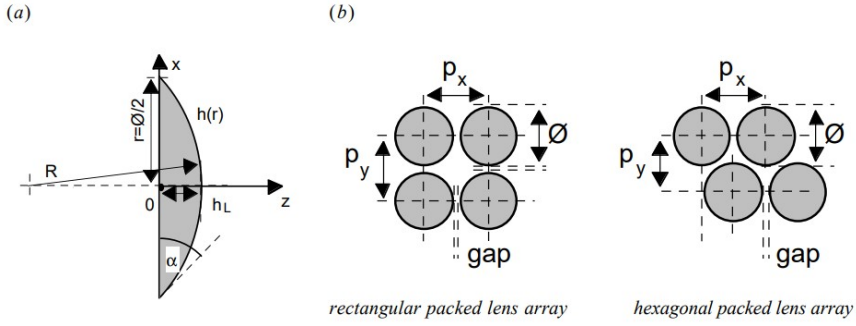


Figure 3.7: (a) Single plano-convex micro-lens to be arranged (b) Rectangular (left) and hexagonal (right) arrangements. p_x and p_y representing the pitch (center-to-center).^[61]

Starting from $\phi = p_x$, where there is no gap between the lenses, the rectangular shape (78.5 %) has a lower packing density than that of hexagonal shape (90.5%) [61]. As the gaps between the lenses increase, the fill factor decreased. With the PTFE light-screen, the hexagonal arrangement has more efficiency in terms of the number of images. However, as shown in Fig. 3.8, the hexagonal arrangement lacks the ability to manage noise around the edge of the resulting image because the gap between each lens cannot be completely blocked by the light-screen. As the gray value comparison suggests from Fig. 3.8(b) and (d), the peak value did not show a noticeable difference between the two arrangements. In other researches that proceeded reconstruction of the images captured by the micro-lens arrays, the benefits of adopting hexagonal arrangement over the rectangular arrangement were addressed. Since the hexagonal arrangement's spatial frequency is 1.15 times higher than that of the rectangular, it was able to obtain more precise 3D reconstructed images [62], and in another research that compared reconstruction of images through the interference imaging system, hexagonally arranged micro-lens arrays showed superior results over other arrangements of arrays they conventionally used[63]. Therefore, adopting the hexagonal arrangement over the rectangular arrangement is promising considering the fact that the images

obtained from the compound eye system would be processed for further use.

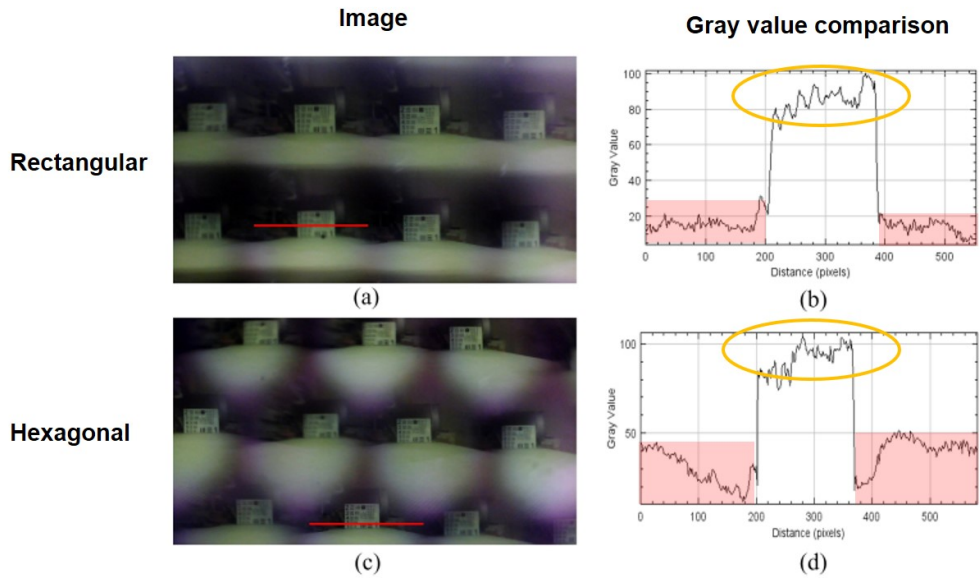


Figure 3.8: Gray value comparison between the rectangular arrangement and the hexagonal arrangement with a USAF-1951 test target located at one meter away. (a) Rectangular arrangement with red line segment indicating the region of analysis. (b) Gray value analysis result of the red line in Fig. 3.8(a). (c) Hexagonal arrangement with red line segment indicating the region of analysis. (d) Gray value analysis result of the red line in Fig. 3.8(c).

3.2.2 Arrangements on a curved surface

Ultimately when the fabricated flexible micro-lens array is attached on a curved surface instead of the flat, the Cartesian coordinate system is arduous in obtaining spatial information from the resulting image since the arrangement lies on a curvature that requires extensive computation. The spherical coordinate system, or the polar coordinate system, is more suitable for processing spatial information in this condition where the distance measurement needs to be done in a 3-dimensional space [64]. The simplicity of the hexagonal arrangement in terms of the spherical coordinate computation in a 3-dimensional space is shown in Fig. 3.9. With regard to the flat surface (upper row), both rectangular and hexagonal arrangements have three levels of layers including the reference micro-lens in the blue area. When these micro-lens arrays were laid on a curved surface as shown in the lower row of the Fig. 3.9, the number of orbits increased dramatically in the case of the rectangular arrangement compared to the hexagonal arrangement for the same level of the layer. For the two micro-lens array arrangements with n layers of lenses, the number of total orbits are as shown in Table 3.2.

n	1	2	3	4	5	6	7	8	9	10
O_{rect}	1	3	6	10	15	21	28	36	45	55
O_{hex}	1	2	4	6	9	12	16	20	25	30

Table 3.2: Numerical comparison of the the number orbits for the arrangements.

The number of total orbits follows the equations below:

$$O_{rect} = n(n + 1)/2, \quad (3.3)$$

$$O_{hex} = \lfloor n/2 \rfloor (\lfloor n/2 \rfloor + 1) + \lfloor (n + 1)/2 \rfloor |\sin((\pi/2)n)|, \quad (3.4)$$

where O_{rect} and O_{hex} are the total number of orbits for the rectangular and the hexagonal arrangements respectively, and n is the level of the layer. The rectangular arrangement has about twice as many distinct orbits than the hexagonal arrangement.

The increased number of orbits indicates the increase in complexity of the calculation for spatial data processing. Therefore, the hexagonal arrangement is more beneficial than the rectangular arrangement in terms of both packing density and computational power budget, even though it lacks the ability to deal with the noise around the edge.

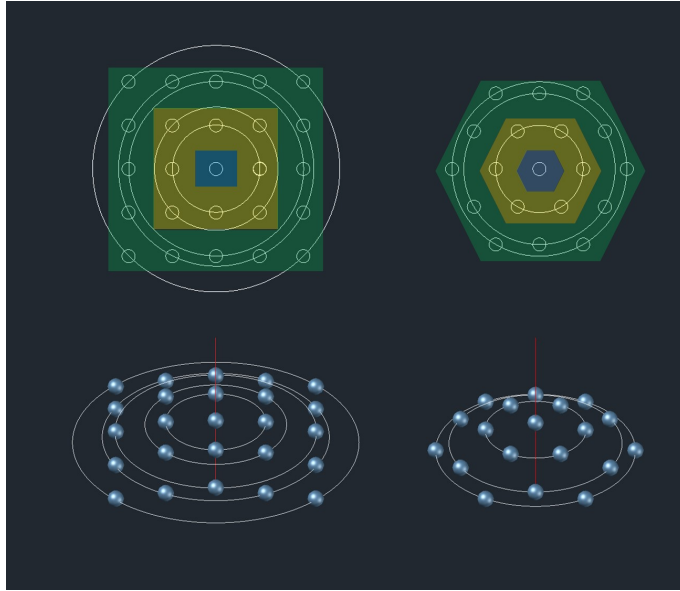


Figure 3.9: Comparison of the rectangular and the hexagonal arrangement on a curved surface. The colored area in the upper row indicates the level of layers from the reference micro-lens (blue area). The red vertical line and the white orbital circle indicate the reference micro-lens, and groups of outer micro-lenses that share the same polar angle from the red line, respectively.

Radius adjustment

The problems with the curved arrangement of the micro-lens array, however, are 1) the lenses are no longer in a perfect focus and 2) the airy disk that is laid on the image surface will no longer be a circular shape. Instead, it will have elliptical shape. Imagine a micro-lens array on a curved surface with its curvature R as described in Figure 3.10.

Assume the micro-lens ‘A’ at the center of the curved surface with its focal length f_0 is perfectly focused on the image sensor plane with its height being f_0 from the sensor. The other micro-lens, for an example, a micro-lens ‘B’ that is tilted with a zenith angle ϕ_1 to the normal of the image plane, namely $\overline{C_1O}$. Since the lens ‘B’ is tilted, it will be positioned lower than that of lens ‘A’, so the focal length will no longer in focus. The size of the lens ‘B’ must be shrunk to a certain ratio so that it can have a valid focal length.

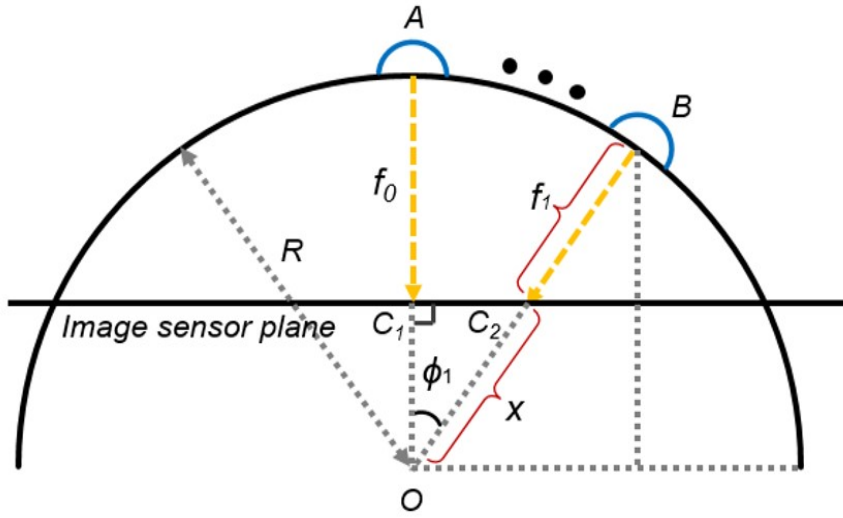


Figure 3.10: Schematic of Micro-lens Array on a curved surface: focal length

$\overline{CS'}$ To find the value of a new focal length, namely ‘ f_1 ’,

we can make use of the given terms. Since $\overline{OC_1} = R - f_0$, the length of $\overline{OC_2}$ can be written as $\overline{OC_2} = x = \frac{R-f_0}{\cos\phi_1}$, from $\triangle C_1C_2O$. Since $R = f_1 + x$, $f_1 = R - x = R - \frac{R-f_0}{\cos\phi_1}$. Therefore, a micro-lens that is located tilted by any angle can be expressed as:

$$f_1 = R - \frac{R - f_0}{\cos\phi_1} \quad (3.5)$$

The newly obtained focal length can be used to find a new radius for the lens from the *lensmaker's equation* that was derived in Equation 1.8. Since we're assuming a

plano-convex lens with its surrounding being air, it can be re-written as:

$$\frac{1}{f_n} = (n' - 1) \cdot \left(\frac{1}{r_n}\right) \quad (3.6)$$

in terms of r_n , it is:

$$r_n = (n' - 1) \cdot f_n \quad (3.7)$$

plugging the newly obtained relationship from Equation 3.5 into the Equation 3.7, now we can obtain a proper radius for a micro-lens located anywhere on the curved surface, in terms of the curvature R , zenith angle ϕ_n , refractive index of the material n' , and the focal length f of the initial micro-lens located at the center.

$$r_n = (n' - 1) \cdot \left(R - \frac{R - f_0}{\cos \phi_n}\right) \quad (3.8)$$

Shape adjustment

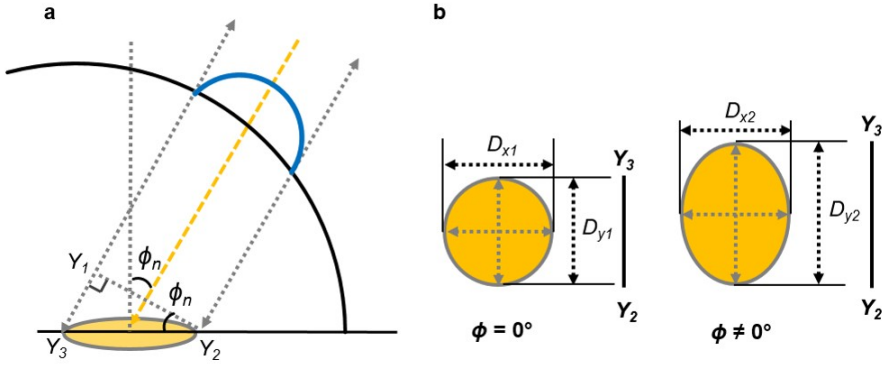


Figure 3.11: Schematic of a Micro-lens on a curved surface that has elliptical airy disk.

The shrunk micro-lens will be in focus when it is located on the curved surface with the tilted angle, or zenith angle ($\phi \neq 0^\circ$). However, because it is tilted, the airy disk that was supposed to be a circle now becomes an elliptical shape. In Figure 3.11, a micro-lens on a curved surface with its zenith angle ϕ_n is illustrated. If it were at the center

of the curvature (where $\phi = 0^\circ$), the airy disk would be similar with the one in the left of Figure 3.11(b). However, geometrical change forces the circular airy disk to be an elliptical. From $\triangle Y_1Y_2Y_3$, $\angle Y_1Y_2Y_3 = \phi_n$ due to AAA similarity postulate. Again from $\triangle Y_1Y_2Y_3$, $\overline{Y_1Y_2}$ becomes $\overline{Y_2Y_3} \cos\phi_n$, because projection of $\overline{Y_2Y_3}$ is $\overline{Y_1Y_2}$. As illustrated in the right-hand-side of Figure 3.11(b) where $\phi \neq 0$, the elliptical airy disk now has its major axis D_{y2} which satisfies the relationship $D_{y2} = D_{y1}/\cos\phi$. This indicates that for a micro-lens that is located at an arbitrary surface with the tilted angle ϕ , its radius along the center of the curve must be multiplied by $\cos\phi$ to compensate the extended radius of the airy disk. Assuming that each micro-lens has its own local xy-coordinate system where its y-axis heading toward the center micro-lens:

$$r_{y2} = r_0 \cdot \cos\phi_n \quad (3.9)$$

Since the radius on the x-axis must stay the same, and combined with the Equation 3.8, radii of the micro-lens that is now an ellipse, has its semi-major and semi-minor axes:

$$\begin{aligned} r_{xn} &= (n' - 1) \left(R - \frac{R - f_0}{\cos\phi_n} \right) \\ r_{yn} &= (n' - 1) (R \cdot (\cos\phi_n - 1) - f_0) \end{aligned} \quad (3.10)$$

To verify calculations, Zemax OpticsStudio was used again. The design scheme is as following: Under Non-sequential System (NSC) settings, BK7 plano-convex lenses with $250\text{ }\mu\text{m}$ of radius are hexagonally arranged, on a curved surface with 10 mm of curvature. A curved ‘Absorb’ layer was located along the lens’ curvature to simulate the lightscreen-aperture of the micro-lens arrays, and either cylindrical or elliptical pillar was used to create apertures on the ‘absorb’ layer using the native boolean function. The lenses on the second layer has 7.5° of zenith angle from the z-axis which is the parallel to the axial ray of the light source. 2 mm by 2 mm sized detector plane is located exactly at the focal length of the center lens. As discussed earlier, due to the shortened distance between the detector plane (image sensor) and the lens, while the center lens’ peak irradiance shows clearly, two small and broad irradiance peaks are shown on the left and right side, which are the irradiances from the lenses on the second layer (Figure 3.12). By applying the results acquired from Equations 3.6 and 3.8,

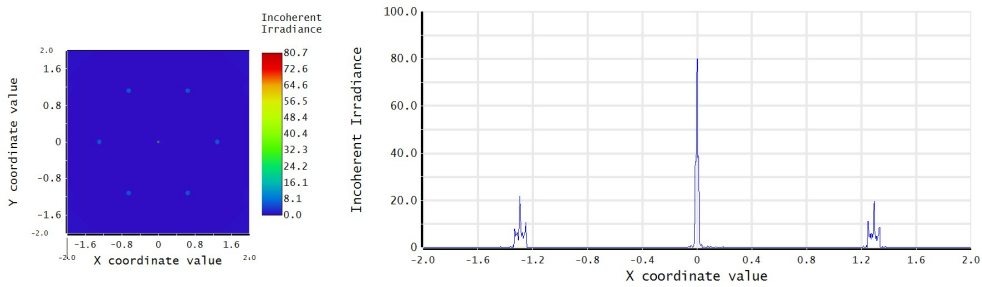


Figure 3.12: Zemax simulation result for a micro-lens array on a curved surface whose lenses have the same radius regardless of the zenith angle.

the focal length of the lens at the center was found, and the radius of the second layer could be adjusted using that value. Note that the material BK7 has 1.515 of refractive

index (n'). From Equation 3.6,

$$\begin{aligned}
 \frac{1}{f_n} &= (n' - 1) \cdot \left(\frac{1}{r_n}\right) \\
 \frac{1}{f_n} &= (1.515 - 1) \cdot \left(\frac{1}{0.25 \text{ mm}}\right), \\
 &= \frac{1}{f_n} = 2.06 \text{ mm}^{-1} \\
 &\rightarrow f_n = 0.4854 \text{ mm}
 \end{aligned} \tag{3.11}$$

plugging the center focal length value (f_0), curvature of the surface $R=10$ mm, and the zenith angle $\phi = 7.5^\circ$ to Equation 3.8, we have a new radius for the lenses on the second layer:

$$\begin{aligned}
 r_n &= (n' - 1) \cdot \left(R - \frac{R - f_0}{\cos \phi_n}\right), \\
 r_n &= (1.51 - 1) \cdot \left(10 - \frac{10 - 0.4854}{\cos 7.5^\circ}\right) \\
 r_n &= 0.208 \text{ mm}
 \end{aligned} \tag{3.12}$$

Applying the optimal radius to the simulation, the result shows improved irradiance as shown in Figure 3.13.

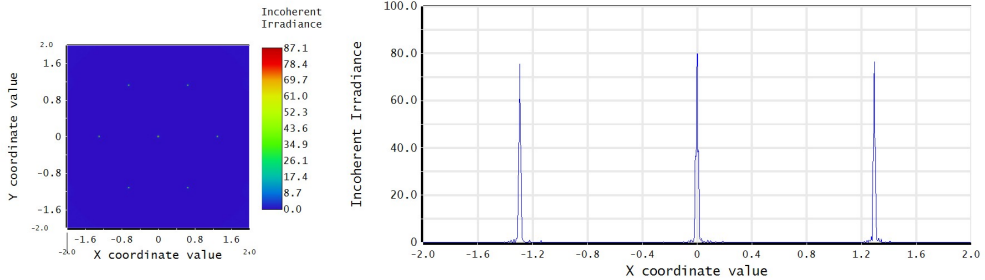


Figure 3.13: Zemax simulation result for a micro-lens array on a curved surface whose lenses have different radii depending on the zenith angle.

Next, to validate compensation of the extended airy disk explained with the Figure 3.11, the plano-convex lens on the second layer are transformed into half-cut ellipsoids. Figure 3.14 illustrates the result of the shrunk micro-lenses that have not been adjusted from Figure 3.12. Compared to the left and right peaks from Figure 3.12, it is proven

that a slight change of the lens shape improved the performance, peak irradiance value on both side increased from $20 \pm 1 \text{ Watts/cm}^2$ to $30 \pm 2 \text{ Watts/cm}^2$. However, when both radius and shape were adjusted at the same time, the result was similar with the case when the radius was adjusted, which can be said that the effect of shape is negligible as long as the size of a micro-lens is well-designed at the corresponding position on the curve.

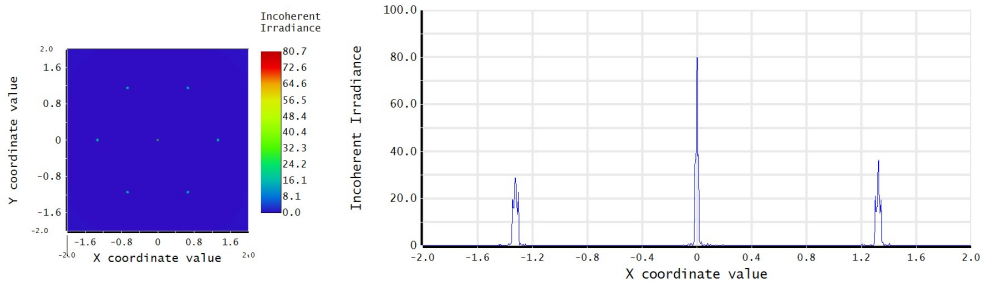


Figure 3.14: Zemax simulation result for a micro-lens array on a curved surface whose lenses have elliptical shape depending on the zenith angle, while maintaining the same initial radius regardless of the zenith angle.

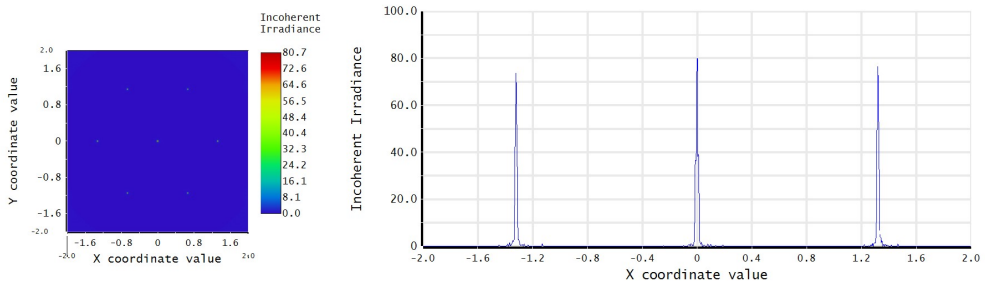


Figure 3.15: Zemax simulation result for a micro-lens array on a curved surface whose lenses have elliptical shapes depending on the zenith angle while varying the radii depending on the zenith angle.

Maximum and minimum number of lenses

Maximum Number of layers

Considering that the optimal size of the micro-lens on a curved surface varies depending on the zenith angle, it would be precisely calculated how many micro-lenses can exist. One can Assume a number of micro-lenses on a curved surface with its curvature being R , varying focal length and its radius expressed as f_n and r_n , respectively, as shown in Figure 3.16. The distance between the two arbitrary lenses is an arc, namely $L(\phi_n)-L(\phi_{n+1})$, as illustrated in Figure 3.16. As long as $L(\phi_n)-L(\phi_{n+1})$ is greater than sum of the radius of two adjacent micro-lenses, the micro-lenses would not overlap, while keep their distances as short as possible. The relationship can be expressed as described in Equation 3.13.

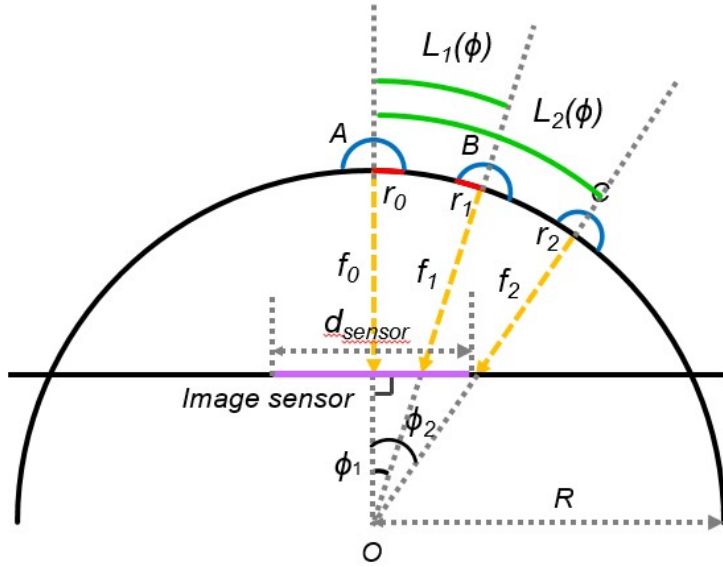


Figure 3.16: Schematic of Micro-lens Array on a curved surface: for maximum number of lenses.

The distance between two adjacent micro-lenses located at zenith angles ϕ_n and

ϕ_{n+1} is:

$$L(\phi_{n+1}) - L(\phi_n) = R \cdot \phi_{n+1} - R \cdot \phi_n \quad (3.13)$$

Since this should be larger than the sum of the radii the micro-lenses obtained in Equation 3.8,

$$R \cdot \phi_{n+1} - R \cdot \phi_n = (n' - 1) \cdot (R - \frac{R - f_0}{\cos \phi_n}) + (n' - 1) \cdot (R - \frac{R - f_0}{\cos \phi_{n+1}}) \quad (3.14)$$

Moving the terms related to $n + 1$ to the left-hand-side and n to the right-hand-side, we get:

$$R\phi_{n+1} + (n' - 1) \cdot (R - f_0) \left(\frac{1}{\cos \phi_{n+1}} \right) = R\phi_n + 2(n - 1)R - (n' - 1)(R - f_0) \left(\frac{1}{\cos \phi_n} \right) \quad (3.15)$$

From the small-angle approximation which makes $\cos \phi_n = \frac{2 - \phi_n^2}{2}$, the general equation that describes the relationship between n th micro-lens and $n + 1$ th lens can be expressed as:

$$R\phi_{n+1} + (n' - 1) \cdot (R - f_0) \left(\frac{2}{2 - \phi_{n+1}^2} \right) = R\phi_n + 2(n' - 1)R - (n' - 1)(R - f_0) \left(\frac{2}{2 - \phi_n^2} \right) \quad (3.16)$$

Before we finalize the number of lenses that satisfies the conditions, however, we need to find the maximum zenith angle that can illuminate the image within the image sensor, namely ϕ_{lim} , since beyond that certain angle, image would not fit in the sensor. As shown in Figure 3.16, the size of the image sensor would not be large enough to cover the light coming from a micro-lens located at a certain zenith angle, namely, ϕ_{lim} . ϕ_{lim} can be obtained by a simple trigonometry. From $(R - f_0)\tan(\phi_{lim} < d_{sensor}/2)$, we have:

$$\phi_{lim} < \arctan\left(\frac{d_{sensor}/2}{R - f_0}\right) \quad (3.17)$$

In the previous setting where $R=10$ cm, $r_0 = 0.25$ cm, $\phi_0 = 0^\circ$, and assuming that the camera has 2 mm of image sensor, $\phi_{lim} \approx 0.1047172rad = 5.999853^\circ \approx 6^\circ$. Starting with the initial zenith angle $\phi = 0^\circ$ and other given parameters such as R , f_0 , and ϕ_{lim} , right-hand-side of the equation becomes a constant value. Based on that,

ϕ_{lim}	0.1047						
ϕ_n	0	0.0494	0.0965	0.1394	0.1768	0.2082	...
ϕ_{n+1}	0.0494	0.0965	0.1394	0.1768	0.2082	0.2336	...

Table 3.3: Zenith angles in radian where the micro-lenses can be located at its maximum for given parameters.

we can solve the left-hand-side polynomial equation for ϕ . By narrowing down the range of the solution that satisfies $0 \leq \phi \leq \phi_{lim}$, we can find the number of lenses the following angles can be obtained as shown in Table 3.3. Since $\phi_{lim} = 0.1047rad$ limits the largest possible zenith angle to be 0.0965 rad, we can have until 3rd layer of the arrangement. The results are demonstrated in Figure 3.17.

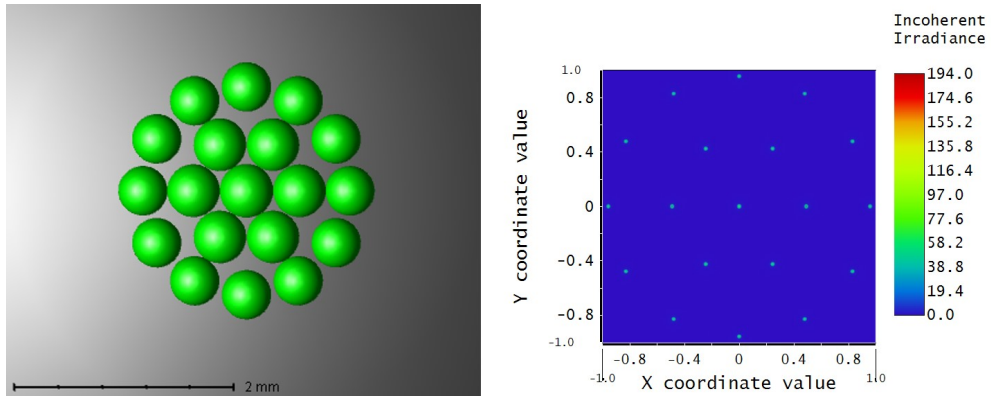


Figure 3.17: Resulting maximum number of lenses simulated on Zemax.

Minimum number of layers for 180 °Fied-of-View

As demonstrated earlier, in the case of a flat-type micro-lens array, the maximum field-of-view is slightly larger than that of a single lens, approximately 100 °. This

happens because the lenses arranged side by side provides additional scenery as if the object is being observed from slightly behind from where the camera is actually located as shown in Figure 3.18. However, if the lenses are arranged on a curved surface as de-

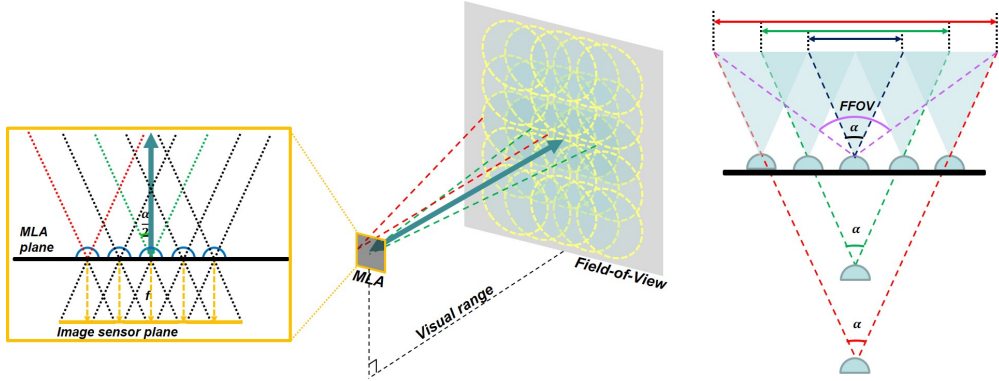


Figure 3.18: Reason for the flat type Micro-lens array providing wider field-of-view compared to the single lens.

picted in Figure 3.19, the overall field of view of the system can be further expanded. For instance, when ignoring the size of image sensor, the FOV can be anywhere between $n \cdot \phi + \alpha$ degrees, where ϕ is the zenith angle of the lense located at the outer most layer, n is the number of layers, and α is the field-of-view of a single lens. Since we're assuming a conventional CMOS image sensor that has a flat with finite size, ϕ_{lim} must be taken into account for a realistic maximum FOV it can possibly obtain. In that case, the maximum FOV would be $2 \cdot \phi_{lim} + \alpha$. As in Figure 3.20(a), consider a micro-lens array with a single lens providing α of field-of-view that is neighboring with another micro-lens array located at the zenith angle ϕ . If the angles α and ϕ are the same, the system would have an blind zone that the camera would never capture. However, as in Figure 3.20(b), as long as α is greater than ϕ , the angles will eventually touch, providing a continuous scenery when combined. Considering the visual range of the camera system, if the height of the blind zone, where the angle touch, exceeds the visual range, still it would not provide a continuous scenery. To achieve a continuous scenery, therefore, the height of the blind zone h must be smaller than the visual

range V , which must satisfy $V > h$, where h follows the relationship

$$h = \frac{R\phi}{2} \cdot \tan\left(\frac{\pi}{2} - \frac{\alpha}{2}\right) \quad (3.18)$$

,where R is the curvature of the curved surface, ϕ is the zenith angle, and α represents the field-of-view of a single lens.

To cover 180° of field-of-view, $n\phi + \frac{\alpha}{2} > 90^\circ$ is required for the lens located at the n^{th} layer with α of field-of-view. This means that the n must be larger than $\frac{\pi-\alpha}{2\phi}$, as shown in Equation 3.19.

$$n > \frac{\pi - \alpha}{2\phi} \quad (3.19)$$

From Equation 3.18, Equation 3.20 can be derived that describes minimal angle ϕ_{end} that the entire system requires to cover 180° .

$$\phi_{end} = \frac{2V}{R} \cdot \tan\left(\frac{\alpha}{2}\right) \quad (3.20)$$

Combined with the condition Equation 3.19 for covering 180° , it becomes:

$$n_{end} > \frac{\pi - \alpha}{2} \frac{R}{2V} \cot \frac{\alpha}{2} \quad (3.21)$$

To conclude, the minimal number of layers required to cover 180° was found with variables such as curvature of the surface R , visual range V , and field-of-view of a lens α .

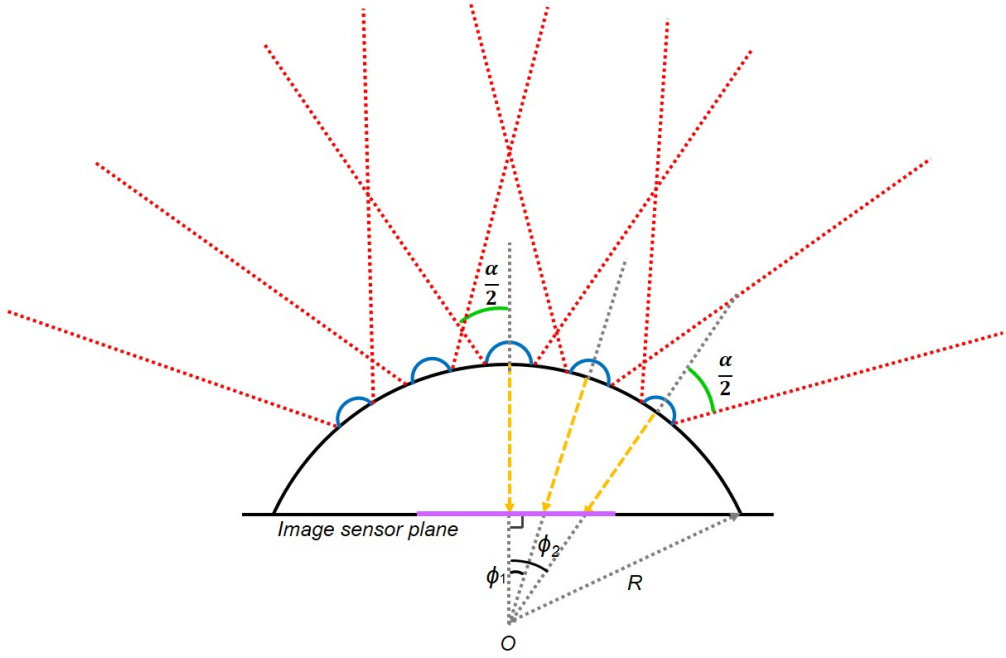


Figure 3.19: Schematic of the Field-of-View of the micro-lens array on a curved surface.

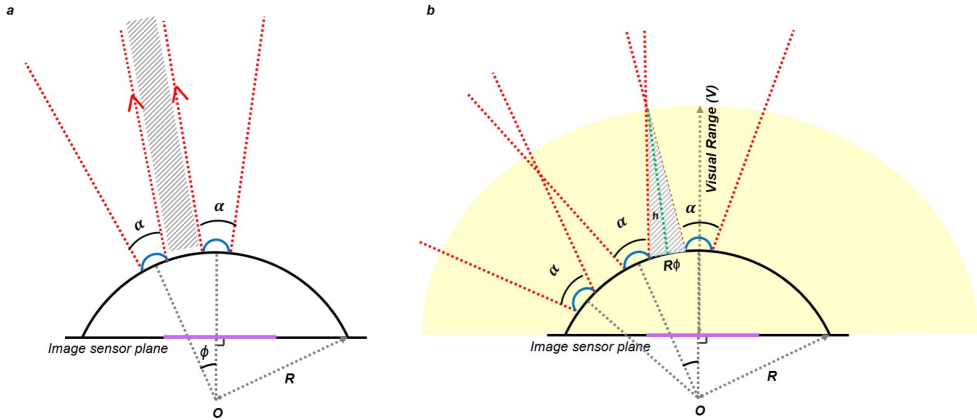


Figure 3.20: Schematic of the minimum number of layers required to achieve 180° Field-of-View for a micro-lens array on a curved surface.

Curvature of the surface

As discussed earlier, micro-lens arrays aligned on a curved surface would achieve $2 \cdot \phi_{lim} + \alpha$ of maximum field-of-view. Since the term ϕ_{lim} is determined by the size of the image sensor d_{sensor} , curvature R , and focal length of the reference lens f_0 , as those variables change, the maximum field-of-view would also be altered. Considering the specifications of the reference lens and the size of the image sensor are given, in other words, when the curvature R is the only variable that affects ϕ_{lim} , one can set the reasonable range of the value R . Combined with 3.17, the maximum field-of-view $2 \cdot \phi_{lim} + \alpha$ can be re-written as:

$$FOV_{max} = 2 \cdot \arctan\left(\frac{d_{sensor}/2}{R - f_0}\right) + \alpha \quad (3.22)$$

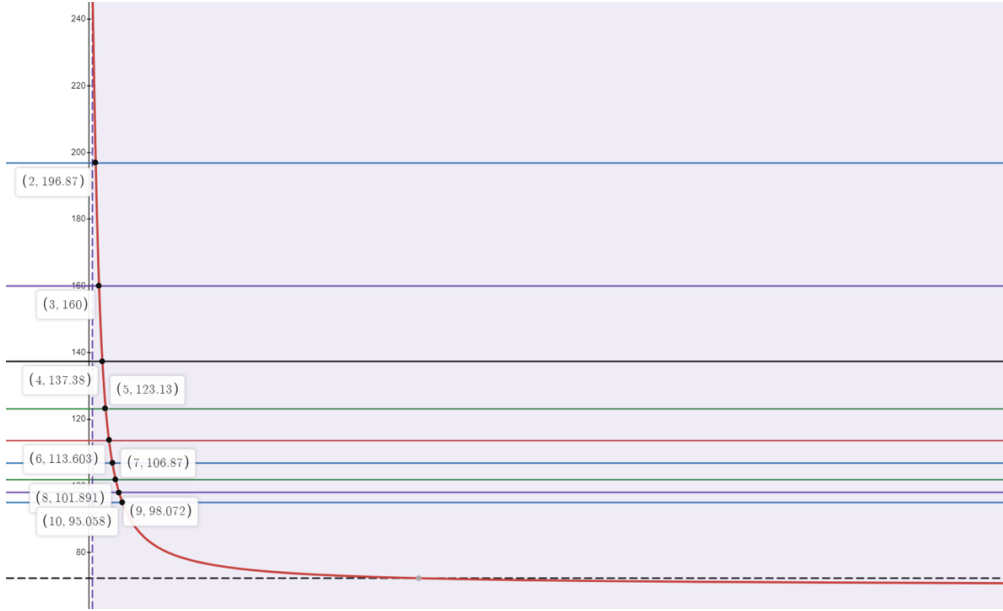


Figure 3.21: Change of the maximum field-of-view by curvature R while d_{sensor} , f_0 , and α are constant.

The minimum value of R must be larger than the focal length f , since if R is less than or equal to f , the images formed on the sensor would be positioned wrong or

even overlap. It would be reasonable to set the range of possible values of R to be $f < R$. As Figure 3.21 illustrates, the maximum field-of-view would converge to α as R increases and increases as R approaches f . With $R = 16$, it reaches around 100° of field-of-view, and reaches 200° when R is as low as 2.865, for $\alpha = 70$ and $d_{\text{sensor}} = 4$ mm of previous settings.

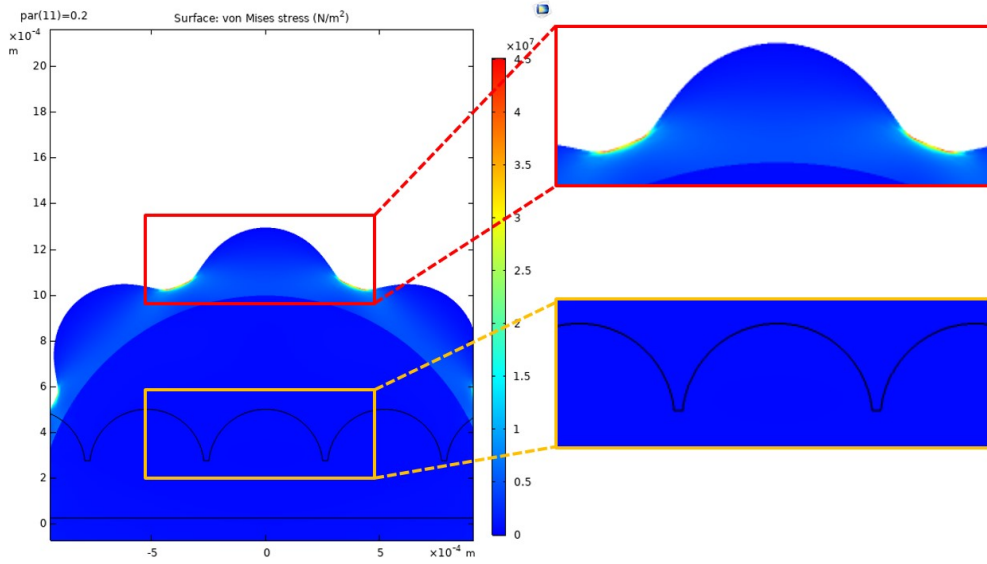


Figure 3.22: Deformation of micro-lens on a curved surface with $R=1$

To further investigate what would happen to the lenses when the curvature was given, a simulation tool COMSOL (COMSOL multiphysics, COMSOL Inc., MA, USA) was used as shown in Figure 3.22. With $R=1$, the lens deformation significantly affected its height, width, and pitch length. The height of the lens decreased, the width was dilated, and the pitch, or the gap between the lenses, was also increased.

Figure 3.23 shows design schematics of the two different micro-lens arrays. Figure 3.23(a) is the case where the micro-lens arrays are made of PDMS only with closely packed lenses with the radius of 0.25 mm allowing only 0.02 mm of distance between the lenses, and Figure 3.23(b) is designed similarly to the PDMS-PTFE micro-lens array that introduced previously. Due to the nature of the COMSOL Multiphysics tool,

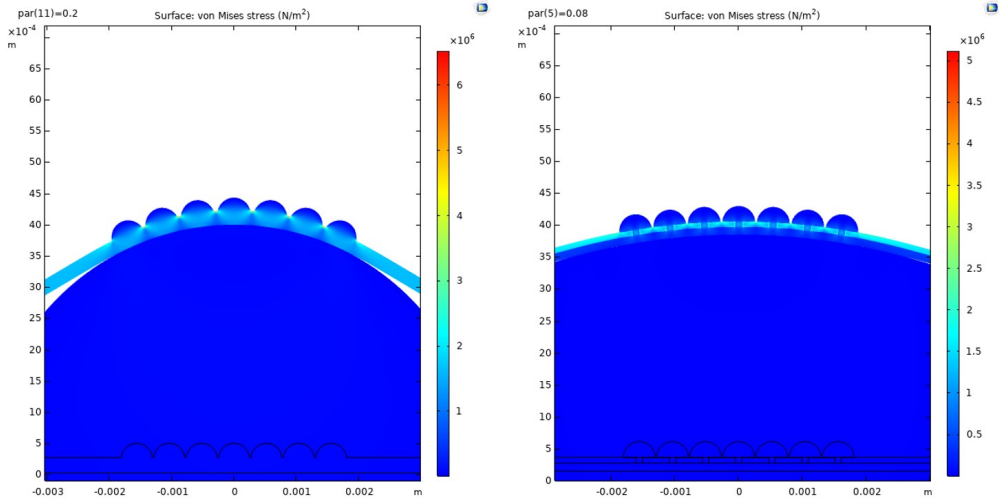


Figure 3.23: Deformation comparison design schemes. (a) Deformation of micro-lens array made of PDMS. (b) Deformation of micro-lens array with PTFE light-screen layer

the two ends of the micro-lens array layer are set to the ‘fixed constraint,’ and by allowing the circular ball to move upward to the micro-lens array, instead of simulating a situation where the micro-lens array is laid on a curvature. The mechanical stress engaged in the micro-lens arrays was observed. The bottom of the micro-lens array and the top half of the ball was set to ‘contact pair’, and a two-parameter Mooney-Rivlin hyperelastic material model was used. The stress was engaged until the lenses at the third layer were perfectly in contact with the ball to ensure they were in the curvature R .

The simulation resulted in the reduced height, increased width, and pitch length for both micro-lens arrays, as Figure 3.24 demonstrates. The rate of change gradually decreased as the curvature increased, but they showed subtle differences in each category. While PDMS MLA consistently had approximately 5% of change in the height of the lens, the one with the PTFE layer showed less than 2% of change or even no changes starting from $R = 6$ mm. Regarding width, both micro-lens arrays had 3-4%

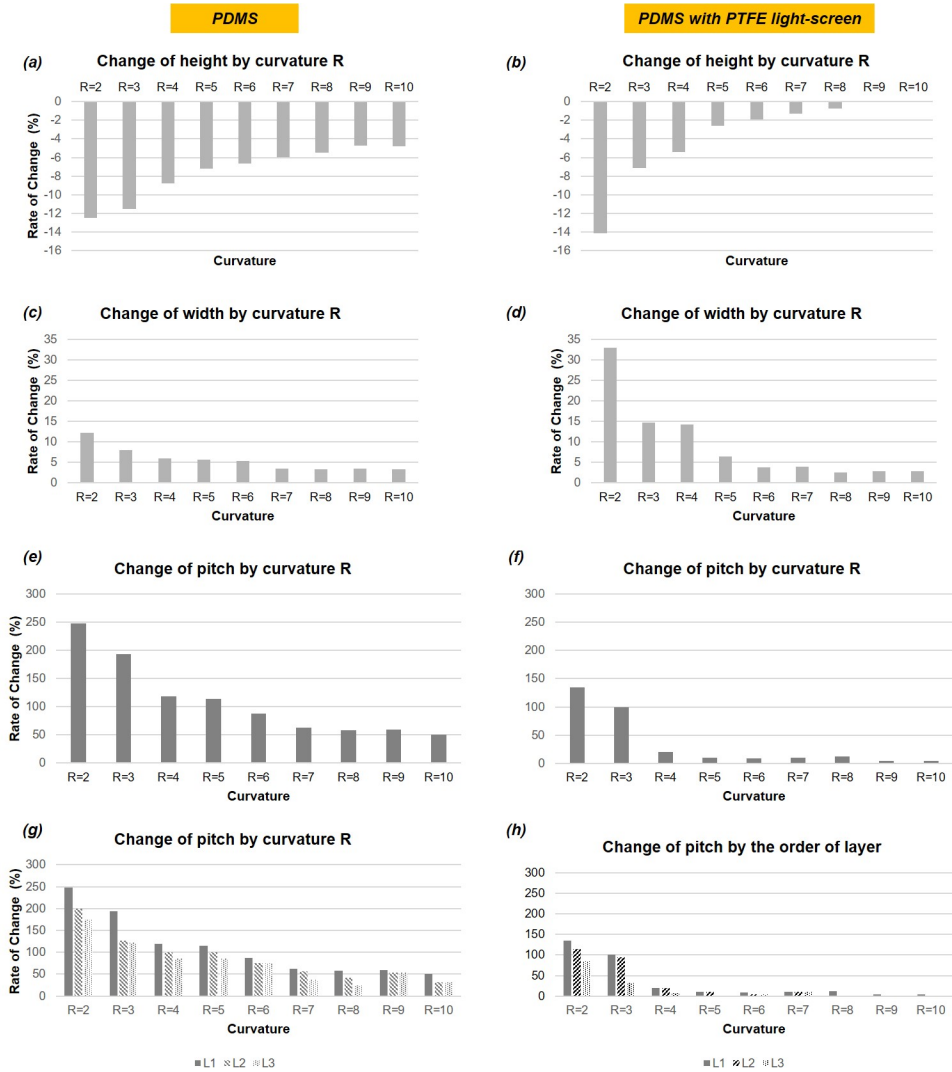


Figure 3.24: Deformation comparisons. (a) Rate of changes in height for PDMS. (b) Rate of changes in height for PDMS-PTFE MLA. (c) Rate of changes in width for PDMS. (d) Rate of changes in width for PDMS-PTFE MLA. (e) Rate of changes in pitch length for PDMS. (f) Rate of changes in pitch length for PDMS-PTFE MLA. (g) Rate of changes in pitch length for PDMS depends on the layer order. (h) Rate of changes in pitch length for PDMS-PTFE MLA depending on the order of layer.

of changes in higher curvature, while they showed different behavior in pitch length. For PDMS MLA, the pitch length consistently showed above 50% of change until $R = 10$ mm, while PDMS-PTFE MLA showed a greatly reduced rate of change starting from $R = 4$ mm, only about 10% for R from 5 to 8, and less than 5% from $R = 9$ mm. As the ‘layer’ increases at the same curvature, the height and width differences exist but are minimal. The pitch length, however, showed a noticeable decrease as they are located further from the central reference lens, as shown in Figure 3.24(g) and (h).

Through the simulation, it is evident that the dimensions of the lenses change depending on the radius of curvature. Assuming that the deformed lens is still in circular shape after deformation, with the rate of change value, it would be possible to obtain a new radius value for the distorted lens. Assuming that the original circle was on a Cartesian coordinate system, three points that were $(-r,0)$, $(r,0)$, and $(0,r)$ before deformation would be $(-w,0)$, $(w,0)$, and $(0,h)$, respectively, after deformation. One can easily find the relationship between the coefficients in the general form equation and the deformed width w and height h by substituting x and y in 3.23 with the points $(-w,0)$, $(w,0)$, and $(0,h)$. Starting with the general form equation of a circle:

$$x^2 + y^2 + Ax + By + C = 0 \quad (3.23)$$

For $(w,0)$,

$$w^2 + Aw + C = 0 \quad (3.24)$$

For $(-w,0)$,

$$w^2 - Aw + C = 0 \quad (3.25)$$

For $(0,h)$,

$$h^2 + Bh - w^2 = 0 \quad (3.26)$$

By subtracting Equation 3.25 from Equation 3.24, we have:

$$\begin{aligned} 2Aw &= 0 \\ A &= 0 \end{aligned} \tag{3.27}$$

By adding Equation 3.25 and Equation 3.24, we have:

$$\begin{aligned} w^2 + C &= 0 \\ C &= -w^2 \end{aligned} \tag{3.28}$$

By subtracting Equation 3.24 from Equation 3.26:

$$\begin{aligned} h^2 + Bh - w^2 &= 0, \\ Bh &= w^2 - h^2, \\ B &= \frac{w^2 - h^2}{h} \end{aligned} \tag{3.29}$$

The radius of the circle can be found in terms of A, B, and C from Equation 3.30,

$$r = \frac{\sqrt{A^2 + B^2 - 4C}}{2} \tag{3.30}$$

By applying A, B, and C represented in terms of w and h to Equation 3.30, we have:

$$\begin{aligned} r_{deform} &= \frac{\sqrt{(\frac{w^2-h^2}{h})^2 + 4w^2}}{2}, \\ &= \frac{\sqrt{\frac{w^4+h^4-2w^2h^2}{h^2} + 4w^2}}{2}, \\ &= \frac{\sqrt{\frac{w^4+h^4-2w^2h^2+4w^2h^2}{h^2}}}{2}, \\ &= \frac{\sqrt{\frac{w^4+h^4+2w^2h^2}{h^2}}}{2}, \\ &= \frac{\sqrt{(\frac{w^2+h^2}{h})^2}}{2}, \\ &= \frac{w^2 + h^2}{2h} \end{aligned} \tag{3.31}$$

Combined with the plano-convex lens maker's equation (Equation 3.6):

$$\begin{aligned}\frac{1}{f} &= (n' - 1) \cdot \frac{1}{\frac{w^2 + h^2}{2h}} \\ &= (n' - 1) \cdot \frac{2h}{w^2 + h^2}\end{aligned}\quad (3.32)$$

Therefore, an equation for the focal length that is altered due to applying curvature can be obtained as follows:

$$f = \frac{w^2 + h^2}{(n' - 1)2h} \quad (3.33)$$

Using the deformation data obtained from Figure 3.24 and Equation 3.33, new focal lengths for the lens that had 0.25 mm of radius, which previously had 0.6038 mm of focal length can be obtained as shown in Figure 3.25.

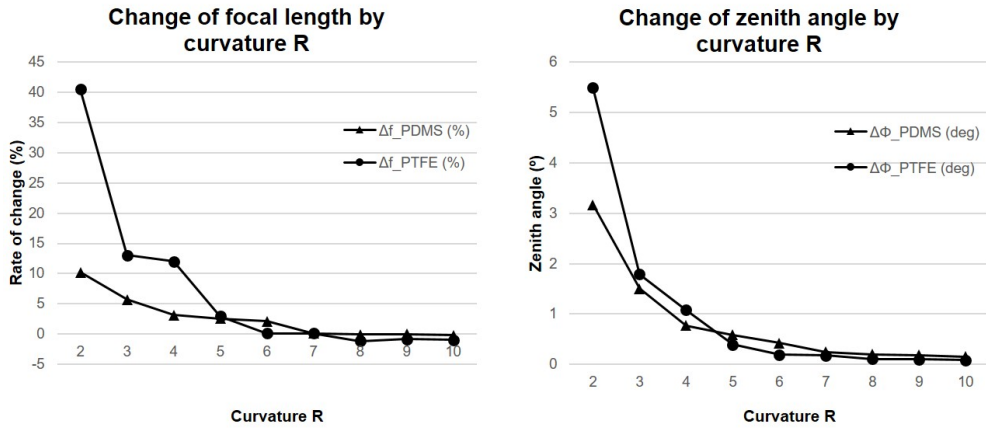


Figure 3.25: Focal length and zenith angle changes after deformation.

As the curvature increases, the focal length also increases, and the tendency converges approximately at 15% for both micro-lens arrays when curvature is larger than 4 (Figure 3.25(a)). Increased pitch and width of the lenses also affect the zenith angle. Compared to the case that it should have been without considering the deformation of the lenses, the zenith angle increased up to 5 °when R=2. When the curvature is larger

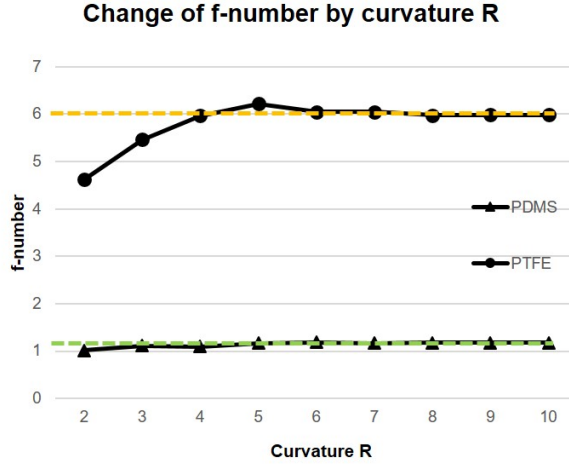


Figure 3.26: f-number changes after deformation. The green and yellow lines indicate the f-numbers of PDMS version and PTFE version, respectively.

than 4, both micro-lens arrays showed less than 1 °difference (Figure 3.25(b)). Considering the lenses' deformation, curvatures from 5 to 10 are reasonable since changes in height, width, pitch, focal length, and zenith angle are predictable and minimal. However, another factor to consider is that whether this small curvature is achievable in real-world fabrication with the corresponding materials. Since the delamination of the two materials due to the difference in Young's modulus is not considered during the simulation, it may be difficult to implement in actual manufacturing.

To conclude, the curvature R of the curved micro-lens array must have a value of R greater than the focal length f. The simulation result validated that applying curvature to the flat micro-lens array brings deformation to the dimensions, such as the height, width, and pitch of the lenses. Above a certain value of R, however, the rate of change is steady, and the f-number converges the original f-number of the lenses as R increases. Considering the range of R from the maximum field-of-view, and the range of R from the deformation results, it can be concluded that the optimal value of R should be where the rate of change starts to converge.

3.3 Conclusion

To summarize, the micro-lens array developed in this dissertation had a relatively long focal length compared to other existing micro-lens arrays due to the smaller size of the aperture set. Reducing the aperture size has the advantage of increasing the visible range, but it also has the drawback of reducing the field-of-view and brightness of each sub-image. Even though the micro-lens array innately allows acquisition of wider field-of-view compared to having a single lens, to compensate for this reduction in FOV, the lenses can be arranged on a curved surface. By arranging the lenses on a curved surface, it is possible to secure a wider FOV and capture a larger portion of the scene. This curvature helps to overcome the limitations imposed by the reduced aperture size and allows for a greater coverage of the surrounding space. Furthermore, since changing the aperture also changes the focal length, implementing a variable aperture is not suitable unless the system can afford hundreds and thousands of voltage for shrinkage of EAP, or has a mechanical setup that can alter the distance between the micro-lens array and the image sensor.

Regarding the arrangement of the micro-lens array, a hexagonal array is advantageous over a rectangular array for both 2D and 3D cases because it has a higher fill factor and lower complexity. When arranging it in a 3D structure, as the lenses are located away from the center, the distance between the sensor and the lens becomes shorter and tilted. Therefore, the size and shape of the lenses need to be optimized according to the zenith angle. The finding includes that the number of layers is limited depending on the size of the sensor and the minimal number of layers required to achieve 180° , although the size of the sensor was neglected in some cases. It was also found that the deformation of the lenses exist when applying curvature to the micro-lens array film, but physical properties and performance of the lenses remain constant after a certain value of R . Considering the maximum field-of-view with the convergence of the rate of change, an optimal value for the curvature could be obtained.

Chapter 4

Application

4.1 Use of multiple aspect

Micro-Lens Array based computer vision can be utilized in various conditions that require use of multiple images of a scene taken at different aspects for information acquisition.

4.1.1 Small robot application

Recent advances in the deep-learning involved computer vision research led to the development of algorithms suitable for compound eye camera systems [65, 66, 67]. These algorithms gather and compare pixels from each micro-lens, and ‘source image’ and ‘target image’ are obtained. It then produces n by n directional information indicating the flow of motion where the scene is heading through ‘final classification’, as illustrated in Figure 4.1. Although they successfully implemented the unique local motion classification algorithms for the compound eye camera system, those systems acquired images from multiple regular cameras positioned at various angles, which is different from ‘compound eye’ system that aims to achieve in a small platform. Therefore, a collaborative work was done with Hwiyeon Yoo from RLLAB, Seoul National University.

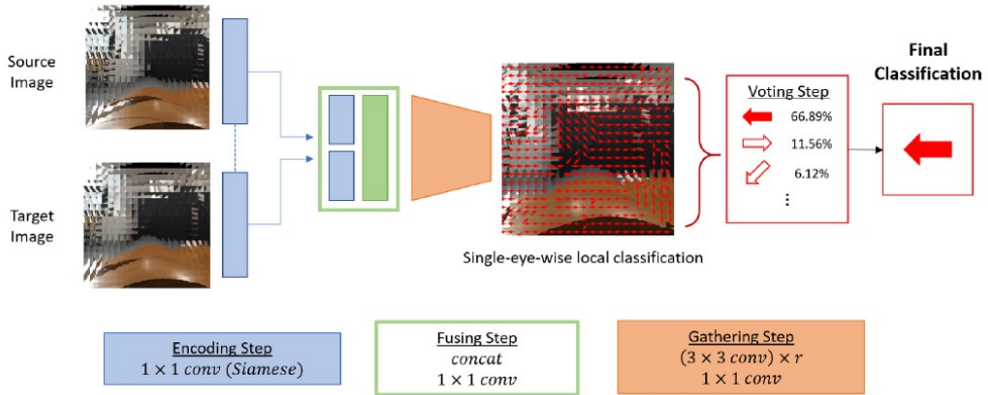


Figure 4.1: Deep Ego-motion Classification

Based on the previously introduced PTFE-PDMS micro-lens array, an octagonally arranged micro-lens array was fabricated as shown in Figure 4.2. The reason for the octagonal arrangement was for the seamless integration of the software and hardware. RRLAB's deep-learning model requires spherically arranged 'n by n' number of lenses, while the fabrication process of the PTFE-PDMS micro-lens array could not reduce the size of the lenses for that n by n feature - the sensor was not in square, and 'n' needed to be an odd number that has a central image as a reference, making the octagonal arrangement a point of compromise. The octagonal arrangement meets all the software requirements (3 by 3 lenses, spherically positioned with a reference lens at the center) and for the hardware-wise, all the lenses were able to capture clear images.

Figure 4.3 shows the resulting images from the collaborative work. By comparing the source image and the target image, the 'single-eye-wise classification' produces local motion change and the final classification state determines how the image moved from previous status. The proposed compound eye camera could produce more detailed and accurate information other than up/down or left/right if it had more number of lenses for calculation. The trade-off of this system is the number of lenses for a limited size of the image sensor. More lens means more images to compare with much

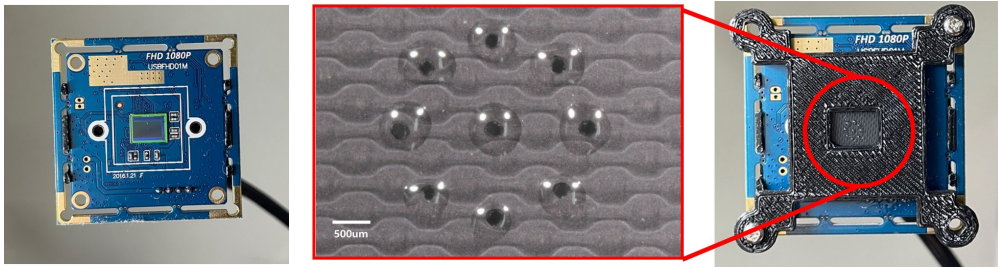


Figure 4.2: Octagonal compound eye camera

accurate information, however, increased number of lenses results in decreased size of each micro-lens, leading to shortening the visual range of the system. The work had been introduced in ICCAS 2021.

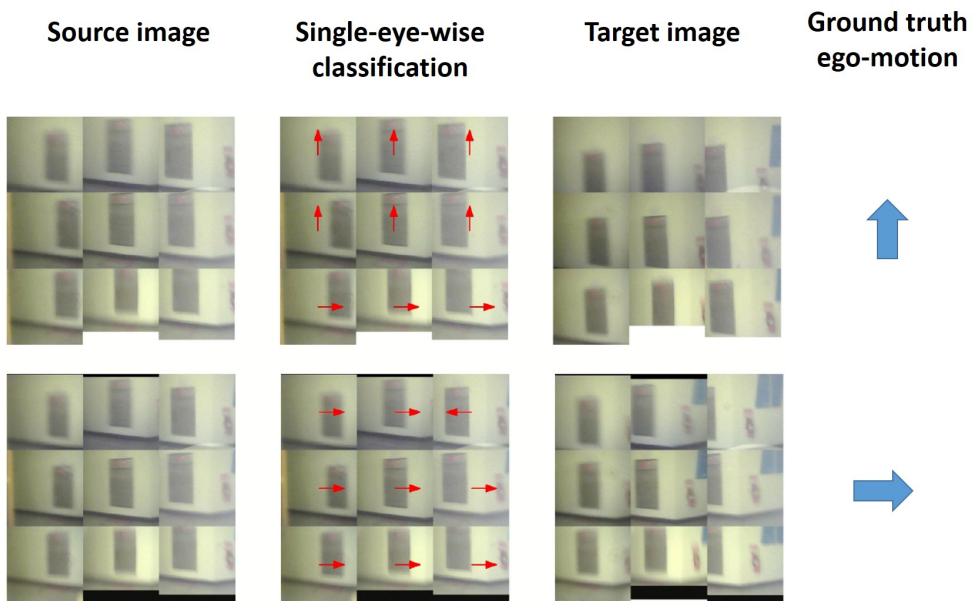


Figure 4.3: Result of the combination of the software and hardware

4.1.2 Micro-lens array for Artificial Retina

The Micro-lens array system can also be used for artificial retinas. Artificial retina, or retinal prosthesis is one of the implantable prosthetic devices that electrically stimulates the designated region of the retina to treat diseases such as retinis pigmentosa or age-related macular degeneration. Researchers around the world have been developed retinal prosthesis in various shapes and methods [68, 69, 70, 71]. Current artificial retina system can be divided into external devices and internal devices. External devices include goggles, a camera mounted on it, video processing unit, and external coil for power supply. The internal device consists of an internal coil to receive power and a stimulating electrode to electrically stimulate the retina. Briefly, the principle of operation of the artificial retina system is as follows: the image acquired through the camera attached to the goggle is pixelated through video processing unit, the edge detection algorithm extracts edges of the surroundings during the video processing step, and the electrode for the corresponding area is stimulated to stimulate the retina, artificially transmitting electrical signals to the retina to restore vision.

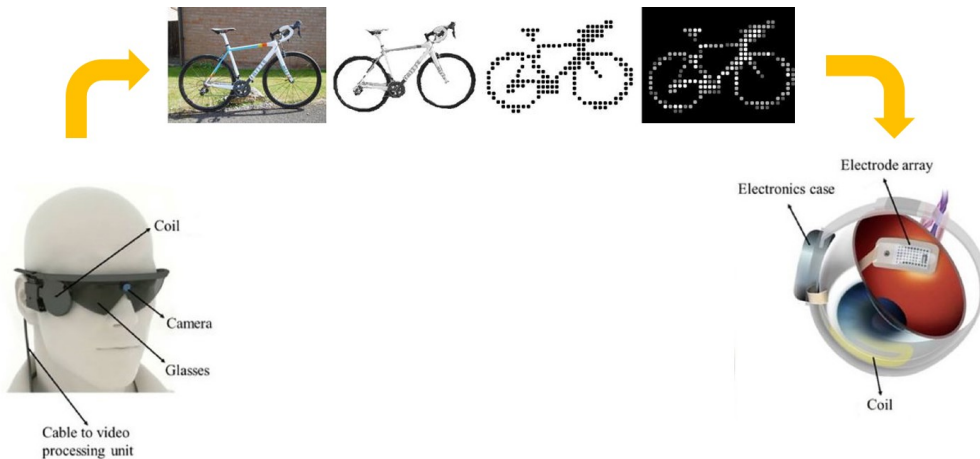


Figure 4.4: Artificial Retina system overview

However, problems arise when the wearer gazes elsewhere. Since the camera attached to the goggles is essentially facing forward, there can be a discrepancy between

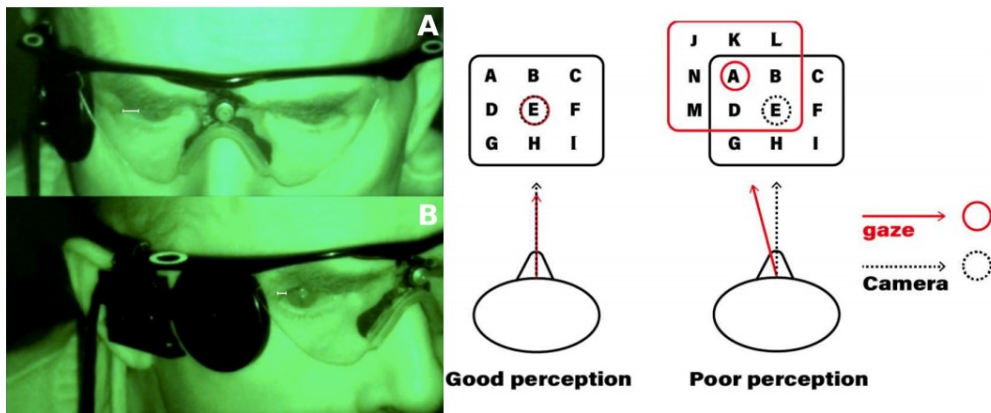


Figure 4.5: Artificial Retina system when the patient gazes sideways

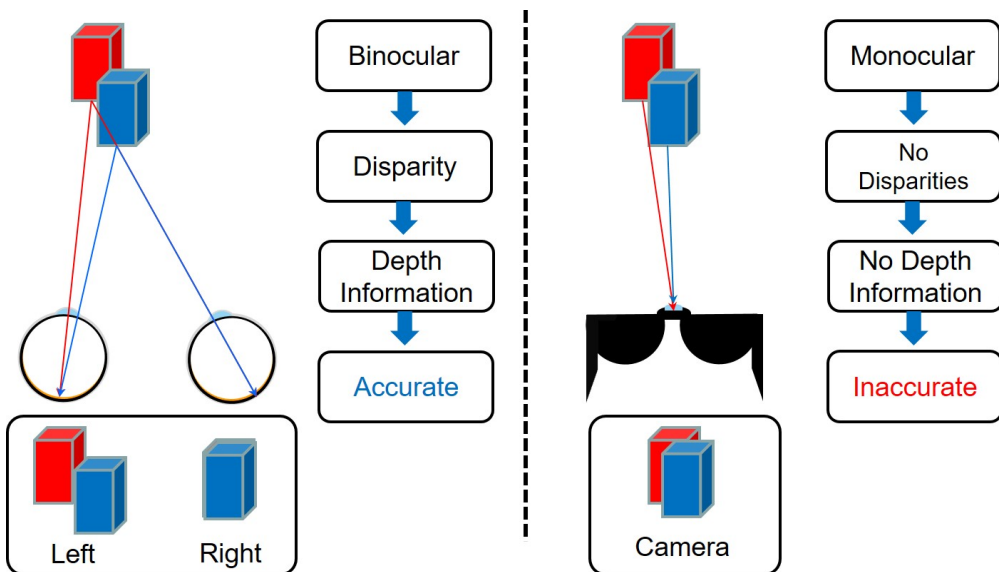


Figure 4.6: Comparison of the binocular and monocular system in terms of the depth information

the visual information provided by the camera and the information perceived by the wearer when they try to look at objects using their peripheral vision. This mismatch can lead to issues and difficulties. Specifically, it had been reported that the field of view of the patients is limited to the “immediate field of view” of the binocular vision along with decreased perception and recognition in object localization [72, 73, 74, 75].

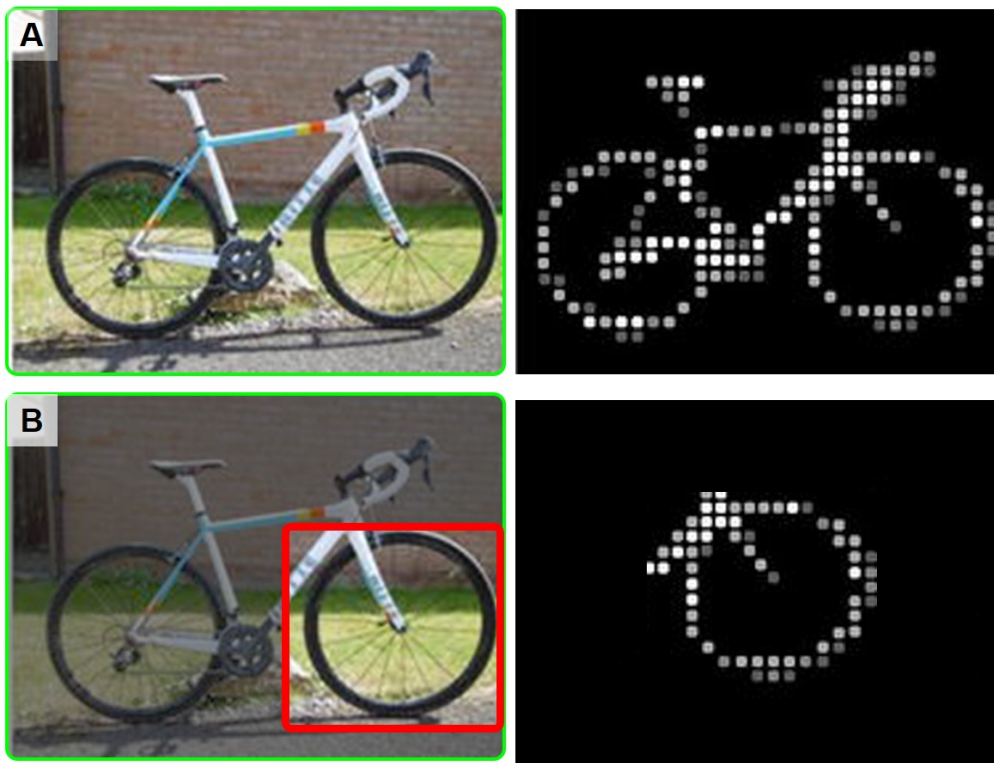


Figure 4.7: Artificial Retina system solution. (A) Example image when seen by the mounted camera, (B) Suggested image when considering the gaze.

The most intuitive way to observe an object from various angles is to rotate the camera itself according to the movement of the eyes. Similar method is widely adopted for commercially available surveillance cameras to detect motion and follow the object. Using the pan-tilt functionality along with eye tracking capability, more sophisticated image could be obtained for the retinal prosthesis. The advantage of the system

is that it can easily be adopted for the image processing part of the existing retinal prosthesis since it only requires small stepper motors around the camera for the pan-tilt functionality, and it offers a wide field-of-view owing to its rotation of the camera. However, the system might not be suitable for human-worn device considering inevitable size and volume increase of the system.

Due to the goggle-mounted nature of the vision system, it is essential for the system to have a smaller and lighter camera and the pan-tilt camera cannot provide such capabilities since it requires ponderous rotary system for camera movement. Moreover, power consumption for the rotary action is another factor to consider for such a condition where the energy resource is limited. On the other hand, compound eye camera is more suitable for the light weight and small camera system since it does not occupy much space since the lens system is all that is needed to be replaced.

In addition, multi-perspective view from the compound eye system is beneficial for visual perception of the patients since a number of the same target object seen from a different viewing angle offers depth information. Using the depth information, more sophisticated electrical stimulation is possible that gives stereopsis-like experience for the patient by varying the amplitude of stimulation. However, this must be followed by the advancement of the electrodes. Argus-II has only 6 by 10 electrodes and Alpha-IMS has 38 by 40 electrodes. As long as the edge detection is available from the pre-processed image, image quality due to the low number of electrodes will serve the purpose. However, the number of the electrodes need to be increased at least up to 100 by 100 provide sense of distance through the retinal prosthesis with compound eyes.

Short visual range and the subdivided region of the image sensor due to the multiple lenses are the major factors that affect the low resolution of the resulting image from the compound eye camera. However, considering that the original image obtained from the external camera is down-scaled or pixelated during the image pre-processing stage to be suitable for the electrode, the problem is less of a concern. As long as the number of pixels a micro-lens produces is greater than the number of electrodes, the

visual prosthesis will provide sufficient images. For the short visual range of the compound eye cameras with micro-lens array, researches introduced earlier successfully obtained clear vision as far as one meter. Although a meter of clear visual range is not sufficient for the human binocular vision, the objects that are out of focus are not meaningless as long as edge detection is possible through the pre-processed image.

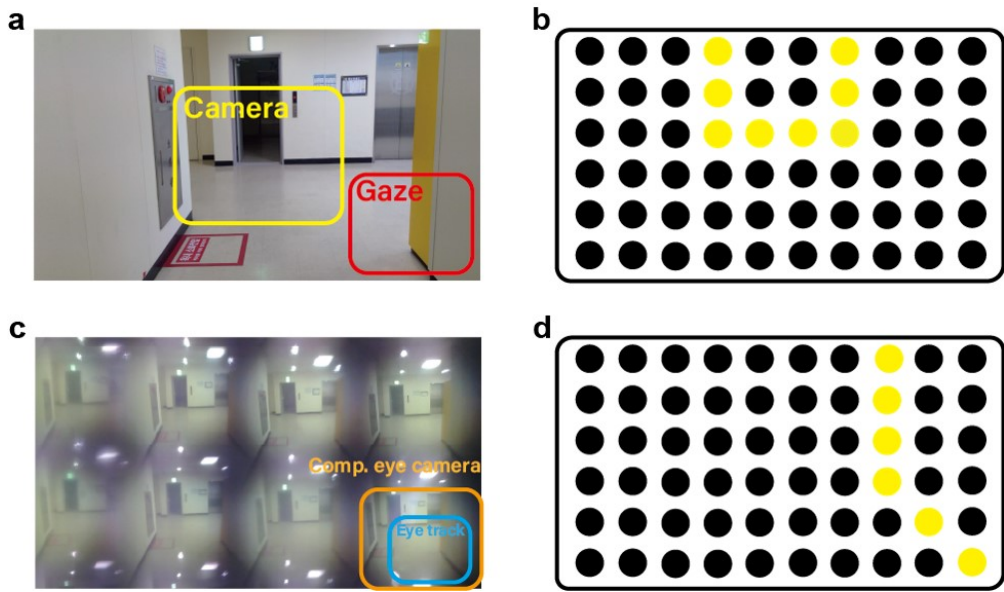


Figure 4.8: Expected result when the micro-lens array is applied to the artificial retina system

Expected Result

Conventional cameras adopted to the current retinal prosthesis system provides an image as shown in Fig. 2a. After the pre-processing of the given information, the electrodes would produce stimulation patterns shown in Fig. 4.8b., even though the patient's gaze is set on the corner of the aisle (red box in Fig. 4.8a.). On the other hand, the proposed compound eye camera system provides a number of similar images seen from different perspectives as illustrated in Fig. 4.8c., producing a stimulation pattern as shown in Fig. 4.8d. which is close to what the patient is staring at. As a result, The

compound eye camera system is proposed as a method to improve the perception of the patients with retinal prosthesis. With a combination of eye tracking technology and a compound eye camera, it is expected to align the visual axis of the gaze and the camera for an enhanced perception.

4.1.3 Other possible applications

Micro-lens array in 3D localization

Micro-lens arrays can also be used to track an object moving in a 3D space [28]. This study also designed a micro-lens array aligned on a curved surface. It adopted a ‘dome light cone’ between the micro-lens array and the image sensor to compensate for the image distortion due to the focal length difference. Using the ‘3D localization algorithm’ of their own, they successfully tracked an object moving in an arbitrary direction in space, as shown in Figure 4.9. This research not only confirmed the use-

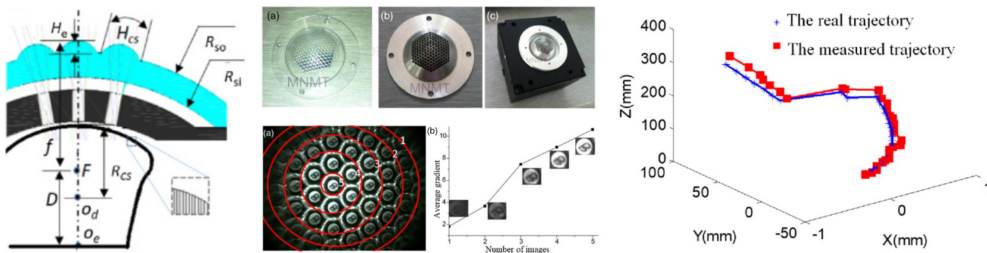


Figure 4.9: Overview of the 3D trajectory system using Micro-Lens Array^[28]

fulness of micro-lens arrays for object localization but also highlighted the advantages of employing a 3D curved design in such applications. However, the drawback lies in the utilization of the dome light cone, which resulted in a bulky system that is unsuitable for small robot applications.

Disparity map

Another useful application of micro-lens arrays is disparity map. Disparity map, or depth map, is a type of image that contains spatial information about an object,

especially the distance between objects in a scene and the camera. It is a 2D representation of a 3D scene, where each pixel in the image contains a value that represents its distance from the camera. Conventional depth map makes use of a single lens camera, which is limited in obtaining precise depth information. However, it is possible to obtain comprehensive depth map using micro-lens array, since multiple images seen from different aspects are captured for a scene. Figure 4.10 shows depth map cre-

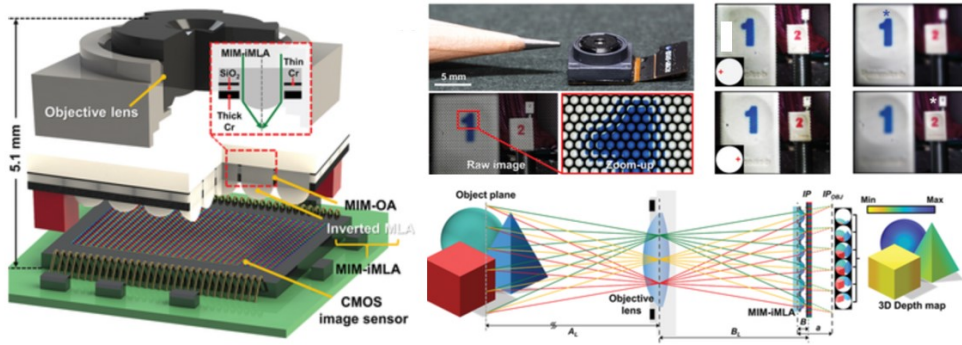


Figure 4.10: Disparity map created by a micro-lens array^[76]

ated by micro-lens arrays [76]. Although the study managed to obtain precise depth map through the fabricated micro-lens array, the use of objective lens for increased visual range and depth-of-field inevitably resulted in that of an apposition compound eye camera, which means it is more close to an pixelated image rather than multiple images seen by different aspects.

Chapter 5

Summary

This study compares the visual systems of insects and humans, explaining the need to replicate insects' compound eyes for small robot applications. It presents three different innovative fabrication methods for micro-lens arrays: a PVC-based flexible micro-lens array, COC-based micro-lens array utilizing the thermal-reflow method, and light screen-aperture integrated flexible micro-lens array created through the protrusion fabrication method, all of which has the light-screen layer the mimicked pigment cell of the compound eye of the insects for improved image quality. The initially adopted PDMS-PVC micro-lens array, chosen for its flexibility, had very small lenses, resulting in a short visual range of a few centimeters. Additionally, there were issues related to thermal properties during the fabrication process, as PVC shrinks under heat while PDMS undergoes curing due to heat. To address these challenges, a COC-CB micro-lens array was created by incorporating a mixture of PDMS and carbon black into the heat-resistant COC micro-lens array. This research demonstrated the role of the light-screen successfully. However, due to the difficulty in achieving curvature with COC MLA, PDMS was once again adopted as the lens material. A flexible micro-lens array was then completed using the protrusion method, allowing for free variation of the aperture size. The integrated design of the screen-aperture micro-lens array demonstrates a superior visual range of one meter while maintaining a wide field of view of

100 °, surpassing conventional micro-lens arrays. The artificial compound eye, with its extended visual range and multi-perspective capabilities, allows for distance data acquisition from captured images.

Design principles for micro-lens arrays are proposed, comparing the arrangements in both 2D and 3D contexts. In terms of the aperture, reducing the aperture size increases the visible range but decreases the field-of-view and brightness of each sub-image. To compensate for the reduced FOV, the lenses can be arranged on a curved surface, allowing for a wider FOV and capturing a larger portion of the scene. This curvature helps overcome limitations imposed by the smaller aperture size and provides better coverage of the surrounding space. Implementing a variable aperture is not feasible unless the system can handle significant voltage changes or has a mechanical setup to adjust the distance between the micro-lens array and the image sensor.

As for the arrangement of the lenses, the hexagonal arrangement is found to be advantageous in terms of packing density and computational simplicity, making it a better choice for curved surface computer vision applications. When placing micro-lens arrays on curved surfaces, the study suggests the maximum number of lenses, field of view, and focal length adjustments based on the zenith angle was also considered unlike any other micro-lens array research. However, the number of layers is limited by the sensor's size, so it was necessary to determine the maximum number of lenses that could be accommodated and the resulting FOV.

Lastly, various application examples utilizing micro-lens arrays were introduced. In the first example, the integration with the latest trend of machine learning was demonstrated by representing camera or object motion vectors. The second example showcased the advantages of integrating micro-lens arrays into systems like artificial retinas. The remaining examples highlighted the utilization of micro-lens arrays in 3D trajectory and depth mapping, emphasizing the strengths of multi-aspect vision of micro-lens arrays when employed in small computer vision applications.

These improvements and analyses demonstrate the potential of the developed micro-

lens array to overcome current limitations and enhance its suitability for future computer vision systems. Given its relatively longer visible range and the ability to acquire spatial data, the micro-lens array can be applied to computer vision systems for small robots and endoscopy applications requiring precise distance measurements in a compact form factor.

Bibliography

- [1] Otto V.M. Bueno, Jose J. Benitez, and Miguel A. San-Miguel. 9 - computational design of cutin derivative bio-materials from fatty acids. In Liliana Mammino, editor, *Green Chemistry and Computational Chemistry*, Advances in Green and Sustainable Chemistry, pages 215–243. Elsevier, 2022.
- [2] Filia Nauli Hapsari, Ratna Purwaningsih, Faradhina Azzahra, and Diana Puspita Sari. Velcro product design with biomimicry approaches. *IOP Conference Series: Earth and Environmental Science*, 1111(1):012057, dec 2022.
- [3] Julian K A Langowski, Dimitra Dodou, Peter van Assenbergh, and Johan L van Leeuwen. Design of Tree-Frog-Inspired Adhesives. *Integrative and Comparative Biology*, 60(4):906–918, 05 2020.
- [4] Gabriella Meloni, Omar Tricinci, Andrea Degl’Innocenti, and Barbara Mazzolai. A protein-coated micro-sucker patch inspired by octopus for adhesion in wet conditions. *Scientific Reports*, 10(15480), 2020.
- [5] B. Kollbe Ahn. Perspectives on mussel-inspired wet adhesion. *Journal of the American Chemical Society*, 139(30):10166–10171, 2017. PMID: 28657746.
- [6] Gregory D. Bixler and Bharat Bhushan. Fluid drag reduction with shark-skin riblet inspired microstructured surfaces. *Advanced Functional Materials*, 23(36):4507–4528, 2013.

- [7] Robert Siddall and Mirko Kovac. *Bioinspired Aerial Robots*, pages 1–12. Springer Berlin Heidelberg, Berlin, Heidelberg, 2020.
- [8] V A Tucker. The deep fovea, sideways vision and spiral flight paths in raptors. *J Exp Biol*, 203(Pt 24):3745–3754, December 2000.
- [9] Matthias Ott. Chameleons have independent eye movements but synchronise both eyes during saccadic prey tracking. *Experimental Brain Research*, 139(2):173–179, July 2001.
- [10] Frank Schaeffel, Christopher J. Murphy, and Howard C. Howland. Accommodation in the cuttlefish (*Sepia officinalis*). *Journal of Experimental Biology*, 202(22):3127–3134, 11 1999.
- [11] Lydia M. Mather, Roger T. Hanlon, Jonas Hansson, and Dan-Eric Nilsson. The w-shaped pupil in cuttlefish (*sepia officinalis*): Functions for improving horizontal vision. *Vision Research*, 83:19–24, 2013.
- [12] D.B. Henson. *Visual Fields*. Oxford medical publications. Oxford University Press, 1993.
- [13] Arjun Krishnaswamy, Masahito Yamagata, Xin Duan, Y. Kate Hong, and Joshua R. Sanes. Sidekick 2 directs formation of a retinal circuit that detects differential motion. *Nature*, 524:466–470, 08 2015.
- [14] Sören J Zapp, Steffen Nitsche, and Tim Gollisch. Retinal receptive-field substructure: scaffolding for coding and computation. *Trends in Neurosciences*, 45(6):430–445, June 2022.
- [15] Chelsea Sabo, Robert Chisholm, Adam Petterson, and Alexander Cope. A lightweight, inexpensive robotic system for insect vision. *Arthropod structure development*, 46, 08 2017.

- [16] Zefang Deng, Feng Chen, Qing Yang, Hao Bian, Guangqing Du, Jiale Yong, Chao Shan, and Xun Hou. Dragonfly-eye-inspired artificial compound eyes with sophisticated imaging. *Advanced Functional Materials*, 26(12):1995–2001, 2016.
- [17] Wolfgang Stürzl, Norbert Böldcker, Laura Dittmar, and Martin Egelhaaf. Mimicking honeybee eyes with a 280 field of view catadioptric imaging system. *Bioinspiration & biomimetics*, 5(3):036002, 2010.
- [18] R.E. Ritzmann and J.A. Bender. *Insect Flight and Walking: Neuroethological Basis*, pages 155–160. 12 2010.
- [19] Julien R. Serres and Franck Ruffier. Optic flow-based collision-free strategies: From insects to robots. *Arthropod Structure Development*, 46(5):703–717, 2017. From Insects to Robots.
- [20] Alexander Borst, Michael Drews, and Matthias Meier. The neural network behind the eyes of a fly. *Current Opinion in Physiology*, 16:33–42, 2020. Vision Physiology.
- [21] Nicholas J. Strausfeld. The lobula plate is exclusive to insects. *Arthropod Structure Development*, 61:101031, 2021.
- [22] Brian Guenter, Neel Joshi, Richard Stoakley, Andrew Keefe, Kevin Geary, Ryan Freeman, Jake Hundley, Pamela Patterson, David Hammon, Guillermo Herrera, Elena Sherman, Andrew Nowak, Randall Schubert, Peter Brewer, Louis Yang, Russell Mott, and Geoff McKnight. Highly curved image sensors: a practical approach for improved optical performance. *Opt. Express*, 25(12):13010–13023, Jun 2017.
- [23] Christophe Gaschet, Wilfried Jahn, Bertrand Chambion, Emmanuel Hugot, Thibault Behaghel, Simona Lombardo, Sabri Lemared, Marc Ferrari, Stéphane

- Caplet, S. Getin, Aurélie Vandeneynde, and David H. Henry. Methodology to design optical systems with curved sensors. *Applied optics*, 58 4:973–978, 2019.
- [24] Dmitry Reshidko and Jose Sasian. Optical analysis of miniature lenses with curved imaging surfaces. *Appl. Opt.*, 54(28):E216–E223, Oct 2015.
- [25] Stefan Sinzinger. 3.02 - diffractive and defractive micro-optics. In Yogesh B. Gianchandani, Osamu Tabata, and Hans Zappe, editors, *Comprehensive Microsystems*, pages 65–99. Elsevier, 2008.
- [26] Hao Zhang, Lei Li, David L. McCray, Sebastian Scheiding, Neil J. Naples, Andreas Gebhardt, Stefan Risse, Ramona Eberhardt, Andreas Tünnermann, and Allen Y. Yi. Development of a low cost high precision three-layer 3d artificial compound eye. *Opt. Express*, 21(19):22232–22245, Sep 2013.
- [27] Young Min Song, Yizhu Xie, Viktor Malyarchuk, Jianliang Xiao, Inhwa Jung, Ki-Joong Choi, Zhuangjian Liu, Hyunsung Park, Chaofeng Lu, Rak-Hwan Kim, Rui Li, Kenneth B. Crozier, Yonggang Huang, and John Rogers. Digital cameras with designs inspired by the arthropod eye. *Nature News*, May 2013.
- [28] Yelong Zheng, Le Song, Jingxiong Huang, Haoyang Zhang, and Fengzhou Fang. Detection of the three-dimensional trajectory of an object based on a curved bionic compound eye. *Opt. Lett.*, 44(17):4143–4146, Sep 2019.
- [29] Changhoon Baek, Jungho Yi, and Jong mo Seo. Low-cost, thermoplastic micro-lens array with a carbon black light screen for bio-mimetic vision. *Opt. Express*, 29(22):35172–35181, Oct 2021.
- [30] Dongmin Keum, Kyung-Won Jang, Daniel S. Jeon, Charles S. H. Hwang, Elke K. Buschbeck, Min H. Kim, and Ki-Hun Jeong. *Xenos peckii* vision inspires an ultrathin digital camera. *Light: Science and Applications*, 7(1), 2018.

- [31] Kiwoon Choi, Chul Jin Jo, and Han Sup Lee. A self-aligned aperture-microlens array. *RSC Adv.*, 4:3009–3015, 2014.
- [32] Sang-In Bae, Kisoo Kim, Kyung-Won Jang, Hyun-Kyung Kim, and Ki-Hun Jeong. High contrast ultrathin light-field camera using inverted microlens arrays with metal–insulator–metal optical absorber. *Advanced Optical Materials*, 9(6):2001657, 2021.
- [33] Minwon Seo, Jong-Mo Seo, Dong-Il Cho, and Kyo-In Koo. Insect-mimetic imaging system based on a microlens array fabricated by a patterned-layer integrating soft lithography process. *Sensors*, 18(7):2011, 2018.
- [34] Simon Thiele, Kathrin Arzenbacher, Timo Gissibl, Harald Giessen, and Alois M. Herkommer. 3d-printed eagle eye: Compound microlens system for foveated imaging. *Science Advances*, 3(2):e1602655, 2017.
- [35] Hyun Myung Kim, Min Seok Kim, Gil Ju Lee, Young Jin Yoo, and Young Min Song. Large area fabrication of engineered microlens array with low sag height for light-field imaging. *Opt. Express*, 27(4):4435–4444, Feb 2019.
- [36] Hyukjin Jung and Ki-Hun Jeong. Monolithic polymer microlens arrays with high numerical aperture and high packing density. *ACS Applied Materials & Interfaces*, 7(4):2160–2165, Feb 2015.
- [37] Scott Lambert and Martin Wagner. *Microplastics Are Contaminants of Emerging Concern in Freshwater Environments: An Overview*, pages 1–23. 01 2018.
- [38] Zeynep Yeşim İlerisoy and Burcu Çolak. *DISCOVERY OF INNOVATIVE MATERIALS IN STRUCTURAL SYSTEM DESIGN: GLASS STRUCTURES*, pages 1225–1237. 10 2018.
- [39] A. Syafiq, B. Vengadaesvaran, Nasrudin Abd. Rahim, A.K. Pandey, A.R. Bushroa, K. Ramesh, and S. Ramesh. Transparent self-cleaning coating of mod-

- ified polydimethylsiloxane (pdms) for real outdoor application. *Progress in Organic Coatings*, 131:232–239, 2019.
- [40] Karthik Raman, T.R Srinivasa Murthy, and G.M. Hegde. Fabrication of refractive index tunable polydimethylsiloxane photonic crystal for biosensor application. *Physics Procedia*, 19:146–151, 2011. International Conference on Optics in Precision Engineering and Nanotechnology (ICOPEN 2011).
- [41] Thomas Martin Reidy, Danli Luo, Priyokti Rana, Brenden Huegel, and Xuanhong Cheng. Transparency of pdms based microfluidic devices under temperature gradients. *Journal of Micromechanics and Microengineering*, 29(1):015014, dec 2018.
- [42] Yuan Qi, Yindian Wang, Changwen Zhao, Yuhong Ma, and Wantai Yang. Highly transparent cyclic olefin copolymer film with a nanotextured surface prepared by one-step photografting for high-density dna immobilization. *ACS Applied Materials & Interfaces*, 11(32):28690–28698, Aug 2019.
- [43] VK Shinoj, VM Murukeshan, SB Tor, NH Loh, and SW Lye. Design, fabrication, and characterization of thermoplastic microlenses for fiber-optic probe imaging. *Applied optics*, 53(6):1083–1088, 2014.
- [44] Jihoon Yeo, Jejun Ryu, Bong-Kee Lee, Euihyeon Byeon, Tai Hun Kwon, and Dong Sung Kim. Theoretical and experimental characterization of wettability of various nanolens arrayed polymer surfaces replicated with nanodimpled aluminum mold insert. *Microsystem technologies*, 16:1425–1430, 2010.
- [45] Sreeram Appasamy, Weizhuo Li, Se Hwan Lee, Joseph T Boyd, and Chong H Ahn. High-throughput plastic microlenses fabricated using microinjection molding techniques. *Optical Engineering*, 44(12):123401–123401, 2006.

- [46] Changhoon Baek, Jeffrey Kim, Youngro Lee, and Jong-mo Seo. Fabrication and evaluation of cyclic olefin copolymer based implantable neural electrode. *IEEE Transactions on Biomedical Engineering*, 67(9):2542–2551, 2020.
- [47] Hsiharn Yang, Ching-Kong Chao, Mau-Kuo Wei, and Che-Ping Lin. High fill-factor microlens array mold insert fabrication using a thermal reflow process. *Journal of micromechanics and microengineering*, 14(8):1197, 2004.
- [48] Jinfeng Qiu, Mujun Li, Huichun Ye, Junjie Zhu, and Chao Ji. Fabrication of high fill-factor microlens array using spatially constrained thermal reflow. *Sensors and Actuators A: Physical*, 279:17–26, 2018.
- [49] Amjad F Abdulkader, Qusay M Ali Hassan, Ahmed S Al-Asadi, H Bakr, HA Sultan, and CA Emshary. Linear, nonlinear and optical limiting properties of carbon black in epoxy resin. *Optik*, 160:100–108, 2018.
- [50] TOPAS. Topas 5013s-04 technical datasheet. https://topas.com/sites/default/files/TDS_5013S_04_e.pdf, 2019.
- [51] RK Jena, X Chen, CY Yue, and YC Lam. Viscosity of coc polymer (topas) near the glass transition temperature: Experimental and modeling. *Polymer testing*, 29(8):933–938, 2010.
- [52] Su-dong Moon, Namsuk Lee, and Shinill Kang. Fabrication of a microlens array using micro-compression molding with an electroformed mold insert. *Journal of Micromechanics and Microengineering*, 13(1):98, 2002.
- [53] Nachiappan Chidambaram, Robert Kirchner, Mirco Altana, and Helmut Schiff. High fidelity 3d thermal nanoimprint with uv curable polydimethyl siloxane stamps. *Journal of Vacuum Science & Technology B, Nanotechnology and Microelectronics: Materials, Processing, Measurement, and Phenomena*, 34(6):06K401, 2016.

- [54] The Dow Chemical Company. *Technical Data sheet - SYLGARD™ 184 Silicone Elastomer*, 2017.
- [55] S. Damodara, D. George, and A.k. Sen. Single step fabrication and characterization of pdms micro lens and its use in optocapillary flow manipulation. *Sensors and Actuators B: Chemical*, 227:383–392, 2016.
- [56] Kisoo Kim, Kyung-Won Jang, Jae-Kwan Ryu, and Ki-Hun Jeong. Biologically inspired ultrathin arrayed camera for high-contrast and high-resolution imaging. *Light: Science and Applications*, 9(1), 2020.
- [57] Hwiyeon Yoo, Geonho Cha, and Songhwai Oh. Deep ego-motion classifiers for compound eye cameras. *Sensors*, 19(23):5275, 2019.
- [58] Ruiliu Wang, Guangbiao Xu, and Yuechao He. Structure and properties of polytetrafluoroethylene (ptfe) fibers. *e-Polymers*, 17(3):215–220, 2017.
- [59] Benjamin K. Tsai, Catherine C. Cooksey, David W. Allen, Christopher C. White, Eric Byrd, and Deborah Jacobs. Exposure study on uv-induced degradation of ptfe and ceramic optical diffusers. *Appl. Opt.*, 58(5):1215–1222, Feb 2019.
- [60] Florian Schneider, Jan Draheim, Robert Kamberger, and Ulrike Wallrabe. Process and material properties of polydimethylsiloxane (pdms) for optical mems. *Sensors and Actuators A: Physical*, 151(2):95–99, 2009.
- [61] Ph Nussbaum, R Volkel, H P Herzig, M Eisner, and S Haselbeck. Design, fabrication and testing of microlens arrays for sensors and microsystems. *Pure and Applied Optics: Journal of the European Optical Society Part A*, 6(6):617–636, nov 1997.
- [62] Jun Wen, Xingpeng Yan, Xiaoyu Jiang, Zhan Yan, Ziqiang Wang, Song Chen, and Min Lin. Comparative study on light modulation characteristic between

- hexagonal and rectangular arranged macro lens array for integral imaging based light field display. *Optics Communications*, 466:125613, 2020.
- [63] Can Ding, Xiangchao Zhang, Xinyue Liu, Haoran Meng, and Min Xu. Structure design and image reconstruction of hexagonal-array photonics integrated interference imaging system. *IEEE Access*, 8:139396–139403, 2020.
- [64] Magdalena A. Tkacz and Kornel Chromiński. Advantage of using spherical over cartesian coordinates in the chromosome territories 3d modeling. In Valeria V. Krzhizhanovskaya, Gábor Závodszy, Michael H. Lees, Jack J. Dongarra, Peter M. A. Sloot, Sérgio Brissos, and João Teixeira, editors, *Computational Science – ICCS 2020*, pages 661–673. Springer International Publishing, 2020.
- [65] Geonho Cha, Hwiyeon Yoo, Donghoon Lee, and Songhwai Oh. Light-weight semantic segmentation for compound images. In *2017 IEEE International Conference on Multisensor Fusion and Integration for Intelligent Systems (MFI)*, pages 295–300, 2017.
- [66] Hwiyeon Yoo, Donghoon Lee, Geonho Cha, and Songhwai Oh. Estimating objectness using a compound eye camera. *2017 IEEE International Conference on Multisensor Fusion and Integration for Intelligent Systems (MFI)*, pages 131–136, 2017.
- [67] Hwiyeon Yoo, Geonho Cha, and Songhwai Oh. Deep ego-motion classifiers for compound eye cameras. *Sensors*, 19(23), 2019.
- [68] G S Brindley and W S Lewin. The sensations produced by electrical stimulation of the visual cortex. *J Physiol*, 196(2):479–493, May 1968.
- [69] W H Dobbelle, M G Mladejovsky, and J P Girvin. Artificial vision for the blind: electrical stimulation of visual cortex offers hope for a functional prosthesis. *Science*, 183(4123):440–444, February 1974.

- [70] S Uematsu, N Chapanis, G Gucer, B Konigsmark, and A E Walker. Electrical stimulation of the cerebral visual system in man. *Confin Neurol*, 36(2):113–124, 1974.
- [71] E M Maynard, C T Nordhausen, and R A Normann. The utah intracortical electrode array: a recording structure for potential brain-computer interfaces. *Electroencephalogr Clin Neurophysiol*, 102(3):228–239, March 1997.
- [72] Cordelia Erickson-Davis and Helma Korzybska. What do blind people ”see” with retinal prostheses? observations and qualitative reports of epiretinal implant users. *PLOS ONE*, 16(2):1–23, 02 2021.
- [73] Carol Brady-Simmons, Raquel Van Der Biest, and Laura Bozeman. Miami lighthouse for the blind and visually impaired case study: vision rehabilitation for the first florida resident to receive the argus ii “bionic eye”. *Journal of Visual Impairment & Blindness*, 110(3):177–181, 2016.
- [74] Norman Sabbah, Colas N Authié, Nicolae Sanda, Saddek Mohand-Said, José-Alain Sahel, and Avinoam B Safran. Importance of eye position on spatial localization in blind subjects wearing an argus ii retinal prosthesis. *Investigative ophthalmology & visual science*, 55(12):8259–8266, 2014.
- [75] Deepa Prabhu, Lisa Wise, Clare MacMahon, Marten De Man, Matthew Petoe, and Chris McCarthy. Effect of camera position on egocentric localisation with simulated prosthetic vision. *Engineering Research Express*, 3(1):015016, 2021.
- [76] Sang-In Bae, Kisoo Kim, Kyung-Won Jang, Hyun-Kyung Kim, and Ki-Hun Jeong. High contrast ultrathin light-field camera using inverted microlens arrays with metal-insulator-metal optical absorber. *Advanced Optical Materials*, 9(6):2001657, 2021.

초 록

기술의 발전으로 로봇이 점점 소형화 되고 있다. 로봇들은 그 목적에 따라 다양한 센서를 갖추고 있고 기본적으로 사람을 위해 쓰이기 때문에 카메라와 같은 시각센서를 기본적으로 탑재한다. 그러나 단일 카메라 하나만으로는 얻을 수 있는 공간 정보는 한정적이다. 상대적으로 큰 로봇들에는 라이다 센서, ToF센서 등 정확하고 다양한 정보 획득을 위한 여러 센서를 장착 할 수 있지만 소형 로봇에는 공간적, 에너지적 한계가 분명하다. 이 논문에서는 자연에서 영감을 얻은 생체모방형 마이크로렌즈 어레이를 통해 그 문제를 해결하고자 하였다. 마이크로렌즈 어레이를 활용하면 하나의 카메라 센서로 하나의 물체에 대해 두 가지 이상의 관점에서 바라볼 수 있기 때문에 사람 눈의 양안시와 같은 효과를 통해 물체의 거리를 측정할 수 있고, 이를 토대로 속도 계산 등 더욱 다양한 정보를 추출해 낼 수 있기 때문에 매우 유용할 것이다. 기존에 없던 새로운 방식으로 다양한 마이크로렌즈 어레이를 제작하고, 실제 촬영 샘플을 통해 어떠한 정보를 얻을 수 있는지 검증하고, 디자인의 분석을 통해 평면에서 제작된 렌즈들을 어떻게 곡면에 배치 할 수 있을지를 고려하여 최적의 결과를 낼 수 있는 방안 또한 알아보았다.

주요어: 생체모방, 마이크로렌즈 어레이, MEMS, 컴퓨터비전

학번: 2018-25309